EXPERIMENTAL INVESTIGATION OF A 2-D AIR AUGMENTED ROCKET:
EFFECTS OF NOZZLE LIP THICKNESS ON
ROCKET MIXING AND ENTRAINMENT

A Thesis

Presented to

The Faculty of California Polytechnic State University,

San Luis Obispo

In Partial Fulfillment

Of the Requirements for the Degree of

Master of Science in Aerospace Engineering

By

Trevor Allen Montre

December 2011

COMMITTEE MEMBERSHIP

TITLE: Experimental Investigation of a 2-D Air Augmented Rocket: Effects of Nozzle Lip Thickness on Rocket Mixing and Entrainment

AUTHOR: Trevor Allen Montre

DATE SUBMITTED: December 2011

COMMITTEE CHAIR: Dr. Dianne DeTurris, Aerospace Engineering Dept.

COMMITTEE MEMBER: Dr. David Marshall, Aerospace Engineering Dept.

COMMITTEE MEMBER: Dr. Jin Tso, Aerospace Engineering Dept.

COMMITTEE MEMBER: D. Ryan Gist, Pratt & Whitney Rocketdyne

ABSTRACT

Experimental Investigation of a 2-D Air Augmented Rocket: Effects of
Nozzle Lip Thickness on Rocket Mixing and Entrainment
Trevor Allen Montre

Cold-flow tests were performed using a simulated Air Augmented Rocket (AAR) operating

as a mixer-ejector in order to investigate the effects of varied primary nozzle lip thickness

on mixing and entrainment. The simulated primary rocket ejector was supplied with

nitrogen at a maximum chamber stagnation pressure of 1712 psi, and maximum flow rate

of 1.67 lb_m/s. Secondary air was entrained from a plenum, producing pressures as low as

6.8 psi and yielding maximum stagnation pressure ratios as high as 160. The primary

ejector nozzles each had an area ratio of approximately 20, yielding average primary exit

Mach numbers between 4.34 and 4.57. The primary flow was ejected into an 18.75 inch-

long mixing duct with a rectangular cross-sectional area of 2.10 in^2. The secondary flow

was entrained into the mixing duct through a total cross section of 0.94 in^2. Two mixing

duct configurations were used, one with plexiglass upper and lower surfaces for flow

visualization and one with pressure ports along the lower surface for primary plume

measurements.

Shadowgraph images were used to characterize the mixing duct flow field, while pressure

and temperature instrumentation allowed for calculation of various ejector performance

characteristics. Experimentally-calculated performance characteristics were compared to

inviscid theoretical predictions. Varying degrees of flow field asymmetry were observed

with each nozzle. Test repeatability was found to be excellent for all nozzles. Several

distinct phenomena were observed in both the primary plume and secondary streams.

The duration of secondary flow choking was found to be inversely proportional to nozzle lip thickness, due to the primary plume being physically closer to the secondary flow with a thinner nozzle lip. This indicated that the ejector's ability to choke the secondary flow is primarily an inviscid phenomenon.

Secondary flow blockage was demonstrated in two consecutive tests using the thickest nozzle lip. Only the left secondary duct became blocked in each case. Blockage was only demonstrated in the centerline pressure configuration, so no visual evidence was able to support the blocked flow theory.

At every pressure ratio, entrainment ratio was shown to increase with nozzle lip thickness. The original conical nozzle produced the largest level of entrainment, indicating that the angle of primary flow impingement was the largest contributing factor to secondary entrainment. The increase in efficiency resulting from a bell-mouth nozzle was less than the increase in entrainment efficiency of a conical nozzle, indicating that the conical design was more efficient overall for air augmented rocket applications.

ACKNOWLEDGMENTS

TABLE OF CONTENTS

LIST OF TABLES

LIST OF FIGURES

NOMENCLATURE

A	Area	$(\text{ft}^2, \text{in}^2)$
a	Speed of Sound	(ft/s)
K_{expand}	Plume Expansion Correction Factor	-
M	Mach Number	-
$\dot{m}$	Mass Flow Rate	(lb_m/s)
P	Pressure	$(\text{lb}_f/\text{in}^2)$
PR	Stagnation Pressure Ratio = P_{0p}/P_{0s}	-
psi,psia	Absolute Pressure	$(\text{lb}_f/\text{in}^2)$
psig	Gauge Pressure	$(\text{lb}_f/\text{in}^2)$
R	Universal Gas Constant	$(\text{lb}_f\text{ft}/\text{lb}_m°\text{R})$
T	Temperature	$(°\text{F}, °\text{R})$
t	Time	(s)
V	Velocity	(ft/s)
x	Distance Downstream of Nozzle Lip	(in)

Greek

φ	Entrainment Ratio = $\dot{m}_S/\dot{m}_P$	-
γ	Ratio of Specific Heats	-
ε	Nozzle Expansion Ratio = A_e/A^*	-
μ	Dynamic Viscosity	(slug/ft*s)
ρ	Density	(slug/ft^3)
σ	1st Standard Deviation	-

Subscripts

0	Stagnation Conditions
c	Critical
e	Nozzle Exit
i	Upstream of Choking
p, 1	Primary Stream
s, 2	Secondary Stream

Superscripts

*	Critical Point (sonic throat condition)

I.   Introduction

Human mobility has increased at an exponential rate over the last two hundred years. At the beginning of the nineteenth century, the mass transportation "normative paradigm" was the horse-drawn wagon; at the outset of the twentieth it was the train; and at the start of the twenty-first, the airplane. This phenomenon is sometimes called the 6-60-600 mph evolution of human transportation[1], and begs the question: will humanity continue this pace and enter the next century at 6000 mph, the speed of a hypersonic commercial vehicle?   The answer to that question will depend on the continuing evolution of hypersonic technologies.

The concept of high speed flight is not a new one. Within a decade of the Wright brothers' first heavier-than-air human flight in 1903, French engineer Rene Lorin published the first concept for a ramjet that could direct the exhaust from an internal combustion engine through a nozzle to create thrust. By the 1920's, Eugen Sänger had proposed the first concept for a winged hypersonic vehicle. In 1947, Chuck Yeager broke the sound barrier in the Bell X-1, and in 1949 the WAC Corporal, a US Army second-stage rocket mounted atop a captured German V-2 rocket, became the first man-made vehicle ever to reach hypersonic speeds. In 1961, only 58 years after the first powered human flight, Soviet Cosmonaut Yuri Gagarin became the first human to travel hypersonically when his Vostok I capsule reached Mach 25 on atmospheric reentry after the first manned orbital flight.

Hypersonic flight is defined by speeds in excess of Mach 5, or five times the local speed of sound. To date, the capability for hypersonic flight has remained almost exclusively the domain of chemical rockets. The reason for this limitation stems from the fact that

rocket propelled vehicles can operate from zero velocity (i.e. takeoff conditions) all the way up to orbital speeds, functioning both inside and outside the atmosphere. The main disadvantage to rocket propulsion is the fact that all of the fuel and oxidizer used in the chemical combustion process that produces thrust must be carried inside the vehicle. This constraint incurs considerable weight penalties, which leads to a requirement for staging in order for such a large vehicle to reach orbital velocities. In addition, even when considering the advancements in efficiency that have been realized since the advent of the chemical rocket engine, modern rockets are beginning to approach their theoretical limits in terms of realizable propulsive efficiency.

Air-breathing engines, as the name implies, operate by carrying only the fuel necessary for propulsion and using atmospheric air as their oxidizer. The result is a much lighter vehicle, but one that is limited to operation within the atmosphere. Turbine-based engines such as the turbojet and turbofan are examples of air-breathing engines that collect and compress their oxidizer from the atmosphere using rotating turbomachinery, which limits their speeds to roughly below Mach 3 based on the structural and thermal limits of the materials used in their construction.

Other high-speed air-breathing flight propulsion systems also exist, including the pulsejet engine and its derivative, the pulse-detonation engine (PDE), and the ramjet and its derivative, the scramjet. Pulsejets and PDEs operate based on the principle of unsteady periodic combustion, whereby combustion occurs in an intermittent manner based on fuel/air flame speeds and combustion chamber characteristics[2,3]. Pulsejets operate subsonically (deflagration), while PDE combustion is supersonic (detonation). PDEs are more efficient and can theoretically operate from subsonic up to hypersonic flight speeds

near Mach 5 without the moving parts required in turbine-based propulsion systems, which significantly reduces weight and maintenance issues. To date, however, PDEs have remained confined to laboratory experiments and flight tests due to the technical issues related to the complex dynamics of combustion by detonation.

The ramjet, like the pulsejet and pulse detonation engine, uses little to no moving parts and is specifically designed for high speed flight. Rather than use rotating machinery to compressing atmospheric air, the ramjet employs inlet geometry to compress incoming supersonic air through a series of oblique shocks that culminate in a normal shock just prior to the combustion chamber, where fuel is combusted subsonically. Ramjets require considerable forward speed in order to operate, typically flying at velocities between Mach 2 and 6, at which point the compression of incoming air raises combustion chamber temperatures beyond the physical limit of its materials. The scramjet, or supersonic combustion ramjet, is a derivation of the ramjet that can operate at much higher speeds by injecting fuel further upstream in the combustion chamber, thereby maintaining supersonic combustion and drastically lowering the temperature in the combustor. This leads to high efficiency performance well into the hypersonic regime, with scramjet operational limits estimated at between Mach 12 and Mach 24.

To date, only turbine-based air-breathing engines have seen widespread production and implementation. Ramjet engines have seen use in some applications, most notably as part of the hybrid turbojet/ramjet J-58 engine that powered the SR-71. The SR-71 aircraft, shown in Figure I-1, was powered by turbojet engines that switched to ramjet mode at high Mach numbers; at Mach 3.2, the aircraft's design cruise speed, 80% of the vehicle's thrust came from the ramjet section[4]. This also makes the J-58 turbo-ramjet

engines unique as one of the earliest combined cycle propulsion systems to be used in a production vehicle.
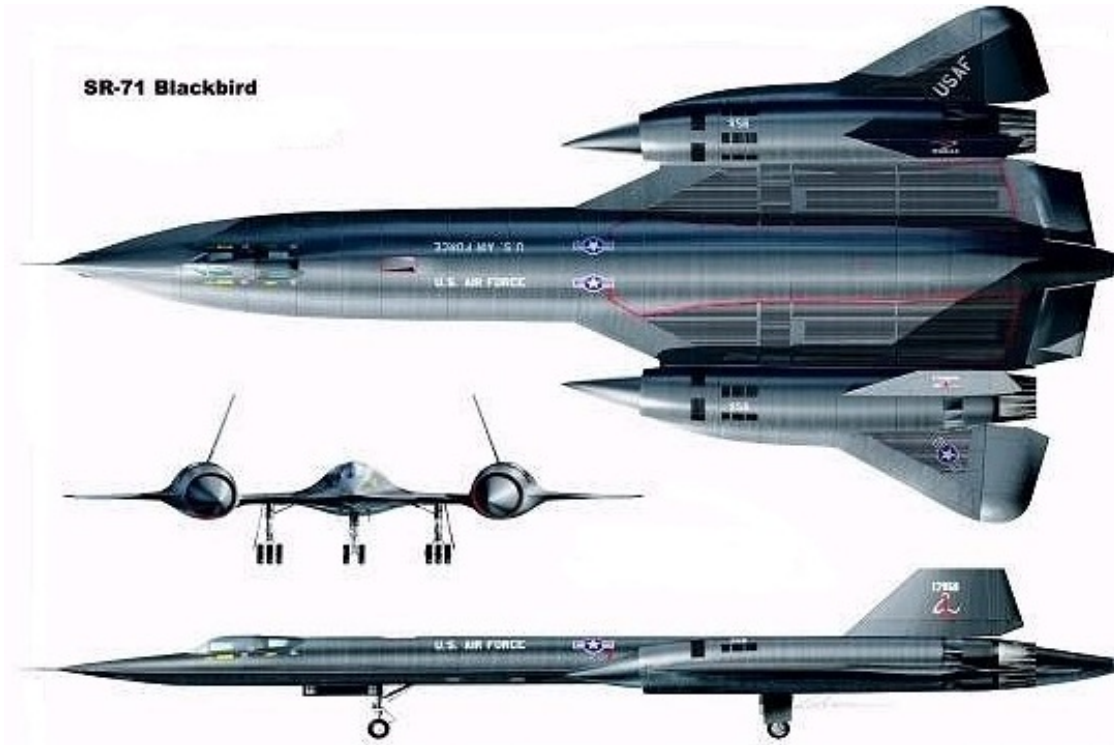
Figure I-1. 3-view image of the SR-71 Blackbird high speed reconnaissance aircraft[4].

Scramjet-powered vehicles have seen considerably less flight time than their ramjet-powered counterparts. The first scramjet flight test occurred in 2001, while the 2004 flight of NASA's X-43 proved for the first time that net thrust (thrust greater than drag) was possible using scramjet propulsion. Current projects like the Air Force's X-51A, DARPA's FALCON, Australia's HyShot, and the joint U.S.-Australian HIFiRE and HyCAUSE programs are continuing to probe the limits of hypersonic technology, albeit at a slow rate. Such a lag in development stems both from the high risk and cost associated with developing the new technologies required for these propulsion systems to operate, and from the fact that they can only operate in specific regimes of flight, necessitating a combination of propulsion systems for a vehicle to achieve independent

flight from takeoff and up to orbital velocities. However, successes like the recent flights of the X-51A Waverider scramjet, which flew for 200 seconds and reached speeds of Mach 5 in May of 2010, may indicate a new trend in hypersonic technology research[5]. The X-51A is shown in Figure I-2.
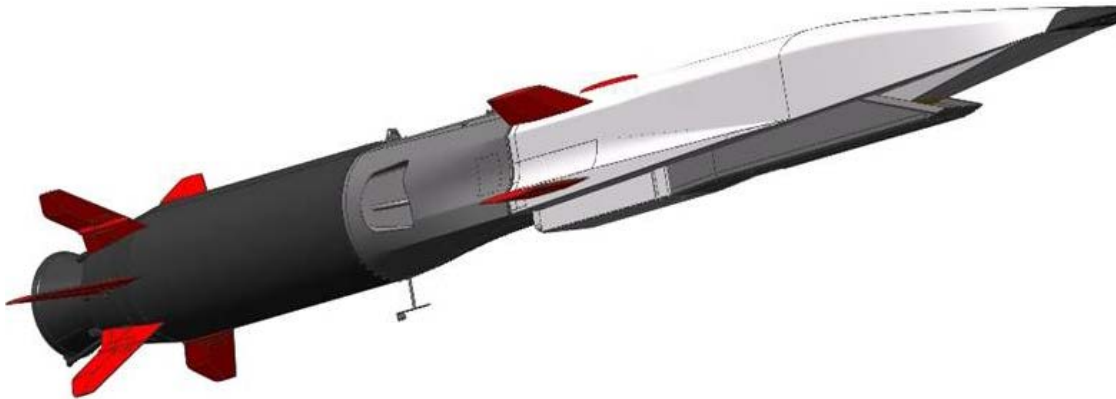
Figure I-2. X-51A Waverider scramjet engine technology demonstrator[6].

Aircraft and spacecraft are typically rated using specific impulse, or thrust per weight of fuel per second. It is thus convenient to compare the operational capabilities of high speed propulsion options by charting the variation of specific impulse with Mach number. Figure I-3 shows the specific impulses of different flight propulsion systems at different speeds, indicating the inherent advantage of combined cycle systems.
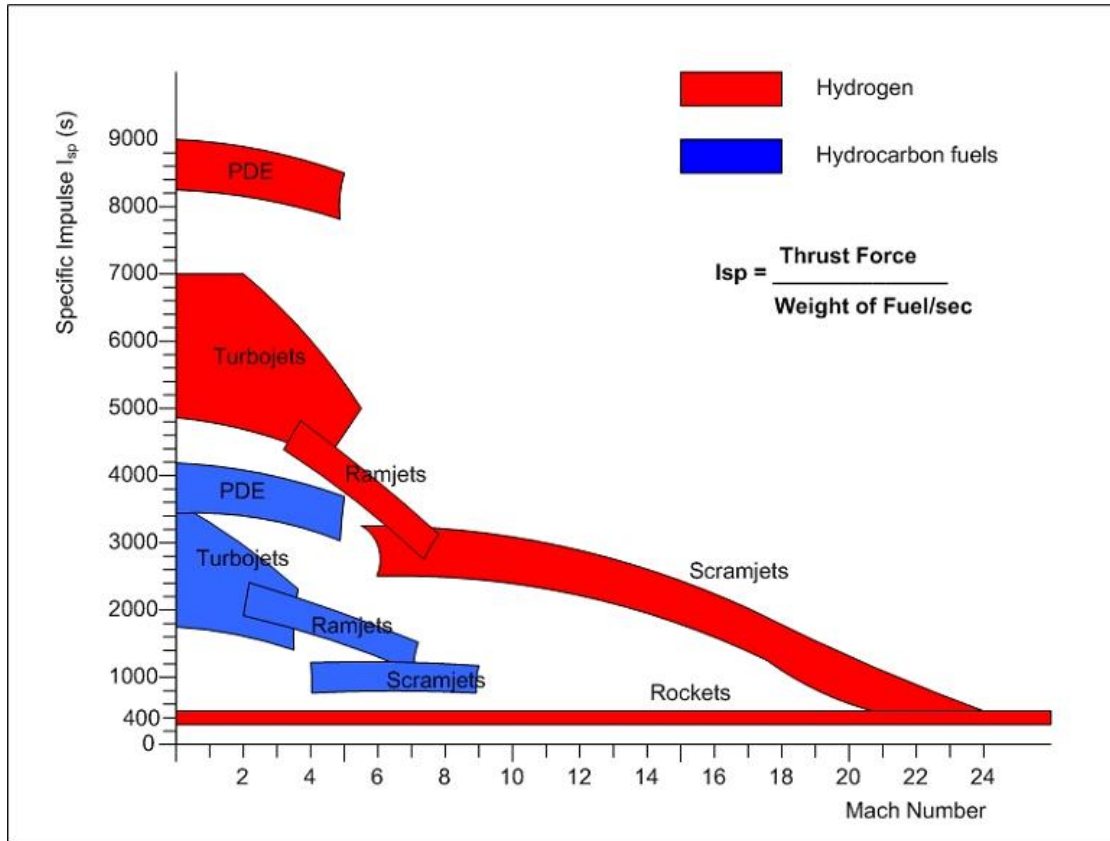
Figure I-3. Comparison of propulsive efficiencies at varying Mach numbers[7].

Flight vehicles implementing multiple propulsion systems are often called combined cycle vehicles. There are two separate and distinct types of combined cycle concepts in existence today: turbine-based combined cycle (TBCC), and rocket-based combined cycle (RBCC). As their names imply, the main difference between the two is their initial method of propulsion. TBCC vehicles typically make use of a turbojet engine for takeoff and acceleration to supersonic speeds before transitioning to ramjet propulsion near Mach 3, followed by a transition to scramjet propulsion at Mach 6, and finally transitioning to full rocket propulsion somewhere between Mach 12 and Mach 24 and remaining in that state until the vehicle reaches orbit. For an RBCC vehicle, the main difference is in the low-speed, high thrust takeoff and landing mode. Rather than using a turbojet at low speeds, rocket-based systems mix incoming air with a fuel-rich primary rocket exhaust,

essentially augmenting the thrust of the main rocket during takeoff when maximum thrust is crucial. Like TBCC systems, the RBCC vehicle then typically transitions to ramjet, scramjet, and full rocket.

Combined cycle systems are typically highly integrated, sharing the same flow path and fuel systems. The main advantage to this is weight reduction and its resulting correlation with increased efficiency, along with increasing the vehicle's reusability by eliminating its need to jettison stages or other components during its acceleration to orbital velocity. NASA's GTX Air-Breathing SSTO Vehicle Concept, shown in Figure I-4, highlights the high integration inherent to a RBCC design. While some RBCC concepts, such as NASA's GTX and the Soviet Gnom project of the 1960's, have been investigated in the preliminary design stage, no functional RBCC vehicle has ever been built.
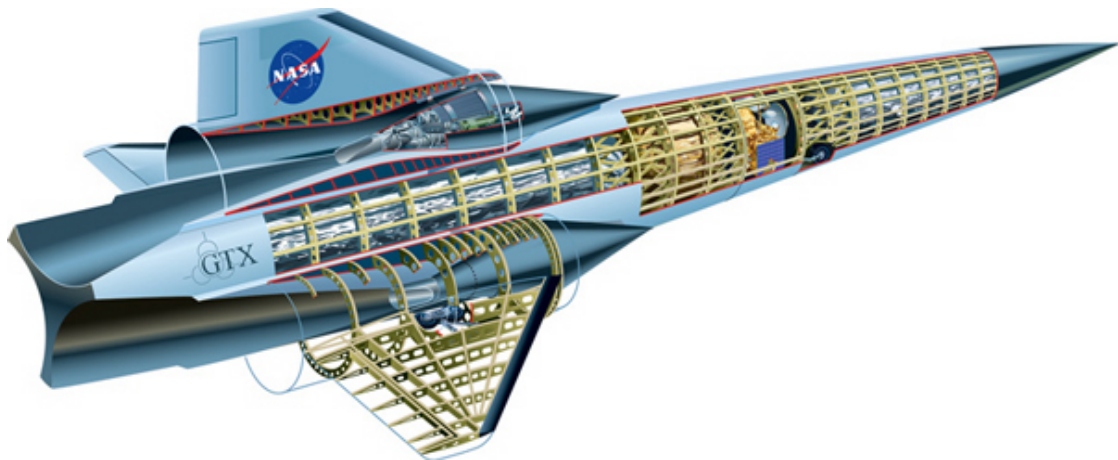
Figure I-4. NASA's GTX air-breathing SSTO vehicle concept[8].

Staged propulsion vehicles, as the term implies, consist of several discrete propulsion subsystems that power the vehicle through different stages of its flight regime, which are then typically discarded when the vehicle reaches the desired speed or altitude for the next propulsion subsystem to take over. All modern rocket launch vehicles fit this profile, whereby the largest and highest thrust first stage propels the 1st, 2nd, 3rd, and

sometimes 4th and 5th stage vehicles at liftoff and is later jettisoned to allow the 2nd stage to operate, and so on. Similarly, research vehicles like the X-43 and X-51 were air-launched at Mach 0.7 and then accelerated on a booster rocket until they had reached speeds where scramjet operation could take over, at which point the rocket was jettisoned and thrust was provided by the scramjet. Based on this definition, most launch vehicles are four- or five-stage-to-orbit. One exception is the Space Shuttle, which can be called semi-reusable because it takes off using both solid rocket boosters (SRBs) and its main engines, but only the auxiliary SRBs are jettisoned during flight. The Space Shuttle is considered a two-stage-to-orbit (TSTO) payload delivery system. The high efficiency that results from combining propulsion subsystems in a combined cycle-powered vehicle has the potential to achieve single-stage-to-orbit transportation.

A.   Background

In concept, an RBCC-powered vehicle would operate using four separate modes of propulsion: air augmented rocket, ramjet, scramjet, and full rocket, in that order. The air augmented rocket (AAR) is essentially a rocket firing in a duct, with ambient air being entrained by the fuel-rich primary rocket's exhaust in order to both augment its thrust and provide additional oxidizer for re-combustion. Thrust augmentation would occur during takeoff and acceleration to higher speeds, in the low-speed, high-thrust portion of the vehicle's flight profile, at which point the ramjet would take over to provide thrust. The focus of this research is on the AAR portion of an RBCC vehicle's flight profile.

Based on its geometry and the conditions in which it performs, the air augmented rocket can be considered analogous to the more common induction pump and/or mixer-ejector, which are both widely used in industry for a number of applications. The idea behind

both of these instruments is that a high-velocity, high pressure "primary" flow is used to entrain a low-velocity, low pressure "secondary" flow. Some amount of mixing occurs between the two streams, and the now-energized stream consisting of both flows "ejects" to create thrust. The domain in which the two flows interact is termed the "mixing duct". Figure I-5 shows a typical air augmented rocket configuration[9].

Mixing Duct

Secondary Flow (Air)

Primary Flow (Rocket)

Primary Plume
Boundary

Secondary Flow (Air)
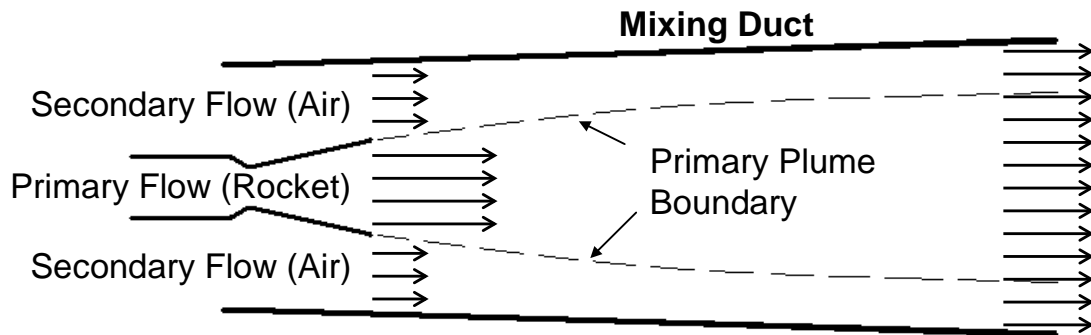
Figure I-5. Generic air augmented rocket configuration.

Ejector performance is typically measured in terms of the ratio of mass flow rates between the primary and secondary streams, also known as the entrainment ratio, φ. Because the goal of an air augmented rocket is to maximize thrust during takeoff, this correlates to the highest possible entrainment ratio. High entrainment requires a high ratio of primary to secondary stagnation pressures. With the secondary stream's stagnation pressure assumed to be held at or near to constant atmospheric (takeoff) conditions, this implies a high throttle setting for the primary rocket and thus high chamber pressures and flow rates.

B. General Mixer-Ejector Theory

A generic definition for mixer-ejector is a device which uses a high speed primary flow to entrain, and subsequently mix with, a low speed secondary flow. From an analytic point of view, the mixer-ejector can take two forms: if secondary entrainment is unknown

and must be calculated, the device is known as an "ejector"; if instead the secondary flow is forced into the mixing duct at a known rate, the device is known as a "mixer" and is analyzed as such. As stipulated by Gist[9], the Cal Poly AAR operates as an "ejector"; the current work will maintain his nomenclature. Additionally, the physical area where the primary and secondary streams are free to interact is labeled the "mixing duct", although this does not imply that the apparatus is operating as a "mixer" the way it was defined previously. Within the ejector's range of operation there exist several distinct modes depending on the conditions at the mixing duct inlet and exit.

The first case will occur if either the secondary and ambient pressures are high enough or the primary pressure is low enough, producing an overexpanded condition in the primary nozzle. As a result, the back pressure at the mixer exit forces a strong shock train to form in the primary plume which terminates in a normal shock. This shock structure decelerates the primary flow to subsonic velocities. The secondary flow is then entrained by a subsonic primary flow and the streams become mixed before exiting the duct. Mixing of the two streams takes place downstream of the normal shock, but the normal shock and full mixing usually occur only in mixing ducts of sufficient lengths and back pressure. This case is often called the subsonic condition and is illustrated in Figure I-6.
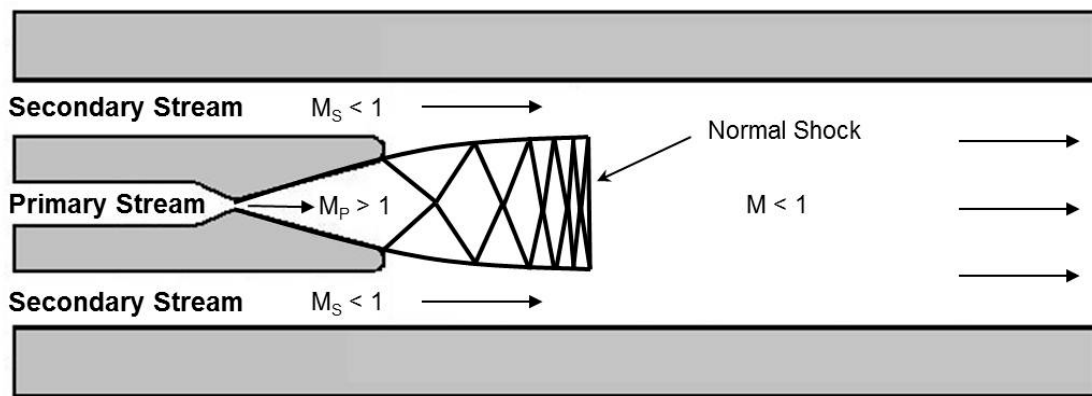
Figure I-6. Subsonic ejector operation mode.

It is also worth noting that if the duct is sufficiently short or insufficient mixing is caused by some other mechanism, two separate streams may persist through the length of the mixing duct. This mode, called the mixed case, is a variant of the subsonic case and indicates that the secondary stream does not achieve aerodynamic choking before the duct exit. Thus the flow consists of a supersonic primary stream and subsonic secondary stream with a pronounced slip line in between. In both the subsonic and mixed cases, entrainment is dictated by the ambient pressure at the mixing duct exit plane.

Increasing the primary stagnation pressure will eventually cause the flow to become saturated supersonic, the second mode of ejector operation. The saturated supersonic case occurs when the secondary flow achieves aerodynamic choking and a sonic condition at the point where the secondary duct connects to the mixing chamber, before it is exposed to the primary plume. Secondary choking occurs here because the space between the duct wall and the primary nozzle becomes the point of minimum area. In this case the primary plume is optimally expanded. The saturated supersonic condition is shown in Figure I-7.
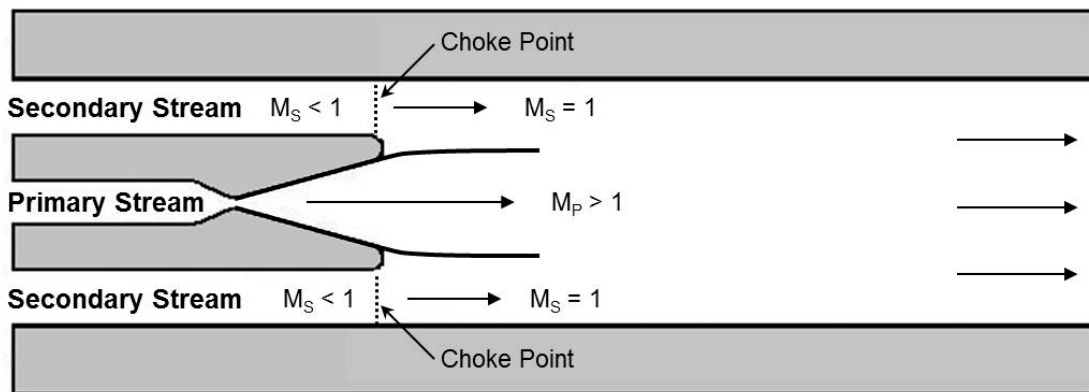
Figure I-7. Saturated supersonic ejector operation mode.

If the primary stagnation pressure is increased beyond the saturated supersonic condition, the primary plume will become underexpanded. If the underexpanded plume impinges

on the secondary flow enough, the condition is classified as Fabri choked, a name taken from the scientist who discovered it. In this case, the primary flow is supersonic and the secondary flow achieves a sonic condition due to the expanding primary plume, which acts as an aerodynamic throat, causing the secondary flow to converge between the primary plume and duct wall. Because the primary plume is underexpanded in this case, weak shocks and expansion fans may exist within the plume. However, this shock structure is not significant enough to decelerate the plume to subsonic speeds. The Fabri choked condition is illustrated in Figure I-8.
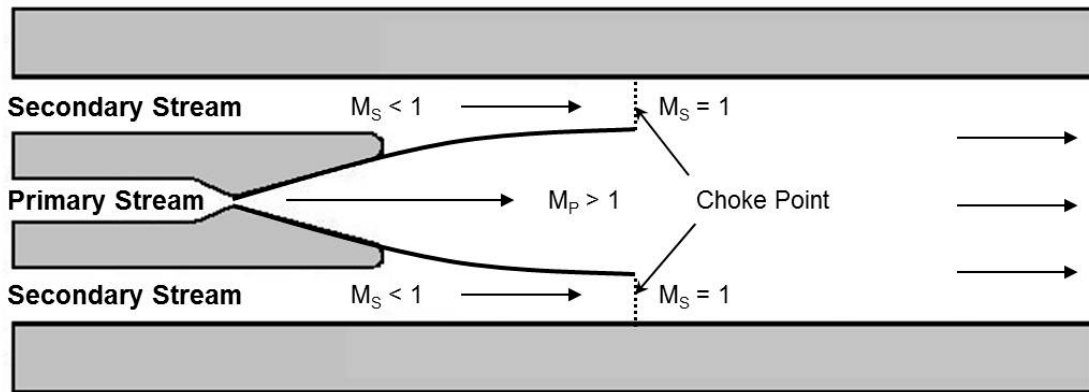
Figure I-8. Fabri choke ejector operation mode.

As with the subsonic case, there exists a variation of the Fabri choked condition. At extremely high primary stagnation pressures, the primary plume may become so underexpanded as to impinge upon the mixing duct wall. This is known as the blocked condition. In the blocked case the secondary flow is prevented entirely from entering the mixing duct and thus secondary entrainment is reduced to zero. In extreme cases of this condition, the primary plume may even reverse direction and move upstream into the secondary duct, potentially causing a secondary inlet unstart. In the saturated supersonic, Fabri choked, and blocked cases secondary entrainment is not a function of downstream

ambient conditions but rather depends on primary-to-secondary stagnation pressure ratio and mixer-ejector geometry.

C.   Current Applications

The scenarios just described are for a generic supersonic air ejector. They have been studied previously via both theoretical and experimental investigations as part of the Cal Poly Air augmented Rocket research project. The current investigation seeks to expand upon that work.

In previous research, the primary flow was accelerated by a conical nozzle with a fixed lip thickness. All prior theoretical and experimental work assumed that the design of the primary nozzle did not play a significant role in the performance of the AAR. The intent of the present work is to investigate the effects of introducing new nozzle geometries into the test apparatus. Primarily, the viscous effects of varying primary nozzle lip thickness are investigated. The present work also examines what affect, if any, may result from changing the primary nozzle from a conical design to a more efficient bell-mouth contour. These results are then compared to the previous analytical and experimental conclusions.

Flow field analysis is performed using both the focused shadowgraphy flow visualization technique and recorded flow pressure and temperature data. Specifically, shadowgraph images of the flow are used to characterize observed phenomena in the primary plume and secondary flow. Rocket performance is compared for each configuration based primarily in terms of secondary entrainment.

II. Literature Review

There has been an abundance of research into supersonic air ejectors in the last half-century, both in the United States and internationally. Collectively, this knowledge has provided a solid technical foundation for the present work. Individually, the works can be classified based on how they influenced it. Seminal works serve as the foundation for not only the present investigation, but nearly all works into supersonic ejectors that have come after them. Supplemental works are especially relevant to the present work because they investigate the same factors in either ejector performance or simply nozzle performance, and in most cases their results are very similar. Previous works directly preceded the present investigation on the Cal Poly AAR project, and as such provided both the necessary hardware and accumulated knowledge to successfully modify and operate the current test apparatus and understand the results that it produced.

A. Seminal Works

Several works, including Fabri, Addy, Emanuel, and Papamoschou, have acted as the primary source of knowledge on the Cal Poly AAR project. Fabri defined the operating conditions in supersonic ejectors based on primary flow stagnation pressures. Addy expanded on Fabri's method, introducing a Method of Characteristics analysis to model the primary plume. Emanuel compared Fabri's analysis to a simple 1D method and proposed a new hybrid of the two. Papamoschou introduced viscous and heat transfer effects to Fabri's model.

1. *Fabri*

Fabri et al.[10,11] were the first to investigate the operating conditions and flow interactions in a supersonic air-to-air ejector. Fabri's ejector is cylindrical and axisymmetric, with a high pressure supersonic primary flow and low pressure subsonic secondary flow. Both flows are assumed to be composed of air, which is treated as a perfect gas. At the mixing chamber entrance, the primary flow velocity is low supersonic while the secondary flow velocity varies between low subsonic and sonic. At the exit of the mixing chamber, the flows have uniform pressure which is equal to atmospheric conditions. Fabri's analysis does not account for viscous interactions between the primary and secondary streams, although a correction is made for pressure loss due to the friction between the secondary flow and the duct wall. Fabri also includes a term for the thickness of the primary nozzle lip in his calculations in order to account for the turbulent wake shed downstream of the lip.

In Fabri's method the primary flow is solved using a quasi-1D approach, although Fabri suggests that the Method of Characteristics be utilized when the primary plume area is expanding because the quasi-1D approach requires correction factors to predict the area of the primary plume. Once the primary flow has been solved, the values of the primary and secondary stream conditions at the mixing chamber inlet are used to solve the conservation equations for mass, momentum, and energy. The outlet condition is then solved as the sum of the primary and secondary inlet mass flow, momentum, and energy with the stipulation of uniform pressure equal to ambient.

Fabri defines three modes of ejector operation in order of decreasing primary stagnation pressure: Fabri choke supersonic, saturated supersonic, and subsonic. The Fabri choke

and saturated conditions are both special cases of the supersonic case. Fabri also points out that if the duct is sufficiently short or insufficient mixing is caused by some other mechanism, two separate streams may persist through the length of the mixing duct. This mode, called the mixed case, indicates that the secondary stream does not achieve aerodynamic choking before the duct exit, and thus the flow consists of a supersonic primary stream and subsonic secondary stream with a pronounced slip line in between. Fabri's method has several limitations, although it serves as the technical foundation for all future works on supersonic air-to-air ejectors. By utilizing conservation of energy and momentum to solve for the aerodynamic flow patterns for each condition, the method provides some insight into the interactions between the flows. However, it does not accurately predict the properties of either the primary or the secondary flow within the mixing chamber. Fabri also concludes that his inviscid approach is valid for supersonic ejector flow fields with similar specific heat ratios, high Mach numbers, and high Reynolds numbers, because under these conditions the flow field is maintained primarily by inviscid forces. However, later works indicate that viscous forces play more of a role in the flow field interactions than Fabri concludes.

2. Addy

Addy[12] presents a flow model developed to simulate axisymmetric air-to-air ejectors with a supersonic primary plume. To start, he imposes several limitations on the model based on Fabri's assumptions: The ejector geometry is axisymmetric and cylindrical; the primary and secondary flows are of the same perfect gas composition and at the same stagnation temperatures; the primary flow is supersonic at the exit of the primary nozzle, while the secondary flow velocity varies from subsonic to sonic; and the Mach number is

16

uniform at the exit of the duct. Addy makes three major improvements over Fabri's quasi-1D model: the addition of a Method of Characteristics (MOC) analysis to describe the primary plume, a capability for quantifying the viscous interaction between the primary and secondary streams, and a method of transient ejector analysis.

The Method of Characteristics acts as the starting point in Addy's analysis. By providing a two-dimensional distribution of gas properties in the primary plume, it yields a much higher quality prediction of the plume than Fabri's quasi-1D estimates. Once a MOC solution has been found, a continuous pressure distribution condition is imposed along the boundary between the primary plume and the secondary stream; this is also known as a pressure-matched boundary condition. Once this value is known, the one-dimensional secondary stream properties are solved using the primary plume shape and a guess for both the inlet Mach number and the ratio of primary-to-secondary stagnation pressures. A solution is calculated after each iteration, with subsequent adjustments to the inlet Mach number until the desired solution is attained.

Addy's analysis addresses the various steady-state cases discussed by Fabri, beginning with the saturated supersonic and Fabri choke condition, both of which operate independently of ambient pressures. Based on a guessed input for secondary inlet Mach number, The Method of Characteristics is used to determine the minimum area available for the secondary flow. In this case, the secondary stream may remain subsonic, achieve a sonic condition before the minimum area, or become sonic at the minimum area of secondary flow. If the secondary flow does not achieve the sonic condition at the minimum area, the assumed secondary inlet Mach number must be changed until the results match the desired properties.

Each final solution provides the entrainment ratio and stagnation pressure ratio, as well as the properties of the primary and secondary streams within the mixing chamber. In addition, the Method of Characteristics provides the jet boundary location of the primary plume, the angle of the boundary between the primary and secondary flows, and a two-dimensional Mach number distribution within the primary plume. Analysis of the entrained flow yields the quasi-1D secondary Mach number and secondary pressure distribution.

Addy presents methods for both inviscid solutions and viscous superposition corrections, as well as a full viscous solution. Following the discussion of a full viscous solution, the effects of ambient-to-primary pressure ratios are investigated. Addy also correlates transient and steady-state ejector operating characteristics based on quasi-steady concepts for the response of separated flows to transient conditions. He concludes that transient ejector performance can be interpreted using a dimensionless time variable that he defines based on flow and system parameters. Addy finishes his investigation with an assessment of other steady-state ejector analysis methods, concluding that the differences between his analytical results and available experimental data are acceptable for steady-state conditions and "indistinguishable" for transient conditions.

3. Emanuel

Emanuel[13] performs a theoretical analysis of supersonic air-to-air ejector performance using both a 1D approach and Fabri's inviscid method. The primary advantage of the 1D method is its ease of implementation - in this method all parameters save for a single independent variable, typically the inlet Mach number, are fixed. The consequence of this, however, is that the method requires a large number of assumptions and initial

knowledge of the ejector conditions as inputs; as a result, the 1D method provides little insight into the flow phenomenon occurring within the ejector.

Emanuel's model requires an assumption of constant area mixing or constant pressure mixing, with the option to apply both conditions simultaneously. The constant area assumption requires the mixing area to remain unchanged in the streamwise direction, while the constant pressure assumption implies equal primary and secondary pressures at the entrance to the mixing chamber. The model also assumes fully mixed flow at the exit of the ejector duct. Both the primary and secondary flows are characterized by their stagnation conditions, Mach number, and area at the entrance to the mixing chamber. Based on these values, other properties such as velocity and mass flow rate can be backed out. Once all flow properties are known, a control volume approach using conservation of mass, momentum, and energy is then applied to calculate the final solution. This method can be applied to cases with either subsonic or supersonic exit velocities, with the additional constraint on the subsonic case that a normal shock be imposed in the stream to decelerate the flow before it exits the duct.

In comparing his technique to Fabri's analysis, Emanuel concludes that Fabri's isentropic quasi-1D method has many limitations, with his main criticism being that Fabri does not account for the case in which the secondary flow is supersonic at the secondary inlet. He also states that Fabri's isentropic method for modeling the primary flow breaks down when secondary flow enters the mixing chamber at transonic speeds. Emanuel suggests that this issue may be remedied by using the Method of Characteristics to solve for the primary plume area.

4. Papamoschou

Papamoschou[14] develops an analytical model for investigating the performance of a constant-area ejector with non-uniformly mixed exit flow. Both axisymmetric and two-dimensional configurations are investigated. The model assumes that the primary plume is supersonic and the secondary entrained flow is subsonic, and both streams are treated as quasi-1D. Viscous and heat transfer effects from the analytical equations developed for the model are transformed into a local coordinate axis and superimposed along the streamline separating the primary and secondary streams.

Papamoschou concludes that the axisymmetric ejector provides better thrust augmentation than the two-dimensional one due to higher skin-friction losses in the 2-D configuration. He also concludes that thrust increases with ejector length, but at a diminishing rate; that for all configurations, thrust augmentation decreases with flight Mach number and becomes zero at a flight Mach number near 0.7; and that increasing the primary-to-secondary area ratio has a minimal effect on thrust. He claims that the analytical results compare favorably with available experimental data on pressure distributions and mass-flow ratios.

B.   Supplemental Works

In addition to the foundational works by Fabri, Addy, Emanuel, and Papamoschou on the topic of supersonic ejectors, numerous works have been published that more thoroughly investigate subjects influential to the current work. These topics include shear layers, variable geometry ejector designs, and the viscous effects of nozzle lip thickness.

1. *Shear Layers*

Fabri concluded that for supersonic mixer-ejectors with similar specific heat ratios, high Mach numbers, and high Reynolds numbers, the mixing duct flow field is maintained primarily by inviscid forces[10,11]. However, subsequent authors have found that viscous forces play an important role in flow field interactions between the primary and secondary streams in supersonic ejectors. Understanding the shear layer that forms in the recirculation region at the base of the primary nozzle lip thus plays an important role in modern supersonic ejector studies such as the present one.

Dimotakis

Dimotakis[15,16] performs wind tunnel experiments to investigate two-dimensional, non-reacting, compressible, turbulent shear layers. Helium, nitrogen, and argon gases are used in various combinations to produce shear layers with isentropically computed convective Mach numbers that range from low subsonic to nearly sonic. Each test makes use of one high speed gas and one low-speed gas which begin mixing after passing over a splitter plate. Schlieren photography is used to measure the growth rate of the shear layer that forms between the two flows.

Dimotakis observes travelling shock and expansion waves in the low speed, high compressibility flows, which he believes are created by turbulent structures convecting at supersonic velocities. He concludes that they cannot be standing waves because the low-speed flow Mach number is much less than unity. Dimotakis also observes a lack of evidence in the compressible flows of the two-dimensional, large-scale turbulent structures seen in incompressible flows. However, because the spacing of the travelling

waves is seen to be on the order of the local shear layer thickness, Dimotakis concludes that some form of large-scale structure is present. Two possible explanations are given for this contrasting evidence: either the large-scale structure is highly distorted by spanwise three-dimensionality, or it is obscured by many small-scale, high-gradient turbulent structures superimposed on top of it.

Dimotakis's results also suggest that turbulent shear layer vortices may be capable of locally accelerating the flow to supersonic speeds. Because such accelerated flow must eventually come to rest at a stagnation point in the convective reference frame, Dimotakis concludes that a very strong recompression shock inside the shear layer would be necessary for this to occur. However, he is unable to observe such a shock.

Dimotakis makes two conclusions about shear layer growth rates: first, that the coupling of a low density ratio and a supersonic free stream Mach number seem to produce low shear layer growth rates; and second, that the shear layer growth rate is relatively insensitive to the effects of incident shock and expansion waves. Dimotakis's shear layer measurements are in close agreement with previous results by other experimenters, except for a few unusual cases at low compressibility and low density ratio.

Papamoschou

Papamoschou and Roshko[17] perform experiments to investigate turbulent two-stream compressible shear layers between similar and dissimilar gases at a variety of free stream Mach numbers, ranging from subsonic to high supersonic, in order to study compressibility effects together with those of density and velocity ratios. Instantaneous flow visualization is accomplished using a Schlieren optical system. The growth of the

turbulent region is defined by means of Pitot-pressure profiles measured at several streamwise locations.

Papamoschou begins his analysis by defining a compressibility-effect parameter in order to correlate and unify his experimental results. This parameter, which Papamoschou calls the convective Mach number, is defined as the Mach number in a coordinate system convecting with the velocity of the dominant waves and structures of the shear layer. In Papamoschou's experiments, it ranges from 0 to 1.9. Using this parameter, Papamoschou finds that for nearly every case examined, the correlation between shear layer growth rate and convective Mach number fall approximately onto one curve when the growth rate is normalized by its incompressible value at the same velocity and density ratios. This normalized growth rate (which is unity for incompressible flow) decreases rapidly with increasing convective Mach number, reaching an asymptotic value of approximately 0.2 for supersonic convective Mach numbers.

Papamoschou also concludes that for a given convective Mach number, the effects of density ratio and velocity ratio on the growth rate follow a trend similar to those in an incompressible shear layer: the growth rate is smaller when the heavier gas is on the high-speed side and larger when the heavier gas is on the low-speed side; in other words, the growth rate increases with decreasing velocity ratio, i.e. with increasing free-stream-velocity difference. Based on Schlieren images of the flow, Papamoschou also agrees with Dimotakis's conclusions indicating the existence of large-scale turbulent structures in the compressible shear layer.

Anderson

Anderson[18] performs a theoretical analysis of the viscous interaction that occurs between the primary and secondary streams of ejector nozzles. The analysis accounts for real sonic-line effects in the primary nozzle flow field and the streamwise variations in mixing and boundary layer size within the ejector. Anderson illustrates aspects of the analysis by applying the theory to a variety of ejector configurations including cylindrical shroud, contoured flap, and plug nozzles. Extensive comparisons are made between theory and data to show the importance of various analytical assumptions and such design variables as diameter ratio, spacing ratio, total temperature ratio, and primary nozzle geometry.

Anderson concludes that both primary nozzle inlet flow conditions (sonic-line) and point-wise mixing between the primary and secondary streams strongly influence the pumping and thrust characteristics of ejector nozzles. When the secondary inlet Mach number becomes high, the pumping characteristics can be noticeably affected by boundary layer flow blockage. Furthermore, high primary nozzle inlet temperatures strongly affect the ejector's pumping characteristics, while giving only marginal gains in thrust efficiency if the ejector is operating at optimum conditions. Finally, the author believes that the heat transfer process associated with turbulent mixing zones within ejector nozzles might noticeably affect ejector performance.

2. *Variable Nozzle Design*

Several authors have investigated how changing the primary nozzle configuration in supersonic ejectors may affect such issues as entrainment ratio, stagnation pressure ratio, and downstream mixing of the primary and secondary flows.

Matsuo

Matsuo et al.[19] investigate the performance of both straight-tube and second-throat supersonic air ejectors over a range of ejector-to-nozzle throat-area-ratios and primary Mach numbers. In this case, a second-throat ejector is defined as one in which the mixing duct downstream of the primary nozzle/secondary duct forms a second converging-diverging throat capable of choking the flow. Thus, the ejector-to-nozzle throat-area-ratio is defined as the ratio of the area of the ejector throat to the area of the primary nozzle throat. Variable throat-area-ratios are achieved using primary nozzles designed for different operating Mach numbers.

The authors classify the ejector's performance based on four separate, distinct flow states that can occur: (1) fully supersonic flow, in which the primary flow fully expands in the mixing tube and the secondary flow is entrained by interacting and mixing with the primary flow; (2) choked secondary flow, in which the secondary flow is choked at a certain point upstream of the ejector throat – this point moves as entrainment ratio increases, finally reaching either the inlet of the mixing tube (in the case of the straight-tube ejector) or the ejector throat (in the second-throat ejector); (3) shock-between-throats flow, in which a pseudo-shock is located between the primary nozzle throat and the ejector throat, and the secondary flow does not choke; and (4) doubly choked flow, in

which the primary flow is choked both at the primary nozzle throat and at the ejector throat, and two pseudo-shock waves occur, one upstream and the other downstream of the ejector throat.

The authors draw several conclusions from these experiments. The first is that secondary flow conditions depend strongly on the primary stagnation pressure, when throat-area-ratio and primary Mach number are held constant. As such, there exists an optimum primary chamber pressure for which the secondary mass flow rate is maximized while the secondary pressure is minimized. The second conclusion is that for a constant primary Mach number and optimum primary chamber pressure, secondary mass flow rate and secondary pressure vary only with throat-area-ratio. Furthermore, an optimum throat-area-ratio exists for which the primary chamber pressure can be minimized while still maximizing secondary flow rate and minimizing secondary pressure. This value is considerably larger than the optimum throat-area-ratio for the case of zero secondary flow.

The third conclusion is that the primary chamber pressure that maximizes the conventional isentropic efficiency at the maximum secondary flow rate is not necessarily equal to the maximum primary chamber pressure. This chamber pressure decreases with primary Mach number.

Lee

Lee et al.[20] investigate the flow characteristics of variable sonic/supersonic ejector systems using both numerical and experimental studies. The main objective of their investigation is to understand the effects of ejector throat-area-ratio and operating pressure ratio on the entrainment of a secondary stream in the variable ejector system. As

with Matsuo, the experiments are performed in a second-throat supersonic air ejector. Variable operating conditions (i.e. variable throat area ratio) are achieved in the ejector via a cone cylinder mounted on the flow axis. A screw handle installed outside the ejector is used to shift the cone cylinder along the ejector axis, thus changing the cross-sectional area at the nozzle throat while keeping the cross-sectional area at the ejector throat constant. As a result, the throat area ratio can be increased as the cone is moved upstream further into the primary nozzle throat.

The authors observe that for a given pressure ratio the cone cylinder of the variable ejector can control the recirculation ratio of the secondary suction mass flow. They conclude that the secondary mass flow rate of the ejector is strongly influenced by the ejector throat-area-ratio, although this only occurs at high operating pressure ratios. They also observe that for the sonic case, the entrainment ratio increases as the ejector throat-area-ratio increases while at a constant operating pressure ratio, whereas in the supersonic case the entrainment ratio decreases at a constant operating pressure ratio. They conclude that variable sonic/supersonic ejector systems can be operated to obtain the required entrainment ratio by altering the ejector throat area ratio and the operating pressure ratio.

Enomoto

Enomoto et al.[21] perform cold flow tests with a scale model of a typical 2-D convergent-divergent (2-DCD) ejector nozzle configuration to investigate its internal flow field and aerodynamic performance characteristics, including entrainment ratio. As with Matsuo and Lee, the experiment uses a second-throat ejector rather than a straight-tube ejector. Thus, throat-area-ratio is again defined as the ratio of throat areas between the primary

flow nozzle and ejector nozzle. In this case, primary flow acceleration is achieved via a converging sonic nozzle rather than a converging-diverging supersonic nozzle. The authors achieve throat-area-ratio variability using two-axis translation: the primary nozzle can be translated upstream and downstream of the second ejector throat, and both the primary nozzle and ejector walls can be expanded outward about the ejector centerline. Using Mach-Zehnder interferometry, the authors record and characterize shear layers, compression waves, and equidensity contours in the variable nozzle flow field. As a supplement to their experimental work, 2-D CFD prediction is also performed and compared with the test results. Good agreement between the test results and CFD predictions are achieved.

The authors define three different flow field conditions that can occur in their setup: Type A, in which the primary flow chokes at the end of the convergent nozzle and the throat of the secondary flow is formed aerodynamically on the divergent flap wall between the shear layer and the divergent flap; Type B, in which the primary flow chokes at the end of the convergent nozzle and the throat of the secondary flow is near the second throat; and Type C, in which the throat of the primary flow is moved downstream of the convergent nozzle, while the throat of the secondary flow is still fixed at the second throat.

The authors conclude that these flow characteristics affect the mass flow rates of both the primary and secondary flows. In Type A, the primary flow is choked and its mass flow rate remains constant regardless of the pressure of the secondary flow. In contrast, the throat of the secondary flow is formed aerodynamically, and its area and position changes as the flow conditions change. This means that the mass flow rate of the secondary flow

is proportional to the distance between the shear layer and the divergent flap. In other words, if the divergent flap is moved parallel to the shear layer, it does not affect the mass flow rate of the secondary flow, whereas if the divergent flap is moved perpendicular to the share layer, the mass flow rate of the secondary flow is changed in proportion to the distance moved.

In Type B, the primary flow also chokes at the end of the convergent nozzle, which keeps the primary mass flow rate constant. As the divergent flap moves upward (increasing the ejector duct area), the area of the secondary flow increases, but the primary flow remains unchanged. On the other hand, as the divergent flap moves downstream, the area of the secondary flow remains unchanged, and the primary flow seems to be stretched downstream. In other words, the mass flow rate of the secondary flow is affected by the vertical motion of the divergent flap and is not related to its horizontal motion.

In the case of Type C flow, the throat area and the mass flow rate of the primary flow are slightly smaller than those of the other types. The throat of the secondary flow is similar to that of Type B, so the mass flow rate of the secondary flow depends only on the vertical position of the divergent flap.

3. Nozzle Lip Thickness

The effect of the primary nozzle base lip thickness on downstream mixing and entrainment has been investigated extensively by several authors. Fabri was the first to account for this phenomenon in supersonic ejectors, which he did by adding a nozzle lip thickness term to his equation for quasi-1D flow analysis. Subsequent research has emphasized its effects not only on shear layer growth, but more specifically on conditions in the primary plume, including plume resonance, steadiness, and symmetry.

Ponton

Ponton and Seiner[22] use acoustic and pressure data to examine the effect of nozzle lip thickness on plume resonance and shear layer growth rate. Using cold flow in an underexpanded sonic nozzle that ejects to ambient conditions, they vary nozzle lip thickness via collars fabricated to fit over the nozzle exit. Pressure ratios are maintained using electronic flow control valves. Acoustic data is recorded using microphones placed throughout the flow field, while pressure data is recorded using pressure transducers at the nozzle lip and pressure probes that move radially and axially along the primary plume and shear layer. The authors conclude that momentum thickness increases with increased lip thickness, which may coincide with increased mixing between the primary plume and ambient air. The result of such increased mixing would also be reduced shock spacing in the primary plume.

In this case, changing the exit lip thickness represents an alteration to the original jet boundary conditions through modification of the external nozzle geometry. Because of this change, the nozzle lip thickness may affect the plume dynamics through an alteration of the initial entrainment and/or through an increased amplification of initial shear layer disturbances. This amplification process may occur with thicker lips because upstream-propagating sound waves in the ambient medium could reflect off the increased nozzle exit area and stimulate the jet.

Kweon

Kweon et al.[23] examine the effect of nozzle exit reflector size (aka nozzle lip thickness) on a pressure-regulated supersonic jet that is discharged from a convergent–divergent

nozzle into ambient air, operating at the range from overexpanded to moderately underexpanded conditions. Data is taken using a combination of pressure measurements in the primary stream/shear layer and a Schlieren system that allows for detailed visualization of the structure of the jet.

The study begins with the observation that any real nozzle that yields a supersonic jet must have a finite lip thickness at the nozzle exit. This thickness can act as a reflector against downstream acoustic feedback, which in turn influences the development of the initial shear layer of the supersonic jet. Consequently as reflector size increases, the structure of the jet plume becomes more asymmetric and oscillates irregularly. However, this result is also strongly influenced by the condition of the rocket plume: for both overexpanded and underexpanded jets, the reflector significantly affects the growth of large-scale turbulent structures in the shear layer of the jet and the turbulent structure-shock interaction, leading to much stronger jet oscillation, enhanced jet mixing, and faster axial decay of the jet. In contrast, when optimally expanded the presence of the reflector at the nozzle exit does not appear to change the jet structure and the resulting acoustic field.

The authors also conclude that exit reflector size seems to reduce the potential core length, defined as the distance measured in the axial direction from the nozzle exit to the location where the inside edge of the jet shear layer merges to a point at the axis. This is again only evident in imperfectly expanded jets, with more of an effect on overexpanded jets than on underexpanded jets.

C.   Previous Works

The Cal Poly Air Augmented Rocket research project is an ongoing effort with the overall goal of investigating the entrainment properties of a 2-D planar air augmented rocket. To date, three theses have been published as a result of this research and two others are pending completion. The original analysis, fabrication, and experimental investigation of the Cal Poly AAR were performed by Foster and Gist. Foster operated the apparatus with hot flow, i.e. combusting flow in the primary stream, while Gist restricted testing to cold flow using compressed nitrogen. Next, Morham developed an automated computer simulation of the Cal Poly AAR test apparatus. Sanchez subsequently modified the apparatus to accommodate a plenum and achieve lower secondary flow stagnation pressures. Popish constructed a Shadowgraph device for flow visualization in the AAR duct. These projects have served as both the primary motivation and technical foundation for the current research.

1. *Foster*

Trevor Foster[24] designed and constructed most of the initial AAR test apparatus. Using methane and oxygen as propellants for the primary plume, he performed hot-fire tests to investigate primary plume expansion and its effects on aerodynamic choking of the secondary flow. Because Foster's investigation was not geared towards thrust augmentation, the primary plume was not fuel rich during these trials – Foster used an oxidizer-to-fuel mixture ratio of 2. The primary stagnation pressure was varied from 325 psi to 1032 psi over a series of four trials, achieving a maximum pressure ratio of 74.

A glass upper surface in the mixing duct downstream of the primary and secondary flows allowed for qualitative flow visualization using an HD video camera, while pressure transducers and thermocouples placed throughout the apparatus were used to characterize the flow and plume behavior on a quantitative level. Foster used Fabri's isentropic quasi-1D analysis with correction factors for nozzle lip thickness and non-isentropic expansion for his theoretical predictions.

Foster drew several conclusions from his testing. First, in comparing his data to results from cold flow nitrogen tests performed under the same conditions and using the same hardware, Foster found that for a given primary chamber pressure, the cold flow tests were more effective at entraining air through the secondary ducting than the hot-fire tests. Foster also concluded that the streamwise location of restriction for the secondary flow in the mixing duct was independent of primary chamber pressure and primary flow temperature. Finally, Foster found evidence indicating that at the highest recorded pressure ratios the secondary flow appeared to be nearing the Fabri limit; however, he was unable to achieve pressure ratios high enough to reduce secondary flow entrainment, which is necessary to prove that the Fabri limit maximum entrainment has been achieved.

2. Gist

Ryan Gist[9] extended the capability of Foster's apparatus by replacing his methane and oxygen primary propellant tanks with modified nitrogen tanks in order to achieve higher primary stagnation pressures and thus higher overall pressure ratios during cold flow tests. Gist achieved a maximum chamber stagnation pressure of 1690 psi and maximum flow rate of 2.8 lbm/s. This yielded a maximum pressure ratio of 115 based on secondary entrainment from ambient air.

The primary nozzle used in Gist's apparatus has an expansion ratio of 10, yielding a primary exit Mach number of 3.92. This high primary Mach number, as well as the two-dimensional planar configuration of the rocket ejector, is what sets Gist's research apart from classic ejector analysis, which typically makes use of axisymmetric designs with low supersonic or sonic primary flow.

Gist's efforts focused on the effect of pressure ratio on entrainment ratio, i.e. the ratio of secondary to primary mass flow rates. Gist also investigated what pressure ratios were required to achieve Fabri choking, the phenomenon in which aerodynamic choking of the secondary stream occurs in the mixing chamber due to the expansion of the primary stream and resulting contraction of the secondary stream.

Gist found that the Cal Poly AAR exhibited Fabri-choking at pressure ratios above 72. Like Foster, Gist used Fabri's analytical approximation based on 1-D isentropic flow to model the Fabri choke and saturated supersonic modes. Gist's model also included an empirical correction to reflect the 2-D nature of the shock structure in the primary plume. Gist's predictions matched experimental results within 12% of experimental uncertainty.

Gist concluded that the transition from Fabri choke to the saturated mode occurs near the optimally expanded pressure ratio, as predicted by the quasi-1D model. He also showed that the highest secondary entrainment (0.32 lbm/s) was obtained in the saturated supersonic mode. Finally, Gist attempted to characterize the shock structure within the primary plume using HD video recordings of the flow; he concluded that the flow visualization supported pressure measurements indicating secondary flow unchoke and the resulting flow field asymmetry.

3. Morham

Brett Morham[25] developed an automated computer simulation, which he called the CPSE Simulator (Cal Poly Supersonic Ejector Simulator), to model the Cal Poly AAR test apparatus. Morham's primary purpose for creating the simulation was to identify the operating conditions which produce the saturated, Fabri choke, and blocked aerodynamic flow patterns. As with Gist, Morham's simulation is geared toward measuring the effect of primary to secondary stagnation pressure ratio on the efficiency of the ejector. The ejector's efficiency is quantified in terms of entrainment ratio.

Morham's CPSE computer simulation operates similar to the analyses presented by Fabri and Addy: first, the primary stream geometry is developed using the Method of Characteristics (MOC). The flow properties in the secondary stream are then determined based on stagnation conditions and the shape of the primary plume using compressible isentropic relations. The primary stream then uses the newly calculated pressure of the secondary stream to produce an updated set of values which approach the final solution. The primary and secondary pressure distributions iterate until the solution does not change considerably, and a final entrainment ratio is calculated.

Morham also makes several additional simplifying assumptions in his simulation, such as: the primary flow of the ejector is assumed to be supersonic, while the secondary (entrained) stream enters the ejector at various velocities at or below Mach 1; the primary and secondary streams are both assumed to be composed of air; the flow is steady and continuous; and viscous forces and thermo-chemical reactions are not considered.

Based on the geometry used by Foster and Gist, Morham found that the saturated flow pattern occurs below stagnation pressure ratios of 74, while the secondary flow of the

ejector becomes blocked by the primary plume above pressure ratios of 230. As a result of these two limiting cases, Fabri choking must occur between pressure ratios of 74 and 230, with optimal operation achieved at the transition from saturated to Fabri choked flow, near the pressure ratio of 74. The case of optimal expansion yields an entrainment ratio of 0.17. Morham's simulation produced entrainment ratio results with an average error of 3.67% relative to experimental data. He concluded that such a level of accuracy in an inviscid simulation would suggest that ejector operation in this regime is governed by pressure gradients rather than viscous effects.

III.   Experimental Apparatus

The materials and equipment described here include everything that was used to test the Cal Poly AAR in its current configuration.   Some portions of the test apparatus, especially the rocket thruster itself, received extensive modifications from its previous configuration, while other elements, such as the plenum chamber, remained virtually untouched. Still other components, like the shadowgraph flow visualization system, were newly constructed additions to the project.   A more complete description of troubleshooting of the test apparatus can be found in Chapter V.

A.   Previous Iterations

The majority of the test apparatus used as part of this project was originally constructed by Trevor Foster and Ryan Gist. Baseline design parameters were chosen based on the proposed ISTAR X-43B RBCC engine, and these early concepts were validated via several analytic and numeric Senior Project investigations in support of the Cal Poly AAR project.

The basic AAR consists of a rocket that produces a supersonic primary exhaust which ejects into a duct, entraining secondary flow from ambient air in the process.   In its original form, investigations were performed using both cold-flow and hot-fire tests. Thus, active cooling methods became necessary in portions of the apparatus that were subject to the intense heating loads experienced during hot-fire tests. As a result, the original nozzle inserts, as well as portions of the rocket chamber and the duct bottom plate, were constructed using copper and incorporated ports through which cooling water could be pumped in order to rapidly move heat away from the rocket. The duct was built

with a divergence angle of three degrees, along with a built-in downward divergence in the bottom plate; both were intended to allow for the expansion that occurs in reacting flow. A glass plate was used as the top portion of the duct in order to visually record the shape of the rocket plume during tests, to check for plume asymmetry, and to observe the shock structure of the primary plume. Pressure taps were also placed along the duct sidewall in order to determine the location of Fabri choking during testing. A semi-exploded view of the original test apparatus is shown in Figure III-1.
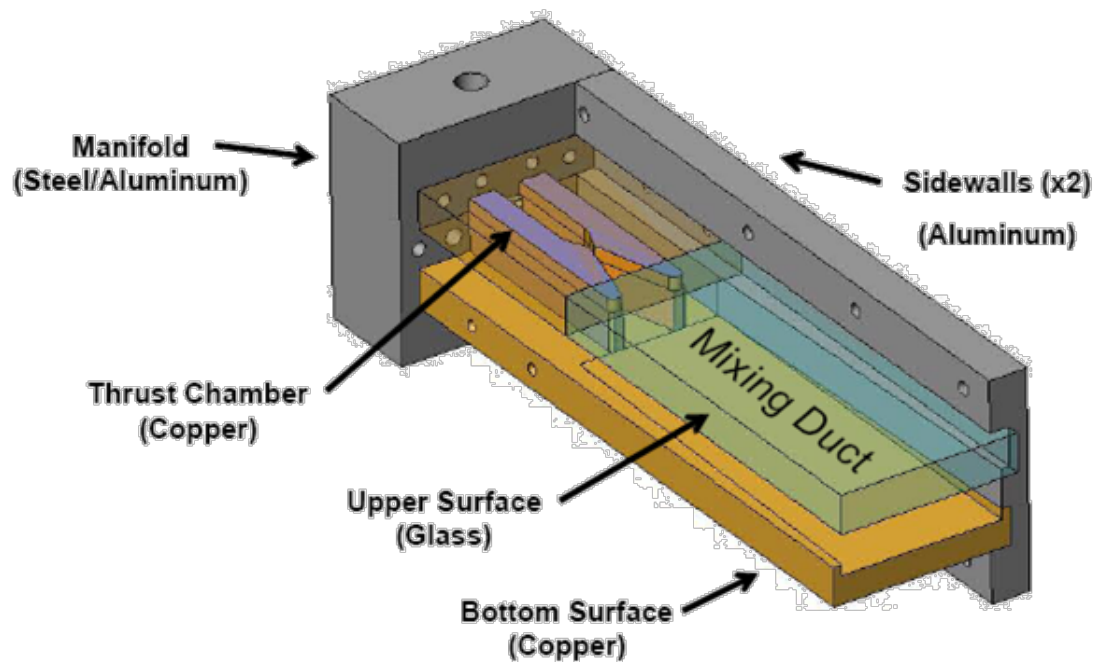
Figure III-1. Original Cal Poly AAR constructed by Foster and Gist[9].

The test apparatus was further modified by Sanchez and Popish. Current tests are limited to cold flow only, so the rocket is not subject to the high thermal loads of hot-fire tests. As a result, all new modifications utilized aluminum components. The mixing duct's length was increased from 14 inches to 18.75 inches in order to ensure that the back pressure at the exit of the duct did not affect upstream flow properties near the primary rocket nozzle exit. This length was calculated based on suggestions from Addy that the

length of the duct be equal to nine times its diameter[12]. The bottom copper plate was replaced by two new, separate components: an aluminum plate between the manifold and nozzle end, followed by three-quarter-inch fused silica glass to act as the upper and lower surfaces of the duct in order to facilitate Schlieren imaging of the flow. Glass plates designed to fit the entire length of the duct proved to be too expensive, so the plates were limited to 14 inches, with aluminum end caps designed to accommodate the remainder of the duct length. Because the Cal Poly AAR is 2-D, the duct's hydraulic diameter was used in this calculation. The duct's sidewalls are made of aluminum, with pressure ports located at 1/8-inch intervals between two and seven inches downstream of the nozzle exit. A view of the modified test apparatus is shown in Figure III-2.
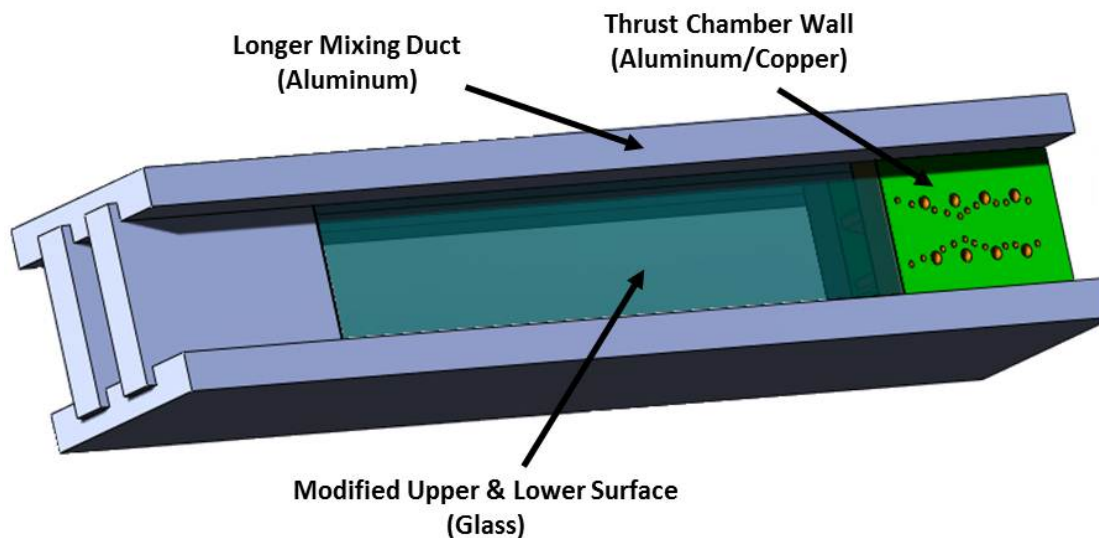
Figure III-2. Modified AAR constructed by Sanchez and Popish[26].

B.   Current Apparatus

The complete AAR test apparatus can be broken up into five distinct elements. The first element is the flow control system. This element controls the flow of primary gases to the AAR, which is necessary for both safety and repeatability of experiments. The

second element is the data acquisition system which is used to measure, record, and process experimental pressure and temperature data taken during a test. The third element is the plenum assembly, which simulates the environmental conditions of a flight-capable AAR during air-launch scenarios. The fourth element is the shadowgraph recording apparatus, which is used to visualize flow inside the AAR duct. The fifth and final element is the primary thruster assembly itself, which simulates components of the propulsion hardware of a flight-capable AAR. A conceptual diagram of the apparatus displaying all of its components is shown in Figure III-3.
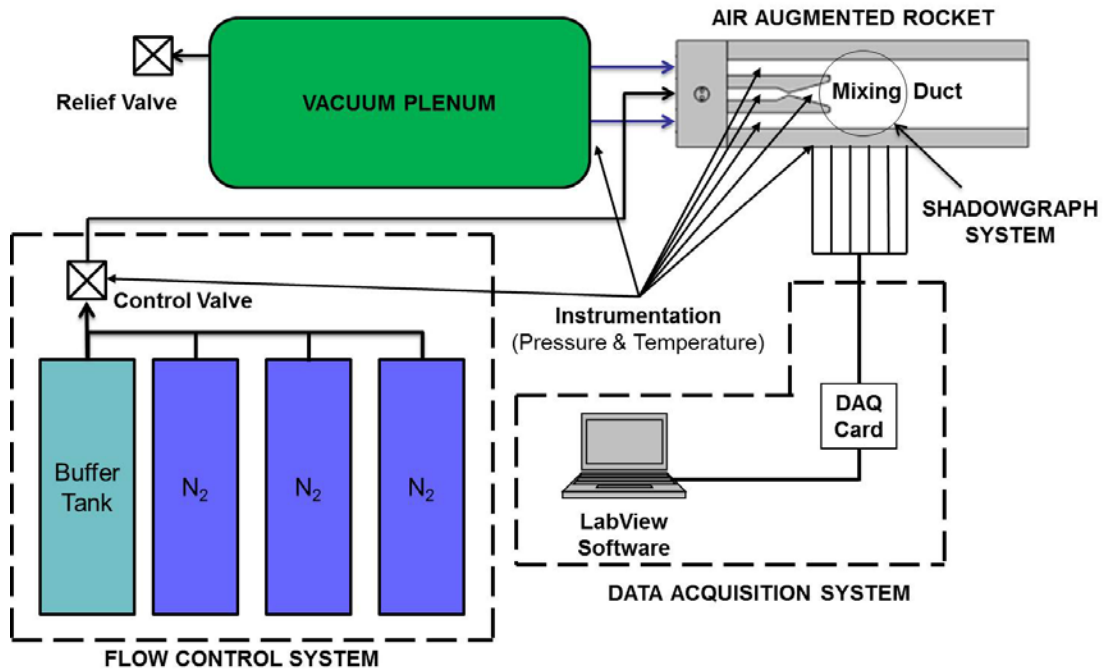
Figure III-3. Block diagram of the current Cal Poly AAR experimental setup.

C.   Flow Control System

The Flow Control System (FCS) consists of the high pressure primary gas supply, supply line plumbing and control units, and the rocket manifold.   The FCS is critically

important to running a successful test, both because of issues related to safety and because repeatable tests scenarios are important for validating test data.

The primary rocket is fed by three high pressure nitrogen cylinders, each starting at 2600 psi and 304 standard cubic feet (scf) of gas. The cylinders are connected via flexible steel hose to a buffer tank with a larger throat area than the supply tanks, which allows for higher mass flow rates. When fully pressurized by the three supply tanks, the buffer tank reaches a maximum pressure of approximately 2150 psi.

One inch diameter type 304 stainless steel pipe is used to connect the supply tanks to the buffer tank, control valve, and remaining feed system. High pressure type 316 stainless steel pipe fittings connect the supply gas cylinders, control valve, and data acquisition ports. The propellant feed line is reduced from 1" to ¾" before it is direct connected into the manifold block. Pipe connections and corners are avoided as much as possible in order to reduce line losses. A pressure transducer located at the control valve is used to monitor pressure drops between the buffer tank and rocket chamber. Leak checks are performed periodically to verify that there are no pressure losses in the lines. A primary feed line schematic is shown in Figure III-4.
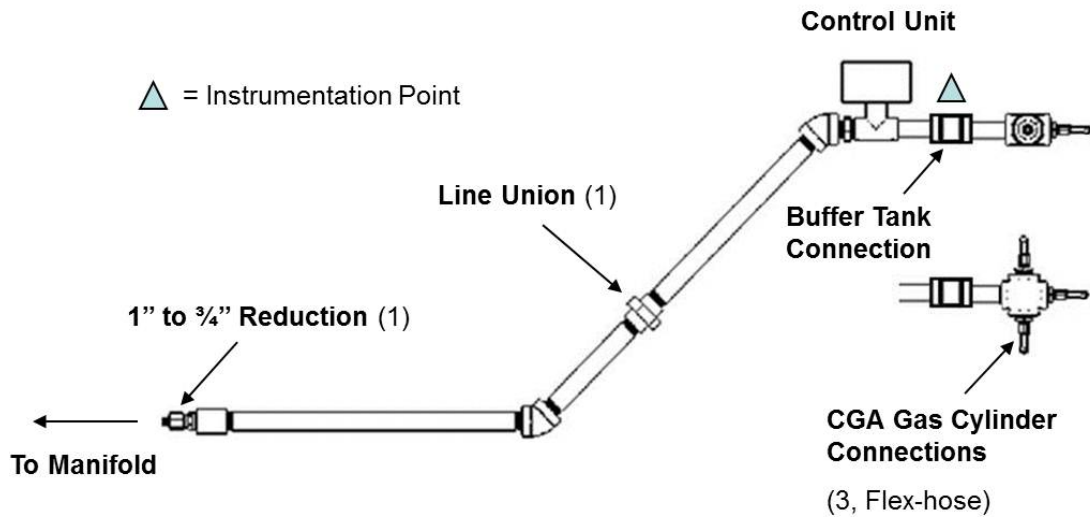
Figure III-4. Propellant feed system schematic.

The propellant feed system is remotely controlled by an active flow control unit. The unit consists of three interlinked components: an Automatic Valve electric solenoid, a Sharpe® SPN-063 "spring return" valve actuator, and an A-T Controls Series-24 1-inch, 3000-psi-rated full-port ball valve. The solenoid is activated via a switch located in the test cell control room. The actuator is pneumatically powered by a continuous supply of compressed air at approximately 100 psi. At the start of a test a voltage signal is sent to the solenoid, which activates the actuator, which then applies a torque to the ball valve and moves it into the *open* position. If the voltage signal or compressed air supply is interrupted, the actuator will spring shut to the default *closed* position. This feature allows for emergency test shut-down in the case of a system malfunction.

D. Data Acquisition System

Currently, there are 23 channels of data that are recorded during a test run. This data includes both pressure and temperature measurements that are collected at various locations within the AAR and its connecting systems. Pressure measurements are

recorded using Omega PX-302 millivolt type pressure transducers. Each transducer recieves a 10 V supply voltage and returns a 0-100 mV signal voltage. The transducers operate at a 1 kHz frequency resolution with an error of less than 0.25% of full-scale readings[28]. Several different pressure transducer models are used based on the pressures they are exposed to. 0-3000 psia models are used in the upstream feed line and primary rocket chamber, while 0-50 psia models are used to record pressure data in the mixing duct, secondary ducts, and plenum.

For temperature measurements, Omega Type K shielded thermocouples are used. These thermocouples do not require both supply and signal voltage to operate, but rather operate via one channel in which the signal changes due to fluctuations in the conductivity of the material with temperature. Type K thermocouples operate over the range from -328 °F to 2282 °F, with less than a 4% drift over the entire range[29].

Each pressure transducer is connected via 1/16 inch stainless steel tubing to a pressure port located along the duct wall, duct lower surface centerline, or primary rocket chamber of the AAR for pressure measurements. A total of 13 taps, spaced along the right wall between 2 and 7 inches downstream of the primary rocket nozzle exit, can be used to collect static pressure data along the duct wall. 3 taps spaced over the same length are located along the left wall in order to verify plume symmetry. 6 pressure taps are placed along the duct centerline, between 0 and 5 inches downstream of the primary nozzle exit, in order to correlate primary plume pressures with wall pressure data. 1 pressure tap and 1 pitot probe are located in the left duct, while 1 pressure tap and 1 thermocouple are located in the right duct. 1 pressure tap and 1 thermocouple are located in the primary rocket chamber. 1 pressure transducer is also located in the plenum. Finally, 1 pressure

transducer is connected to the primary gas feed line at the buffer tank. Figure III-5 shows

all 28 possible locations for pressure and temperature measurement in the AAR setup

(Not pictured: pressure transducers in the plenum and propellant feed line).
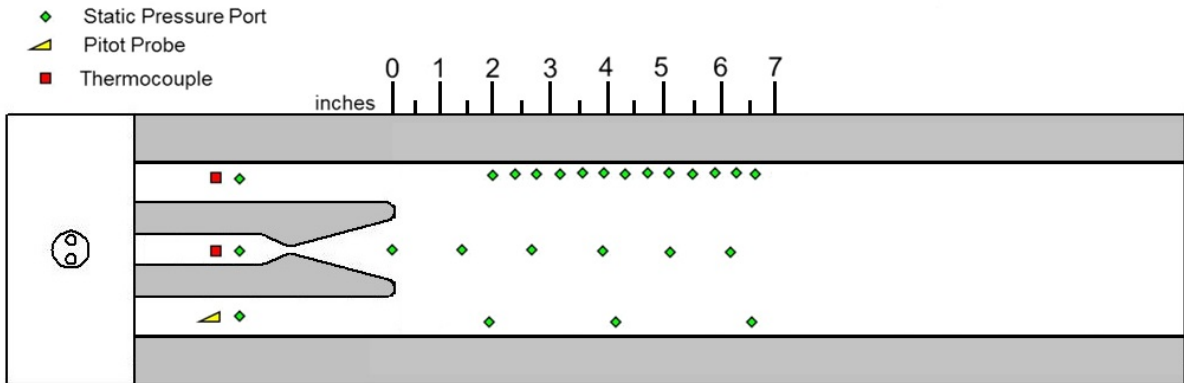
Figure III-5. Thruster instrumentation locations.

Signals from the pressure transducers and thermocouples connect to a National

Instruments (NI) SCXI-1303 32-channel terminal block. The terminal block is housed in

a protective NI SCXI-1000 chassis that provides power to the terminal. The output signal

from the terminal runs to a laptop computer via a PCMCIA DAQ card-6036E.

Once the signal reaches the computer, it is processed and recorded using the software

program LabView, a graphical user interface (GUI) that allows the user to set up data

channels, perform calibrations, and select data recording settings. The current LabView

file used to collect data was created by Sanchez based on modifications to the original

code created by Gist[26]. During a test run, the LabView code is set to record data at a rate

of 50 Hz, which was selected based on a compromise between data size and resolution.

LabView logs this data to an Excel Spreadsheet, which is used in further analysis.

E.   Plenum

A plenum chamber was built by Joey Sanchez in order to reduce the pressure of the secondary flow during tests, with the intent of achieving higher pressure ratios between the primary and secondary flow. The plenum is made of a structurally-reinforced steel oil drum, as shown in Figure III-6.

Because the plenum is direct-connected to the secondary ducts of the AAR, it can't be pulled down in pressure prior to a test. Rather, pressure reduction is achieved during the test via the shear forces of the primary flow on the secondary gases. This makes the test inherently unsteady and transient, as the pressure ratio

Figure III-6. Plenum internal structure.

between the two flows is constantly changing.

Early tests implemented flexible tubing to connect the plenum to the rocket. However, because these tubes became the narrowest point between the plenum and mixing duct, the flow choked there first, limiting the mass flow rate into the duct. A solution was eventually developed in which aluminum tubing having the same inner geometry as the secondary ducts was used as a direct connection between the plenum and the AAR. Inlet air horns were placed at the opening of the ducting into the plenum, allowing air in the plenum to enter the ducts more smoothly and increasing the entrained mass flow rate.

F.   Shadowgraph Apparatus

The primary objective of this investigation has been to develop a better understanding of the viscous effects of nozzle lip thickness on mixing and entrainment in the Cal Poly AAR. Flow visualization is a fundamental method for quantifying viscous interactions, so a shadowgraph apparatus was built in order to achieve this objective.

1. *Schlieren vs. Shadowgraph*

Schlieren and shadowgraph photography are methods for visualizing density varations in fluid flow. In concept, they rely on changes in the refractive index of air across large pressure gradients, such as may exist in supersonic flows. In the case of both Schlieren and focused shadowgraphy methods, the system begins with a single collimated source of light. When that light is placed at the focal point of a concave mirror, parallel light rays are reflected. If this parallel beam is then focused onto a second concave mirror, the reflection from that mirror can be focused onto a viewing surface. When density gradients are present in the fluid passing between the two mirrors, the varying refractive index of the fluid will cause disturbances in the parallel light beams. The image projected off of the second mirror will reflect these disturbances, which appear as 'streaks' or 'schlieren'[30] on a viewing surface or photograph.

The main difference between Schlieren and shadowgraph systems is in what density gradients are shown and what are not.   In Schlieren photography a knife-edge is placed at the focal point of the second mirror, positioned to block roughly half of the projected light. In flows with uniform density this will simply make the photograph half as bright. However, in flows with density variations the distorted beam focuses imperfectly,

projecting two overlapping images: one image showing density gradients in the direction parallel to the knife edge, and one image showing density gradients perpendicular to the knife edge. The knife edge thus acts to intercept and remove density gradients parallel to it from the final image, leaving only an image containing light and dark patches corresponding to positive and negative fluid density gradients in the direction normal to the knife-edge.

The term 'Schlieren' is typically only applied to systems which implement the knife-edge technique; by removing the parallel density gradients, it measures the first derivative of density. If a knife-edge is not used the system is generally referred to as a shadowgraph and the image as a shadowgram; it which measures the second derivative of density.

2. *Shadowgraph System Construction*

In order to visualize the viscous flow interactions between the primary and secondary airstreams in the AAR, a focused shadowgraph system was built around the AAR test stand. The current system is an evolution of an earlier attempt at building a Schlieren apparatus for the same project by Martin Popish which yielded insufficient images of the flow field under investigation. Popish's system was itself a modification of earlier apparatuses built as senior projects for the Aerospace Engineering department at Cal Poly[31].

Popish's setup yielded poor images due to several factors. Chief among these was that the system used a simple red LED as the light source for flow visualization. The luminous intensity of this light source was several orders of magnitude lower than is necessary for most high speed flow applications. The system was also entirely self-enclosed, preventing outside light from entering the path of the illuminating beam;

because it was originally designed for use in undergraduate wind tunnel labs, this allowed for daytime use. However, when used in this way on the current setup, the structure had to be mounted directly onto the walls of the AAR mixing duct. Such mounting produced significant vibrations on the system during testing, which contributed to the overall poor image quailty of the pictures. Being self-contained also prevented the system's mirrors and glass test section from being cleaned regularly; this made dust buildup on the mirrors an additional factor in reduced image quality. The Schlieren enclosure also severely limited mirror calibration because of the way the mirrors were mounted inside the PVC structure.

Finally, one of the biggest reasons for poor image quality was the placement of both the illuminator and analyzer beams on the same side of the test section. A typical setup for both Schlieren and focused shadowgraphy is called the Z-type system because it resembles the letter 'z', with the light source on one side of the test section and the image projection on the other side. This setup is used in order to offset the effects of coma on the quality of the image. Coma is the result of off-axis mirror use: when the optical and geometric axes of the mirror are not coincident, as must be the case in a focused shadowgraph setup if the light source is not on the same axis as the test section (which it can't be), different annular zones of the mirror-face focus at different points along the subsequent reflection. This results in the original point light source being smeared into a region of flare with a bright core at one end. The Z-type system cancels this effect by tilting the mirrors at equal angles in opposite directions. Thus, by placing both beams on the same side of the test section, the effects of coma were doubled in the original setup rather than cancelled out.

Constructing the focused shadowgraph system proved difficult due to the limited space available in the test area and the relative immobility of the test apparatus. Typical Schlieren and shadowgraph systems are constructed in such a way as to place all of the elements on the same horizontal plane, often on an optical bench, in order to make calibration easier. This was not possible with the AAR because of its configuration, which only allowed for flow visualization on a vertical plane; therefore, all elements in the system had to be aligned in the same vertical plane.

The system was originally intended to be used for Schlieren visualization, not shadowgraphy, and was constructed with that in mind. A knife edge was set up perpindicular to the analyzer axis and a special platform was built to accommodate the heights necessary for a camera to capture the projected image (a result of the unique setup built around the AAR and the focal length of the mirrors was that the image focused at over six feet off the ground, higher than most conventional tripods). A relatively standard JVC 930C GZ-MG730U camcorder with a 7 Megapixel CCD image sensor and 10X zoom capability was initially used to record the tests, but the images produced were of poor quality because the camera was unable to focus properly on the projected image.

Eventually a higher quality, high-speed HD video recording device was acquired from the Cal Poly Mechanical Engineering department. Using this camera, along with available 50 mm, 55 mm, 85mm, 105 mm, and 170 mm macro and zoom lenses, multiple attempts were made to produce a better focused image of the AAR test section. Attempts were also made to project the test section image directly onto the camera's CMOS image sensor, although these also yielded poorly focused images. Ultimately, it was determined

that setup would need two major upgrades in order to produce a satisfactory Schlieren image: a more powerful xenon flashtube light source capable of producing light intensities one or two orders of magnitude higher than the current lamp, and a custom lens designed based on the focal length of the mirrors used in this setup which could produce a properly focused image on the camera's CMOS image sensor. The costs associated with these upgrades greatly exceeded the AAR project's budget (a new xenon flashtube would cost an estimated $17000 alone), and so alternative solutions were pursued.

Based on a low-cost solution pursued by another group faced with similar budgetary constraints[32], the Schlieren concept was eventually discarded in favor of a focused shadowgraph method. Instead of trying to project a focused image onto the camera's sensor, a semi-transparent viewing surface was constructed and mounted on the analyzer axis between the second mirror and its focal point, at the location where the image appeared to be the sharpest. The image is thus projected directly onto the viewing screen without using any additional focusing optics, with the camera placed on the opposite side. As shown in Figure III-7, the system in its final form consists of a light source, condenser lens, source slit, two concave spherical mirrors, a semi-transparent viewing screen, and a high speed HD video camera.
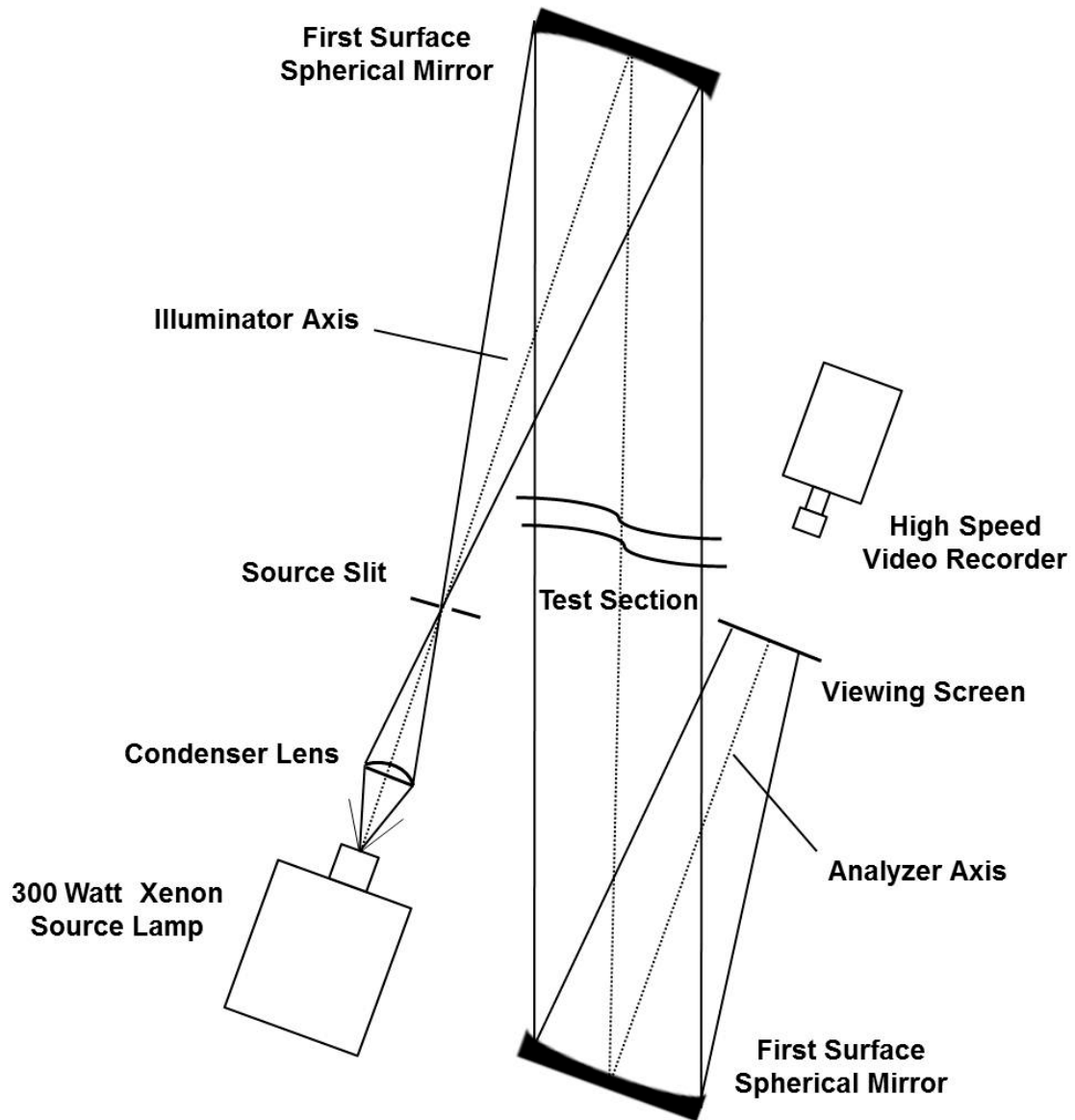
Figure III-7. Shadowgraph system schematic.

The apparatus uses two first-surface spherical F10 mirrors with 1/8 wave surface accuracy, overcoated with silicon monoxide. The mirrors are 6 inches in diameter with a 60 inch focal length. Mirror mounting and adjustment is accomplished via a heavy-duty steel telescoping tube structure built especially for this project. The steel frame is mounted on a 6 inch x 6 inch steel base that is bolted to the concrete floor of the test section in order to minimize the effects of vibration on mirror orientation during testing.

The main steel post is approximately 8 feet tall, with 3 foot arms extending from the post above and below the AAR mixing duct. Perforations spaced along both the arms and post allow for incremental adjustments of the mirrors in order to center the mirrors over the test section and adjust their heights to accommodate for their focal lengths between the light source and image projection, respectively. Two U-shaped brackets were constructed to provide structural support and an additional two-axis rotational ability for each mirror. In total, the mirror-mounting structure provided five degrees-of-freedom for mirror translation and rotation, which resulted in excellent mirror calibration.

Light for the Schlieren apparatus is provided by an Olympus model CLV-A 300 Watt xenon short-arc lamp. Light intensity in the lamp can be adjusted in 17 increments, with a maximum luminous flux of 6000 lumens. A 50 mm diameter x 44 mm focal length condenser lens was used in combination with the xenon light source in order to collimate the light from the lamp into a straight beam to more evenly illuminate the mixing duct test section. Brackets on the back of the lamp box are mounted on a steel rod, which allows the lamp to rotate about the rod without translating in any direction. Thus, once the lamp has been brought into the same vertical plane as the mirrors, it can be rotated along the axis of the rod until it makes an appropriate angle with the first spherical mirror.

The viewing screen that the final image projects onto is simple tracing paper mounted on a cardboard frame. The frame is supported by a U-shaped bracket similar to those used to support the system's mirrors, with the bracket mounted onto the same structural arm as the second mirror. Thus, the viewing screen has five degrees-of-freedom for rotation and translation, just like the mirrors. Finally, video recording of tests is performed using a

Vision Research Phantom v310 high-speed camera, which has 1 Megapixel image clarity, is capable of recording up to 500,000 frames per second (fps), and can use exposure times as low as 1 microsecond. Current tests record at a rate of 300 fps, at exposure times between 300 and 1000 microseconds. A 50 mm Canon camera lens is used to focus the camera onto the viewing surface.

G. Primary Thruster

The main experimental hardware is the thruster assembly itself. The thruster consists almost entirely of aluminum components due to the fact that all current experiments focus on cold flow testing, which eliminates the need for high heat-enduring materials. Only one stainless steel element remains, that being the manifold component that links the thruster to the stainless steel primary feed line. Figure III-8 depicts the thruster assembly and all pertinent dimensions. The primary chamber, secondary ducts, and mixing duct all have a constant height of 0.75 inches.
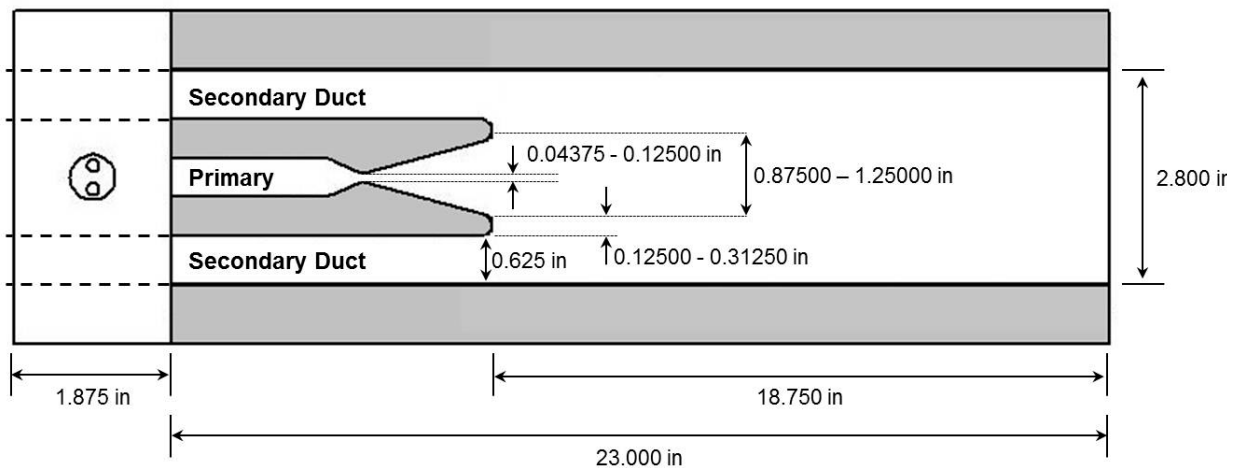
Figure III-8. Thruster assembly dimensions – top view.

The nozzles used in this experiment are based on the original nozzles used in the AAR at the time of its design. The original nozzles (made of ¾" thick alloy 110 copper bar stock,

with cooling channels in order to provide active cooling during hot-fire tests) were simple conical nozzles with an area ratio of 10 and divergence angle of 15.35°. The nozzles had a base lip thickness of 0.25 inches and throat area of 0.075 in^2.

1. *Nozzles*

The primary research goal for this thesis is to examine what changes may occur in the flow field of the Cal Poly AAR mixing duct when the original nozzles designed for the project are switched out for new ones. To that end, the first change made was to convert the nozzles to a bell contour shape from the original conical design.

Conical vs. Bell-Mouth Nozzles

The only two nozzle geometries in wide use today are the truncated cone and the bell contour. The principal difference between these two configurations is found in their diverging supersonic flow sections. In contrast, the converging nozzle section between the chamber and the nozzle throat is not critical to achieving high performance in either design. The subsonic flow in this section can easily be turned without a considerable pressure drop and thus any radius, cone angle, wall contour curve, or nozzle inlet shape is satisfactory. Neither is the throat contour very critical to performance, meaning that any radius or other curve is usually acceptable. The pressure gradients are high in these two regions and as a result the flow will adhere to the walls.

The conical nozzle is the oldest and simplest of all nozzle configurations, largely due to its relative ease of design and fabrication. It was chiefly for this reason that Foster and Gist originally decided to use one in their test apparatus. Conical nozzles yield nearly uniform exit velocity, but the flow angle varies from zero at the axis to the cone half-

angle at the wall. This introduces flow divergence, which reduces the total momentum of the exhaust in the axial direction. Thus a small nozzle divergence angle causes most of the momentum to be axial and as a result gives a high specific impulse, but also makes the nozzle longer and heavier. A large divergence angle in contrast makes the nozzle shorter and lighter, but with a reduction in axial exhaust momentum. The optimum conical nozzle shape and length is typically assumed to be between 12 and 18 degrees half angle – Foster and Gist chose a half angle of 15.35 degrees, almost exactly halfway between these two limits.

The bell nozzle is probably the most common nozzle shape in use today. It has a high angle expansion section (20 to 50°) right behind the nozzle throat, which is followed by a gradual reversal of nozzle contour slope so that at the nozzle exit the divergence angle is small, usually less than a 10° half angle. It is possible to go to large divergence angles immediately after the throat because the large pressure gradient that exists there does not allow separation to occur in this region unless there are discontinuities in the nozzle contour. A bell nozzle is more efficient than a simple straight cone of similar area ratio and length, because its wall contour is designed to minimize losses via the Method of Characteristics.

In concept, an ideal nozzle will direct all of the gases generated in the combustion chamber and accelerated by the throat to exit along its axis. This maximizes the exhaust's axial momentum and thus the thrust produced by the rocket. However in any real nozzle, the exhaust gases have some finite amount of non-axial momentum. In a bell nozzle designed via the Method of Characteristics, the nozzle expands rapidly immediately after the throat, causing expansion waves to form as the gases move out of

the throat. The nozzle geometry then slowly curves back in to give a nearly straight flow of gas at the nozzle exit plane. However, reversing the nozzle's slope like this causes compression waves to form. If designed properly, the bell nozzle's contours will force these two sets of shock waves to coincide and cancel each other out, thus minimizing energy losses in the rocket's exhaust.

Nozzle Design Process

Nozzle designs were created using the software program NOZZLE[33], a one-dimensional (with cross-sectional area variation) compressible flow computer program for the analysis of converging-diverging nozzles. Once a basic cross-sectional nozzle shape (such as conical, bell-mouth, parabolic, etc.) is specified, the program takes input parameters including chamber temperature and pressure, exit pressure, nozzle length, throat diameter and location, throat radius, exit diameter, and divergence angle, and using either the Method of Characteristics or the MacCormack Finite Differences Method creates a nozzle profile that maximizes the efficiency of the design. The program has the capability to simulate a variety of both hot-flow exhaust gases (such as liquid oxygen and hydrogen) and cold-flow gases such as nitrogen (as is currently used in the AAR setup). The Nozzle GUI is shown in Figure III-9.
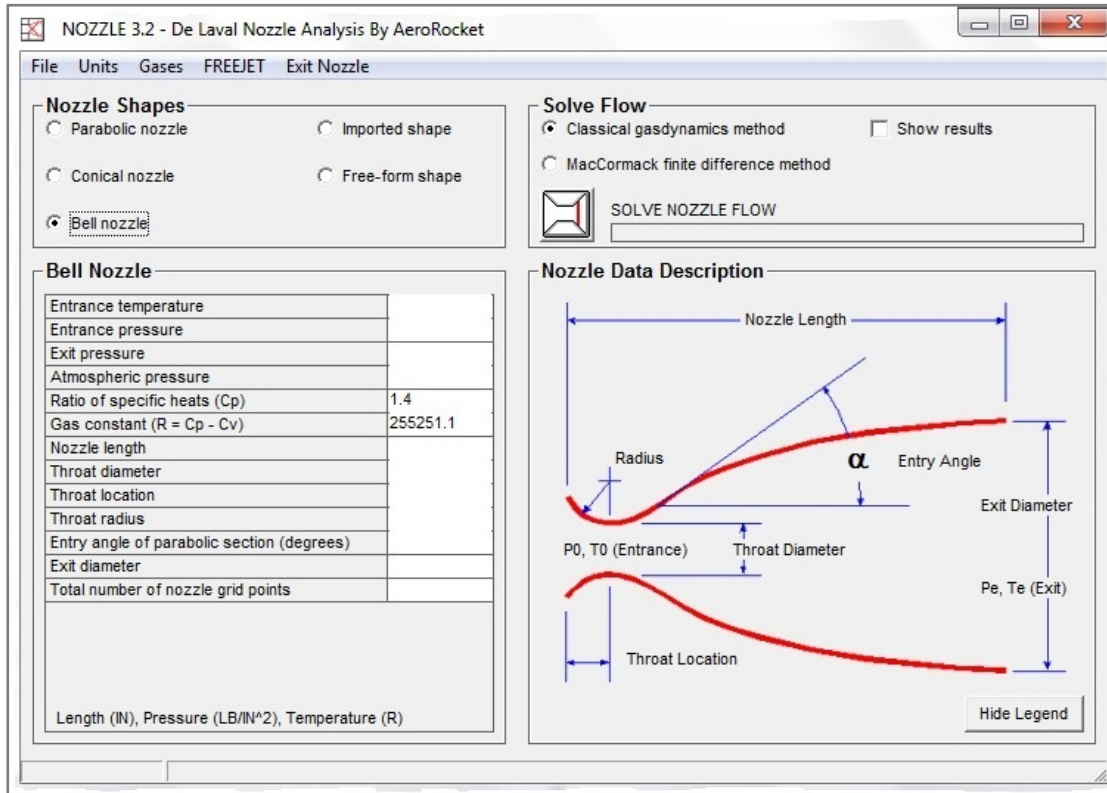
Figure III-9. NOZZLE design GUI.

Once the program has solved for a nozzle contour, the data can be saved to an Excel file containing a user-defined number of x- and y- data points and corresponding pressure, temperature, and density ratios and Mach numbers. However, the program assumes an axisymmetric nozzle geometry, which makes any of these additional flow characteristics invalid when the nozzle contour is applied to a 2-D setup such as the Cal Poly AAR.

The next step in the nozzle design is importing the new bell-mouth curve to SolidWorks©. An existing nozzle part file based on the original conical nozzle inserts used in the Cal Poly AAR serves as a basis for the new nozzle designs. Because the nozzle inserts must fit into the existing AAR manifold, the upper and lower portions of the inserts must maintain the same profile as the originals; only the portion of the insert that is exposed to the flow field is changed to the new bell-mouth contour. An example of a new nozzle insert is shown in Figure III-10.

Primary combustion chamber

Bolt holes

Recessed into top/bottom plates

Bell-mouth contour

Varying lip thickness, throat/exit area
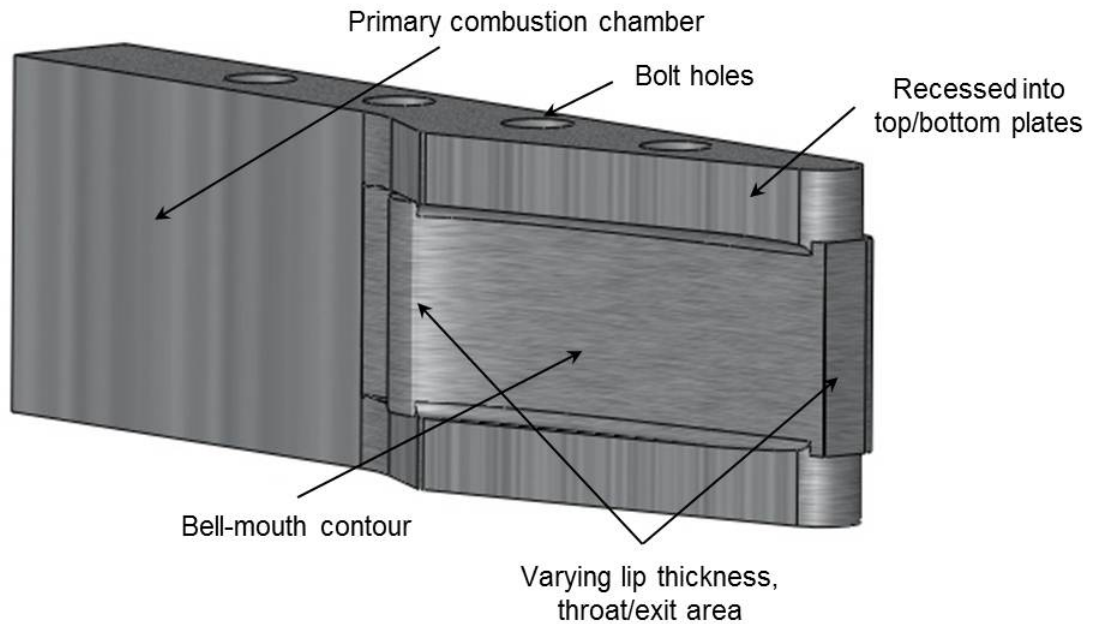
Figure III-10. Nozzle insert showing new contoured design.

Nozzle Manufacturing

The original goal of this project was to incrementally change two variables in the nozzle's design in order to determine their impact on the resulting flow field interactions between the primary and secondary streams in the AAR mixing duct. Because this phase of testing would be restricted to cold flow experiments, grade 6061 aluminum was selected as the nozzle material because of its easy machinability, superior strength over the previous copper nozzle inserts, and relative cheap acquisition cost. The first three nozzles were intended to maintain the same area ratio of 10 that the original nozzle inserts were designed for, while varying the base thickness of the nozzle lip between the original design dimensions and the smallest manufacturable lip thickness. A thin nozzle lip is desirable because it most closely approximates a splitter plate, which is the instrument used in most shear layer research and thus serves as a basis for most of the

analysis in this work[16]. Based on discussions with a manufacturing engineer at Cal Poly[34], it was determined that the thinnest nozzle lip that could be reliably machined was 1/8 in. Beyond that limit, it was likely that the CNC machine bit would shred the aluminum nozzle material. Thus, the three nozzle lip thicknesses selected were 0.25 in (to coincide with the original conical design), 0.125 in., and 0.1875 (halfway between the first two, in order to provide a third data point for more accurate interpolation based on the experimental results).

The second set of nozzles was designed to vary lip thickness in the same increments as the first set but at a different area ratio and thus different primary Mach number. This would provide an additional set of evidence for the same lip thicknesses at a different primary velocity relative to the secondary flow.

Several obstacles were encountered during the nozzle manufacturing process. Chamfers had to be added to several portions of the new nozzle curve in order to make the interface between it and the existing curves machinable. Special attention was paid to making the wall surface throughout the nozzle as smooth as possible in order to minimize friction losses due to surface roughness. However, even with machining tolerances of a few thousandths of an inch, the final bell contour of the nozzle contains finite, linear slope changes that prevent it from being perfectly isentropic and contribute to the formation of shocks in the nozzle, a topic that will be discussed more in-depth in the experimental results section. Finally, machining tolerances proved to be extremely important in producing nozzles that fit into the manifold plates properly: if off by more than a few thousandths of an inch, the nozzles were either too large to fit or too loose to produce a

good seal when the thruster was assembled. Ultimately, each nozzle had to be finalized by hand in order to achieve a proper fit.

Nozzle Throat Issues

According to Sutton[35], when a rocket's combustion chamber cross-section is larger than approximately four times the throat area, the chamber velocity can be neglected. However, below this number the flow's velocity in the chamber will affect pressure buildup: the gases in the chamber expand more if the velocity is not reduced by a small throat, so the energy used to accelerate the expanding gases towards the throat will cause a pressure drop and additional energy loss. Because of this energy loss, the chamber pressure is lower at the nozzle entrance than it would be if this ratio had been larger.

Initial experiments using the first three nozzles, all with chamber-to-throat area ratios of roughly 3.6 to 5.0, were unable to achieve chamber pressures high enough to produce useful results. These issues are discussed further in Chapter V. The important conclusion from this testing was that the throat areas of these nozzles fell too close to the threshold and thus could not produce sufficient pressure buildup in the chamber. This led to some confusion as to how the nozzle used during the tests performed by Sanchez and Popish could have successfully reached high chamber pressures. Upon closer inspection, it was discovered that Sanchez and Popish had used a modified nozzle with very different characteristics than the ones originally designed by Foster and Gist. This nozzle had a throat area of 0.0338 in^2, yielding an area ratio of roughly 22.3, more than double the originally designed value of 10. The first test of Nozzle B3, with a larger area ratio and thus smaller throat area, produced much higher chamber pressures without any other

changes to the setup. This confirmed that a large throat area was indeed the cause of the poor results with the other nozzles.

As a result of these conclusions, it was decided that the first three nozzles would not yield good data and so were discarded from future tests. This meant that the present work would shift attention away from the effects of area ratio and instead focus solely on examining the effects of lip thickness on the AAR's performance, as the remaining nozzles all have the same area ratio. An additional nozzle was created with a thicker lip than the baseline version used by Sanchez and Popish, in order to investigate designs on both sides of the thickness spectrum. A matrix of the seven nozzle designs, along with the conical versions used by both Foster and Gist (F&G), and Sanchez and Popish (S&P), is shown in Table III-1 together with all important dimensions.

Table III-1. Nozzle insert dimensions.

	Expansion Area Ratio (ε_e)	Average Mach Number	Lip Thickness (inches)	Throat Width (inches)	Exit Width (inches)	Contraction Area Ratio (ε_c)	Max Turning Angle	Exit Angle
Nozzle A1	9.1	3.49	0.135	0.138	1.253	3.62	57.7	10.3
Nozzle A2	9.2	3.41	0.189	0.123	1.136	4.07	54.6	9.3
Nozzle A3	10.0	3.54	0.258	0.100	1.001	5.00	50.7	8.2
Nozzle B1	19.8	4.57	0.130	0.063	1.250	7.94	70.1	10.4
Nozzle B2	19.8	4.37	0.196	0.057	1.128	8.77	67.6	9.3
Nozzle B3	19.3	4.39	0.253	0.052	1.006	9.62	64.6	8.3
Nozzle B4	19.0	4.34	0.312	0.046	0.876	10.87	60.8	7.3
Nozzle C3 (F&G)	10.0	3.92	0.254	0.100	1.004	5.00	15.4	15.4
Nozzle C3 (S&P)	22.3	4.29	0.254	0.045	1.004	11.11	15.4	15.4

IV.   Theoretical Analysis

The theory used in this research serves as an important predictive tool to compare against any data collected through experimental work. The primary theoretical method, a 2-D inviscid simulation, was used to quantify the expected performance of the ejector using each nozzle design.

A.   CPSE Simulation

As described previously in the literature review, a 2-D, inviscid computer model of the AAR mixing duct flow field was built in MATLAB by Brett Morham in order to provide a predictive capability to the Cal Poly AAR project. The simulation was named CPSE Simulator, for Cal Poly Supersonic Ejector Simulator. The CPSE simulation uses the Method of Characteristics to predict the structure of the primary plume, while the secondary flow is modeled using 1-D, isentropic relations. A pressure-matched boundary condition is imposed on the boundary between the primary and secondary flows, and the secondary flow is assumed to choke at the point of minimum area.

At a fundamental level, the model uses isentropic area relations to calculate the area of the secondary flow based on the shape of the primary plume calculated using the Method of Characteristics. The point of maximum primary plume expansion is modeled as the point of minimum area for the secondary, and thus the location where the secondary flow chokes. This relationship is highlighted in Equation 4-1.

$$\frac{A_{si}}{A_s^*} = \frac{1}{M_{si}}\left(\frac{2}{\gamma+1}\right)\left(1 + \frac{(\gamma-1)M_{si}^2}{2}\right) \tag{4-1}$$

In Equation 4-1 the subscript "s" refers to the secondary flow, while the "i" indicates conditions upstream of the choke point, and the star represents conditions at the choke point.

Static pressures in the secondary flow are found using the Mach numbers produced from Equation 5-1. Once the pressure distribution in the secondary is calculated, the pressure-matched boundary condition is applied to the plume boundary and the process is repeated until it converges to a solution. Figure IV-1 shows Mach number distributions in the AAR mixing duct for a converged solution of the Fabri Choke case using the CPSE simulation.
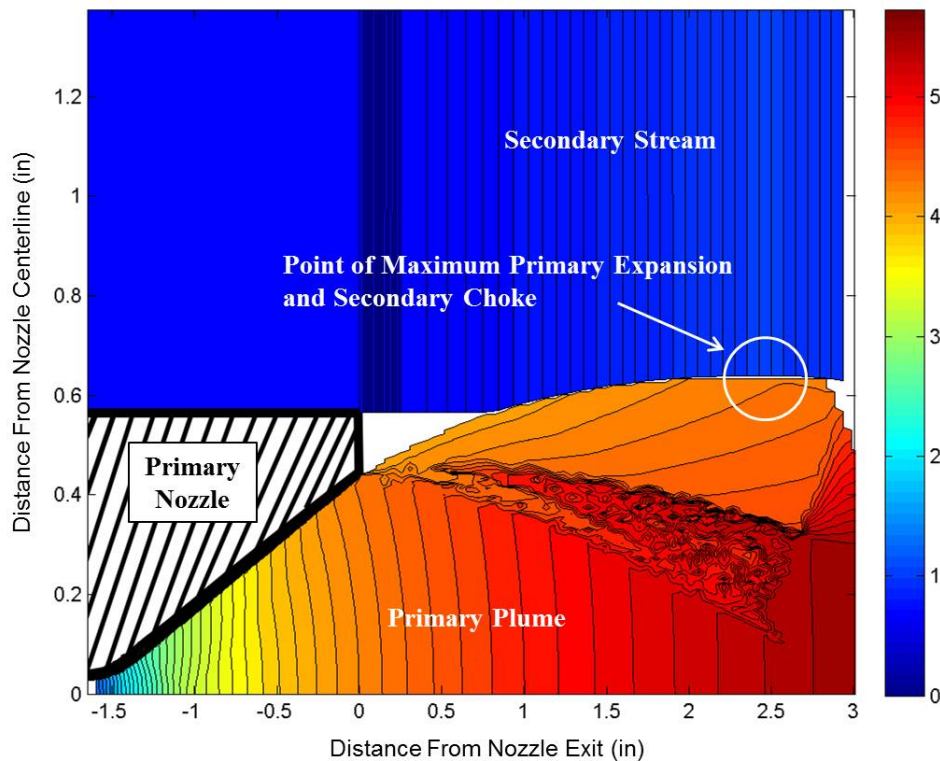
Figure IV-1. CPSE simulation of mixing duct Mach number distribution, PR = 124.

The CPSE simulation was validated against both quasi-1D predictions and experimental results produced by Gist. The average error between the CPSE numerical simulation and the experimental data from Gist was 3.67%[25]. The excellent agreement between the model and experimental data is best demonstrated in terms of their performance results;

ejector performance is generally measured in terms of entrainment ratio as a function of stagnation pressure ratio. Figure IV-2 presents a performance comparison between experimental data, quasi-1D predictions, and the results of the CPSE simulation.
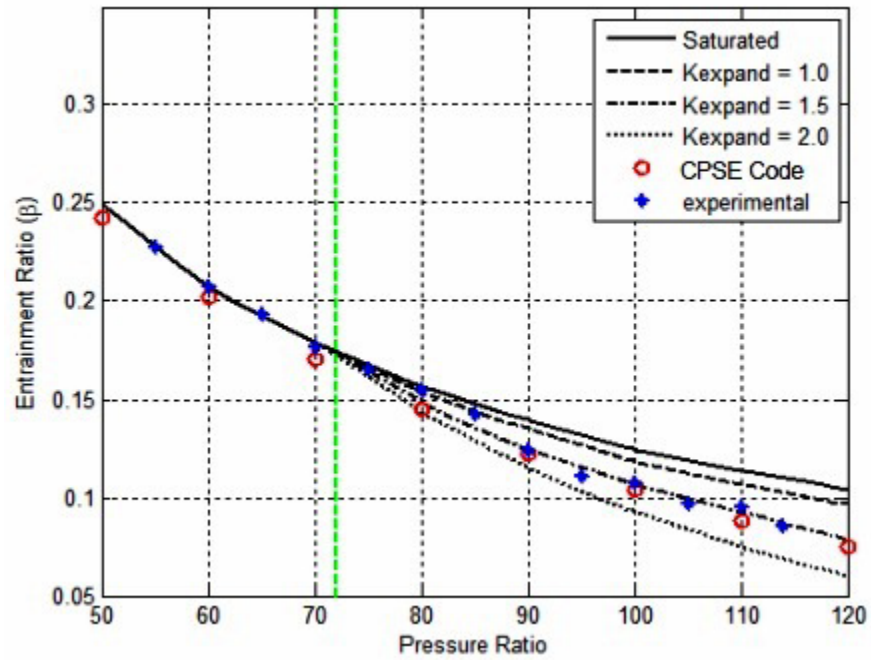
Figure IV-2. Comparison of CPSE model with empirical and experimental data[25].

V. Initial Cold Flow Testing and Issues

Initial testing of the new nozzles occurred at the same time as final testing of the original nozzles used by Sanchez and Popish. These tests served as preliminary validation of the new centerline pressure configuration, which was constructed in order to supplement visual flow-field data with additional pressure data from the primary rocket plume. The addition of a centerline configuration would also allow for comparison against the data collected by Foster and Gist, in order to verify that the primary plume was consistent with its performance during their tests.

Several problems were encountered during the initial tests. The most critical of these problems was the rocket's consistent inability to achieve Fabri-choking. From the data it was apparent that this poor performance was due to low chamber pressures in the primary rocket, but the cause behind the low pressures was less obvious. Several sources were considered, including leaks in the thruster assembly and primary feed system. It was ultimately concluded that these issues were the result of both malfunctions in the primary feed system and problems with the newly constructed nozzle inserts.

A. Primary Feed System Malfunction

As was discussed previously in the apparatus section, the propellant feed system is remotely controlled using a system that consists of an electric solenoid, valve actuator, and ball valve. The solenoid is activated via a switch located in the test cell control room, which causes the pneumatic actuator to open the ball valve. Over the course of their tests, Sanchez and Popish noticed a trend of decreasing performance from the ball-valve system. Specifically, the length of time necessary for the ball valve to open fully at

the start of a test kept increasing. Fortunately, the reduced performance associated with this delay did not cause any immediate issues; the valve could fully open within approximately 1-2 seconds, which still allowed for a sufficiently large pressure buildup in the primary nozzle chamber.

However, during Tests 34-39 the ball-valve became a significant source of pressure loss between the propellant tanks and primary rocket chamber. Predicted line losses between the tanks and primary chamber were calculated to be on the order of 100 psi; however, pressures recorded during testing indicated over 1000 psi lost to some other mechanism in the propellant feed system. In addition, the trend in pressure decrease between the tank and rocket chamber was very abnormal. For a fixed orifice, the tank pressure should always drop more sharply at the beginning of a test (high pressure = high flow rate) and then taper off asymptotically as the pressure falls. However, during these tests the pressure followed the opposite trend (slower pressure decay at higher pressure). It thus became apparent that the area through which the primary flow moved was changing throughout the test, which seemed to indicate a valve positioning issue. The valve was confirmed as the source of the trouble when the length of time between different tests was compared – abnormal pressure curves coincided with tests on the order of 15-30 seconds, versus the typical 6-8 second length of more normal tests, indicating the the valve was sticking as it opened during the test.

Ultimately, replacing the ball valve solved the largest of the pressure loss issues. Figure V-1 compares pressure drops for a malfunctioning valve against a later test using the new valve. As the figure shows, the new valve not only produces a rapid pressure spike and drop in the chamber as predicted, but this also occurs over a much shorter time span.
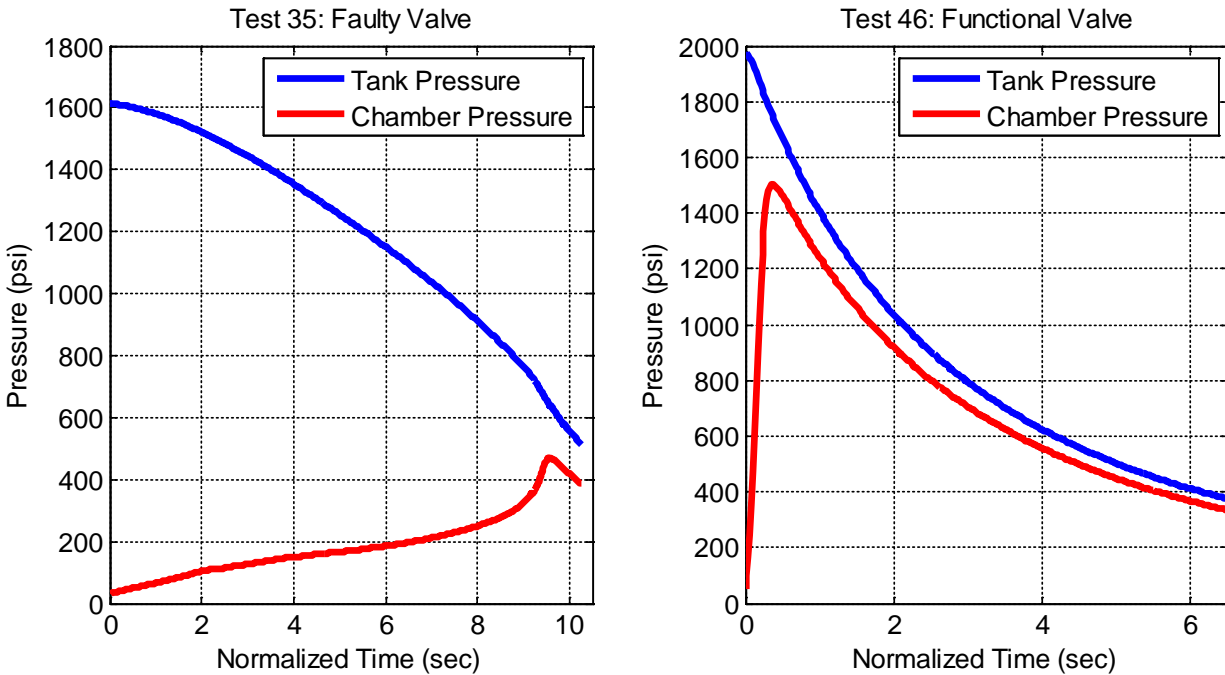
Figure V-1. Pressures resulting from malfunctioning vs. properly functioning valves.

B.   Pressure Losses Due to Throat Area

After the faulty ball valve in the primary feed system was replaced, chamber pressures increased significantly from Test 40 onward.   However, these values were still considerably lower than those achieved during the tests performed by Sanchez and Popish.   The pressure loss was assumed at first to be caused by leaks in the propellant system and thruster assembly.   As a result, both were disassembled and reassembled multiple times, with careful attention paid towards proper sealing.   The thruster especially was subject to several sealing techniques: a high pressure gasket sealant was used to seal internal thruster parts, while putty was used as an additional external sealant.   However, post-test thruster examinations consistently showed that both sealants were being ejected from the thruster at certain joints, specifically along the seam between the thruster and manifold and around the bolts holding the nozzle inserts into the thruster.   New 1/32-inch

high pressure carbon gasket material was added in order to provide a better seal at these locations; the gasket material reduced pressure leakage considerably.

Even with better sealing between the thruster and manifold, however, chamber pressures never even reached 1000 psi, roughly the minimum pressure necessary to achieve Fabri choking. As a sanity check, Test 42 was performed using the original conical nozzle inserts used by Sanchez and Popish. This test yielded higher chamber pressures, which pointed towards the new nozzle inserts as the reason for the pressure differences. The new inserts still seemed unlikely, however, as they were designed to the same tolerances as the originals and with the same throat area. However, it was eventually discovered that the inserts used by Sanchez and Popish had been modified from their original design to incorporate a considerably smaller throat area.

Minimizing throat area proved to be the key to achieving higher chamber pressures. While not intuitively obvious, the primary chamber pressure will actually decrease in order to accommodate a larger throat. Equation 5-1 for isentropic choked mass flow highlights this relationship:

$$\dot{m}_P = \frac{P_0 A_P^*}{a_0} \gamma \left(\frac{2}{\gamma+1}\right)^{\frac{\gamma+1}{2(\gamma-1)}} \tag{5-1}$$

Primary nozzle throat area was confirmed as the cause of the chamber pressure issues by comparing mass flow rates between tests using both the original nozzles and the new inserts. Each test achieved nearly the same maximum primary mass flow rate, independent of throat area, which indicated that the throat was simply too large on the first set of new inserts to achieve the desired chamber pressures. As a result, the first three sets of nozzles, designed with an area ratio of approximately 10, were omitted from further tests and instead focus was placed on the second set of nozzles, which all had

design area ratios near 20 and thus throat areas equal to half of the first set. This throat area reduction proved to be the solution to the chamber pressure issues, which did not occur again once the switch was made to the smaller throat nozzles. Figure V-2 compares tank and chamber pressures between Nozzles A3 and B3, which are identical save for throat area.
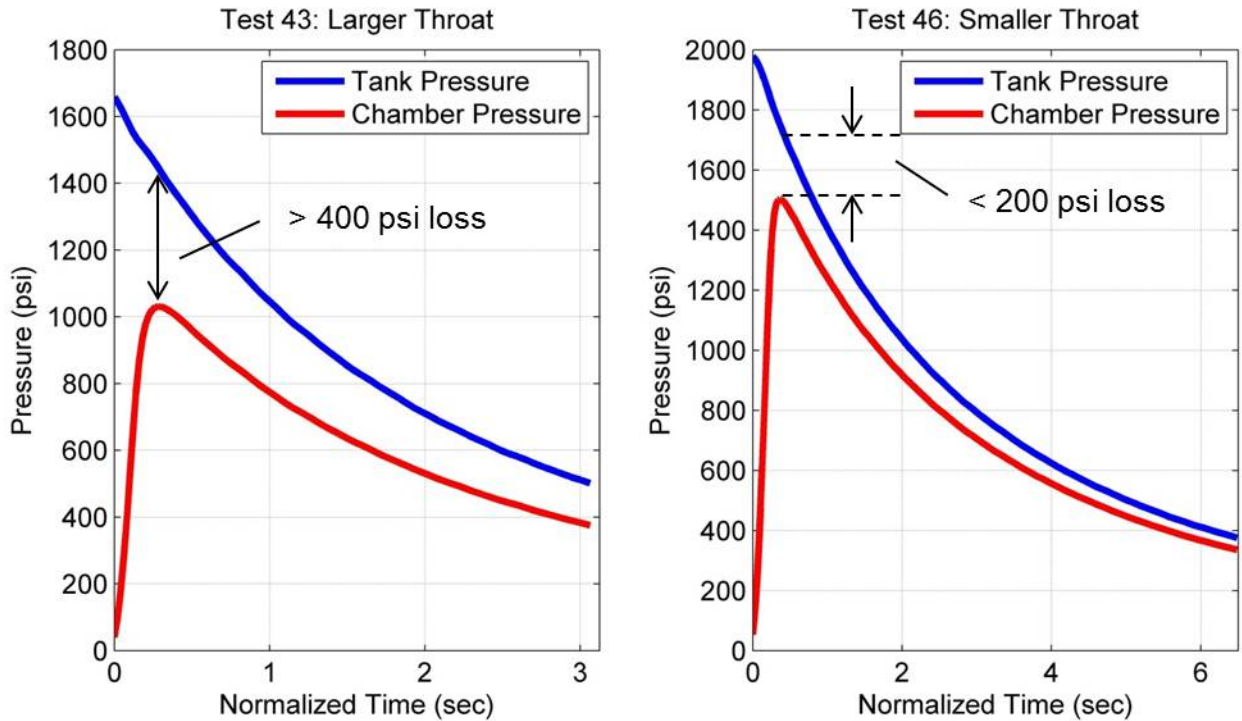
Figure V-2. Pressures resulting from larger and smaller throat areas.

VI.   Formal Testing

After all issues with the experimental apparatus had been resolved during preliminary tests, formal testing was initiated. A total of 26 formal test runs were conducted using 4 different nozzles in 2 distinct thruster configurations: 14 tests using an aluminum plate as the bottom of the mixing duct, with pressure ports for recording primary plume data, and 12 tests using fiberglass plates as the upper and lower surfaces of the mixing duct, for shadowgraph flow visualization. Each test was run using 3 high pressure nitrogen cylinders, providing chamber pressures as high as 1712 psi and maximum primary mass flow rates as high as 1.67 lb_m/s. Plenum pressures were reduced to as low as 6.8 psi, yielding maximum pressure ratios as high as 160. Average primary Mach numbers for each nozzle were between 4.34 and 4.57, as compared to the average Mach number of 4.32 for the original conical nozzles. All pressures reported are absolute.

A.   Experimental Procedure

A pressure-fed simulated air augmented rocket was tested at varying Stagnation Pressure Ratios. The tests were initiated at a high primary supply pressure that steadily decreased during the run. Secondary stagnation pressures were continuously reduced via a plenum connected to the rocket's secondary ducting. Tests were conducted at the Aerospace Engineering Department's Propulsion System Test Facility, a concrete enclosure with an approximately 10 ft x 20 ft test cell and adjacent 10 ft x 5 ft control room. The control room is isolated from the test cell by 10 inches of reinforced concrete and a 4-inch-thick tempered glass window port. A minimum of two operators were present at each test to ensure safe operation of the apparatus.

Each test used three high pressure nitrogen cylinders in varying degrees of fullness: one full cylinder at 2600 psi, one cylinder at approximately 2100 psi, and one cylinder at approximately 1750 psi. All three cylinders were connected to a buffer tank with a modified throat to allow for greater mass flow rates than a standard tank. The buffer tank was controlled with the Flow Control System's ball valve mechanism, which defaults in the "closed" position. Each cylinder was opened and closed in succession in order to fill the buffer tank, starting with the emptiest and moving to the fullest. Once the buffer tank was full and the test cell had been cleared, the LabView data logger and shadowgraph camera were activated from the control room and the flow control unit was triggered, releasing the propellant nitrogen and initiating the test. After each test, the emptiest tank was rotated out and replaced with a new, full tank at 2600 psi.

Once the flow control unit is triggered, the compressed nitrogen flows through the propellant feed system, into the rocket chamber, through the primary nozzle, into the mixing duct, and finally ejects out into ambient air. Upon entering the mixing chamber, the primary flow creates a shear force to pull air in through the secondary ducts from the fixed reservoir of air in the plenum. Tests typically last 3 to 10 seconds; during the first 1.5 seconds the primary rocket chamber ramps up from ambient pressure to a maximum value and then decreases at a diminishing rate until returning to ambient. As pressure builds in the chamber the primary plume rapidly accelerates into an underexpanded condition, establishing a (usually) steady shock structure. Eventually the flow passes through optimal expansion and into an overexpanded case, before the chamber pressure falls below levels necessary to achieve supersonic flow and the plume decelerates to subsonic for the remainder of the test.

B. Shadowgraph Images

Prior to each test the shadowgraph system was cleaned and its mirrors and light source were recalibrated to project the sharpest possible image onto its viewing surface. The device used to record the shadowgraph data, a Phantom v310 high speed camera, was then set up in the test cell and its lens focused onto the shadowgraph system's viewing surface. At the start of each test the camera was triggered by an operator simultaneously with the data recording system, and continued recording data until its hard drive was full. Once the test was complete, any extraneous pre- or post-test data was cut and only relevant footage was saved. Figure VI-1 illustrates the boundaries of the shadowgraph's field of view within the mixing duct.
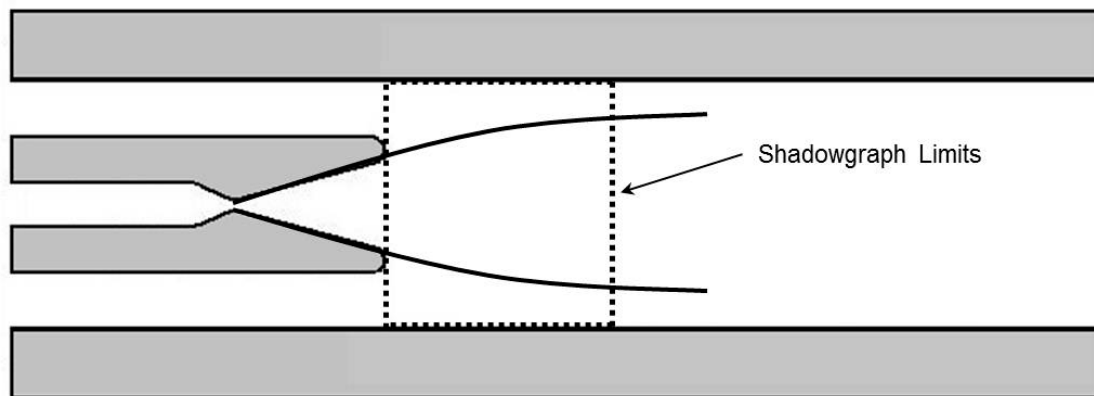
Figure VI-1. Location of the shadowgraph image within the mixing duct.

Maximizing the quality of the camera's images meant compromising between image brightness and image clarity when setting its exposure time. Thus, depending on the light conditions present during each test, the exposure time was set between 300 and 1000 microseconds. At exposure times below these levels, the camera could not gather enough light from the system's viewing surface (alternatively, the system's xenon light source could not produce a bright enough light) to produce a properly visible image.

As mentioned previously, the camera used to record the shadowgraph images of the flow is capable of recording up to 500,000 frames per second. This rate is much higher than necessary for visualizing the flow in the current setup. For example, in a worst case scenario when the primary flow is moving at Mach 4.57, the fastest recorded exit Mach number, the camera would have to record at a rate of roughly 12,350 frames per second in order to capture a single particle across multiple frames. This rate might be necessary if the goal was to capture small-scale turbulent structures within the shear layer between the two streams. However, because the present work focused more on a general qualitative analysis of the mixing duct flow field than a comprehensively quantitative one, a rate of 300 frames per second was selected because it would still allow the camera to capture the desired flow field changes on a small time scale without creating unnecessarily large file sizes.

C. Data Reduction

Formal test data was recorded on 23 parallel channels at a rate of 50 Hz, which was seen as a good compromise between file size and data resolution given the capabilities of the computer used in the experiment. Data recorded by LabView during testing was saved to a Microsoft Excel® spreadsheet at the conclusion of each test. Once saved, the data from the spreadsheet was imported into MATLAB for post-processing. During post-processing, MATLAB's smoothing function was used to reduce noise in the recorded data, while a script was written to cut data captured outside the window of useful information. Post-processing was used to interpolate between data points, but no data extrapolation was performed.

Recorded temperature and pressure values were normalized based on current ambient conditions as part of the data reduction process. This was done by subtracting the first value recorded by each transducer or thermocouple from the rest of the data recorded by that device, and then adding the current ambient pressure or temperature to that value. Several experimental parameters that were not directly measured during testing were instead calculated from other measured quantities. The experimental parameters obtained indirectly are derived below. Each calculation assumes that the flow behaves as a perfect gas, which is reasonable for the temperatures and pressures present in the primary and secondary streams[9].

The Mach numbers of both the primary and secondary flows were calculated using recorded static and stagnation pressures in the primary and secondary, respectively, using the isentropic Mach number equation for compressible flow in a perfect gas. The primary flow Mach number is calculated at the nozzle exit plane. Equation 7-1 shows the isentropic Mach number equation.

$$M = \sqrt{\frac{2\left[\left(\frac{P_0}{P}\right)^{\left(\frac{\gamma-1}{\gamma}\right)}-1\right]}{\gamma-1}} \qquad (7\text{-}1)$$

Flow density values were required for both mass flow rate calculations. Equation 7-2 shows the perfect gas equation of state used to calculate density in the primary and secondary flows based on recorded static and stagnation pressures and temperatures.

$$\rho = \frac{P}{RT} \qquad (7\text{-}2)$$

Flow velocity values were also used in mass flow rate calculations. Equation 7-3 uses recorded values for static and stagnation temperature to calculate the speed of sound in

the primary and secondary flows, and this value is combined with the calculated Mach number to find the velocity in Equation 7-4.

$$a = \sqrt{\gamma R T} \qquad (7\text{-}3)$$

$$V = Ma \qquad (7\text{-}4)$$

The mass flow rate through the left secondary duct was calculated from both recorded and calculated values, using the isentropic mass flow rate equation for compressible flow in a perfect gas. Equation 7-5 shows a variant of the isentropic equation for secondary mass flow rate.

$$\dot{m}_s = \frac{32.2 A_s P_{0s} M_s \gamma \left[1 + \left(M_s{}^2\right)\frac{\gamma-1}{2}\right]^{\frac{-(\gamma+1)}{2(\gamma-1)}}}{a_s} \qquad (7\text{-}5)$$

The mass flow rate through the primary nozzle was also calculated using both recorded and calculated values, based on another variant of the isentropic mass flow rate equation. Equation 7-3 shows the isentropic equation used to calculate primary mass flow rate.

$$\dot{m}_p = \frac{32.2 \gamma \left(\frac{\gamma+1}{2}\right)^{\frac{-(\gamma+1)}{2(\gamma-1)}} A_p^* P_{0p}}{a_{0p}} \qquad (7\text{-}3)$$

Flow values were also calculated using Bernoulli's equation with compressible flow corrections, in order to see the effects of different solution methods on the final results. According to Popish[2726], the average difference between calculated values for velocity ratio and secondary Mach number for each method is on the order of 7%. This difference was deemed acceptable, and only the isentropic calculations are presented in this paper.

D.   Experimental Error Analysis

Each measurement recorded as part of the experimental process has a finite accuracy associated with it, which creates uncertainty in the values reported after testing. The uncertainty of these values in turn propagates through any calculations made using this data. As a result, an error analysis was performed in order to understand the inaccuracies associated with these calculations and quantify them.

The first step in quantifying the error is to determine the accuracy of the measuring devices used in the test. For the Omega pressure transducers the maximum uncertainty due to errors in linearity, hysteresis, and repeatability was quoted at 0.25% of the full scale reading[28]. The Omega thermocouples used in the test were reported to have less than 4% instantaneous drift[29]. Baseline calibrations for the thermocouples were performed using an ice bath-calibrated mercury thermometer. The pressure transducers were calibrated using a steady-state high pressure air supply and a certified-calibrated precision-accurate 50 psi pressure gauge.

Each measurement of a physical length or area also has an error associated with it. Because several experimental results depend on these values, each physical dimension was specified as part of the design process and manufactured to within a certain tolerance. To supplement these tolerances the dimensions were measured again prior to testing, using calipers that have an associated least scale reading (LSR). Any values calculated using these measurements made use of either the design dimensions with fabrication tolerance, or the measured dimension with LSR, whichever was the more precise. The tolerance or LSR associated with the chosen measurement was used as the uncertainty of the quantity for error analysis.

As noted by Popish[27], there are additional sources of error associated with calculations made using shadowgraph images. These originate with data collected by the video camera. Specifically, there is an error associated with correlating frames from the video with the recorded pressure and temperature data. The camera used for testing was set to record at 300 Hz (300 frames per second). The pressure transducer and thermocouple data was collected at 50 Hz. In order to correlate the pictures with the pressure and temperature data the start time of the test had to be found and matched. The error associated with this correlation was calculated by determining the maximum interval of time that the picture might be representing. Frames from one test were correlated 20 times with the first significant pressure rise (signaling the start of the test), yielding a standard deviation of 1.31 frames. Each recorded time step (0.2 seconds) corresponds to 6 frames; thus 1.31 frames correlate to just 0.044 seconds. In this case the standard deviation was rounded up such that the picture might correspond to at most a total of one time step's difference from the correlated time. The change in value of each variable was found over this time and its corresponding error was calculated.

In order to quantify the net effects of combined error on the final experimental results, an error propagation analysis was performed. The calculated experimental uncertainty associated with each measured quantity was used to produce a value of propagated uncertainty in the final experimental results. This was done using a Pythagorean sum. Equation 7-5 shows the formula used for this calculation.

$$\Delta Z = \sqrt{\left(\frac{\partial F}{\partial A}\right)^2 (\Delta A)^2 + \left(\frac{\partial F}{\partial B}\right)^2 (\Delta B)^2} \qquad (7\text{-}5)$$

The total calculated uncertainty associated with each experimental uncertainty is summarized in Table VI-1. Values are presented as percentage uncertainty.

Table VI-1. Experimental uncertainties.

	Quantity	Symbol	Average	Standard Deviation
Primary	Density	ρ_p	0.06%	0.05%
	Velocity	V_p	2.03%	0.23%
	Mach Number	M_p	1.18%	0.02%
	Mass Flow Rate	$\dot{m}_p$	0.31%	0.28%
Secondar	Density	ρ_s	1.76%	0.07%
	Velocity	V_s	0.2%	0.07%
	Mach Number	M_s	0.35%	0.14%
	Mass Flow Rate	$\dot{m}_s$	2.95%	0.18%
	Entrainment Ratio	φ	2.96%	0.18%

E.   Test Repeatability

During the testing process, a minimum of 6 tests were performed using each nozzle: 3 centerline pressure tests and 3 shadowgraph tests, in order to verify the repeatability of each nozzle's performance. Each time that a modification was made to the thruster, including the replacement of nozzle insert plates and the addition of new high pressure gasket material to seal the manifold-thruster connection, at least one test using each nozzle insert was conducted in order to verify that the modifications did not affect the thruster's performance. Care was also taken to test all nozzles under similar conditions. While nozzles were tested at chamber pressures between 1437 and 1712 psi, each nozzle achieved a chamber pressure of 1500 or higher at least once. Primary exit Mach numbers ranged between 4.34 and 4.57 for the different nozzles across all tests, a variation of approximately 5%. Most of this variation can be attributed to differences between design area ratios, which were 20 for all of the nozzles, and actual measured area ratios, which varied between 19 and 20.

Testing showed that the nozzles produced very repeatable results. Figure VI-2 shows performance results from three tests per nozzle. The data is shown with error bars representing the 2.7% error associated with the calculated entrainment ratio values. As shown in the figure, each nozzle follows a nearly identical performance trend in terms of entrainment ratio versus pressure ratio, especially as pressure ratio increases beyond 80-100, near the optimally expanded condition for all of the nozzles.

However, the figure does show a slight variation in the maximum pressure ratio achieved by each nozzle for different tests. While tests were performed under nearly identical conditions, primary chamber pressures did vary by as much as 250 psi. Secondary pressures were also prone to some fluctuation across tests, depending on primary chamber pressure. Thus, the variations in maximum pressure ratio are most likely due simply to slight differences in initial conditions.
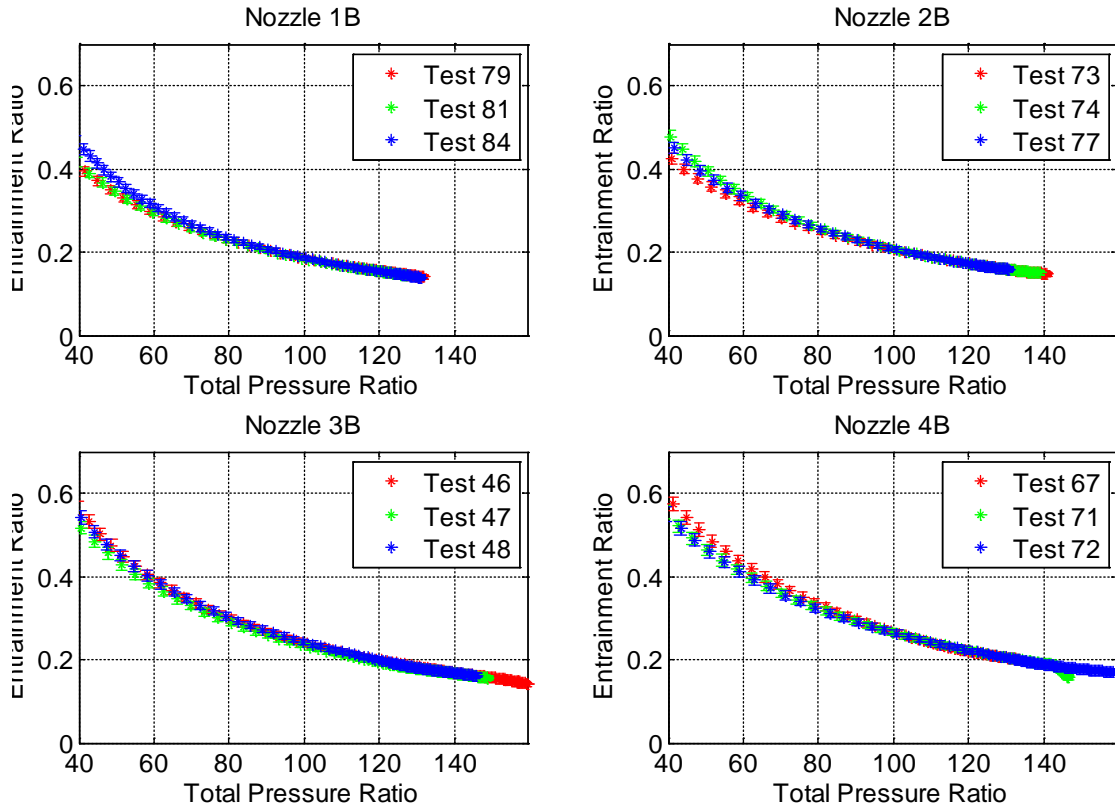
Figure VI-2. Performance results showing repeatability for each nozzle.

Shadowgraph images of the flow revealed similar repeatability results across tests. Figure VI-3 shows shadowgraph images from two separate tests for each nozzle, all at pressure ratios of 120. The pictures reveal that the primary plume remains nearly identical for each pair of tests, while also showing the considerably different internal structures produced by each nozzle. Maximum expansion appears at the same location downstream for each pair of tests. Shocks in the plume follow patterns unique to each nozzle, and the plume boundaries appear to be identically underexpanded. Thus, the lack of discernible differences in the physical appearance of the flow for different tests using the same nozzles suggests an excellent level of repeatability for each nozzle.

Tests 82 and 83, Nozzle B1.
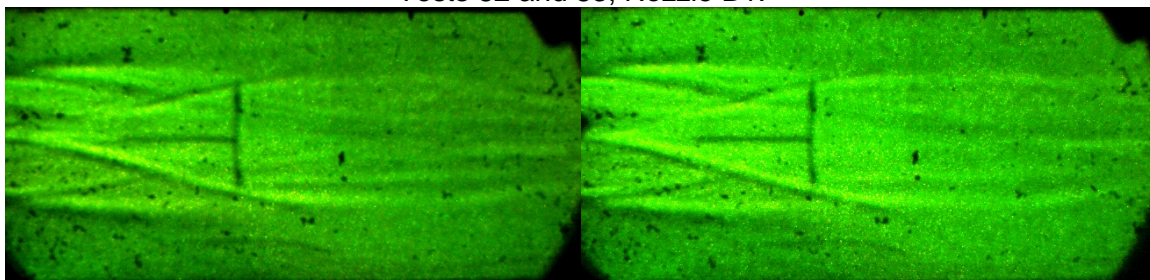
Tests 76 and 77, Nozzle B2.
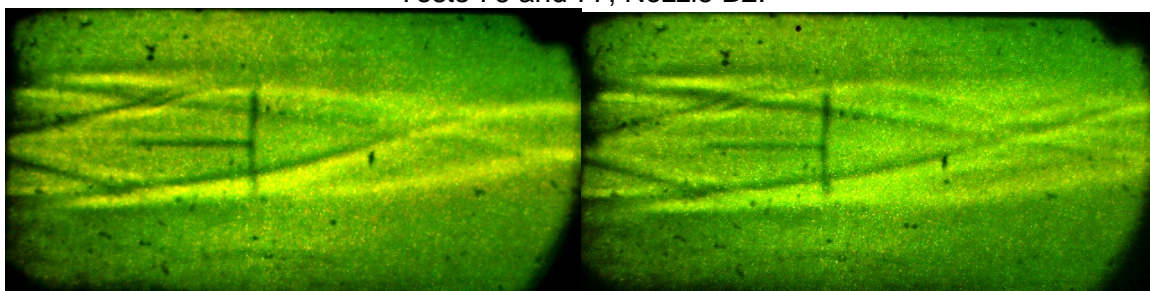
Tests 68 and 69, Nozzle B3.
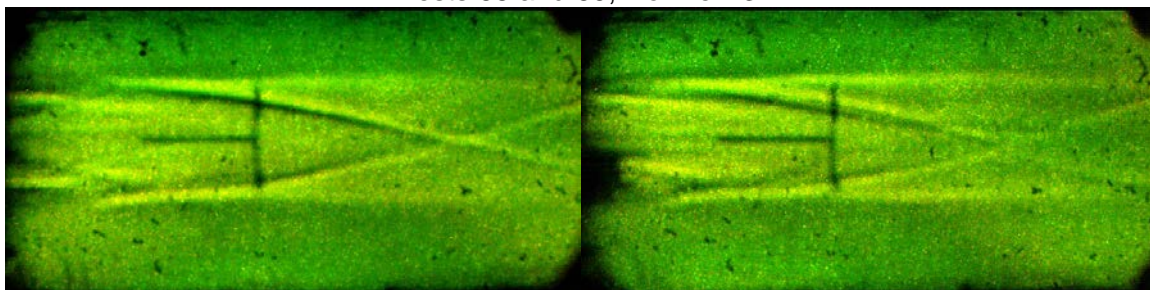
Tests 66 and 67, Nozzle B4.
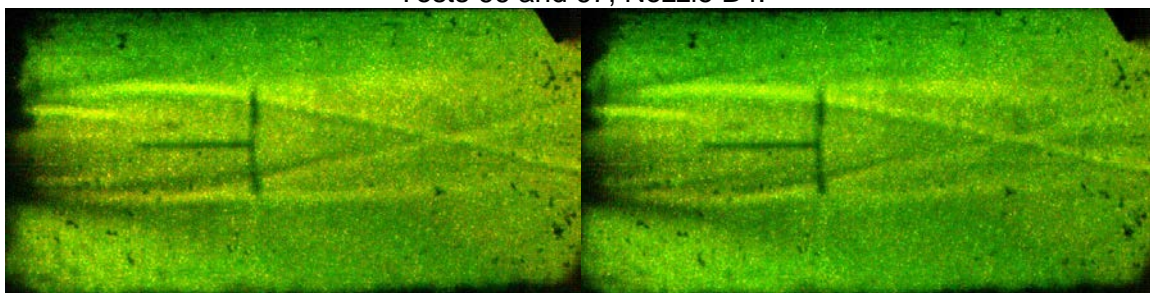
Figure VI-3. Shadowgraph images showing test repeatability, PR = 120.

VII.   Shadowgraph Results

Shadowgraph images taken during testing were used to characterize the flow in the AAR mixing duct.   Flow characterization included both quantitative and qualitative observations. Several additional observations were made of unique and unexpected flow-field phenomena, and attempts were made to characterize these based on other scientific literature.

A.   Symmetry and Unsteadiness

Although the measured differences in size between left- and right-side components of the AAR were negligible, and great care was taken during each reassembly of the apparatus to maintain this symmetry, testing showed that the right and left secondary flows were not precisely symmetric. Shadowgraph images also revealed some amount of asymmetry and unsteadiness in primary plume structures, both in terms of the size and number of shock cells in the plume and the symmetry of the plume with respect to the nozzle centerline. Most tests demonstrated a consistent plume structure in Nozzles B1, B3, and B4, as well as C3, the original conical design. In fact, these nozzles produced internal expansion and compression wave reflection angles that typically varied by only a few degrees, and at predictable, periodic, microsecond-level frequencies. However, Tests 76-78 highlighted that Nozzle B2 in particular produced a plume that was both periodically asymmetric and time-varying in terms of the shape of its plume boundary and the number of shock cells visible in its core. Figure VII-1and Figure VII-2 illustrate the non-ideal structure of Nozzle B2's plume.
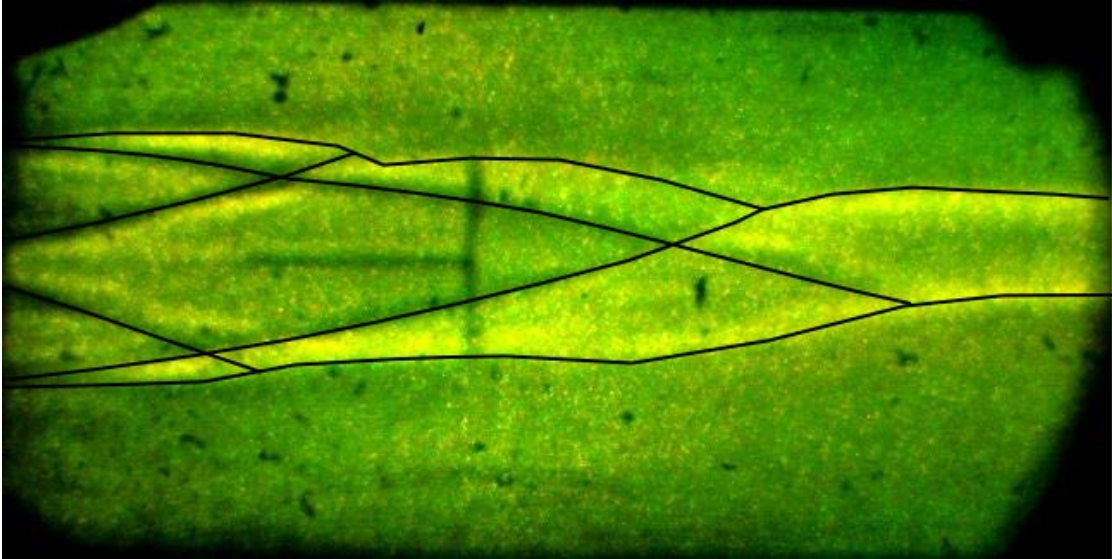
Figure VII-1. Nozzle B2, Time = 1.272 seconds.
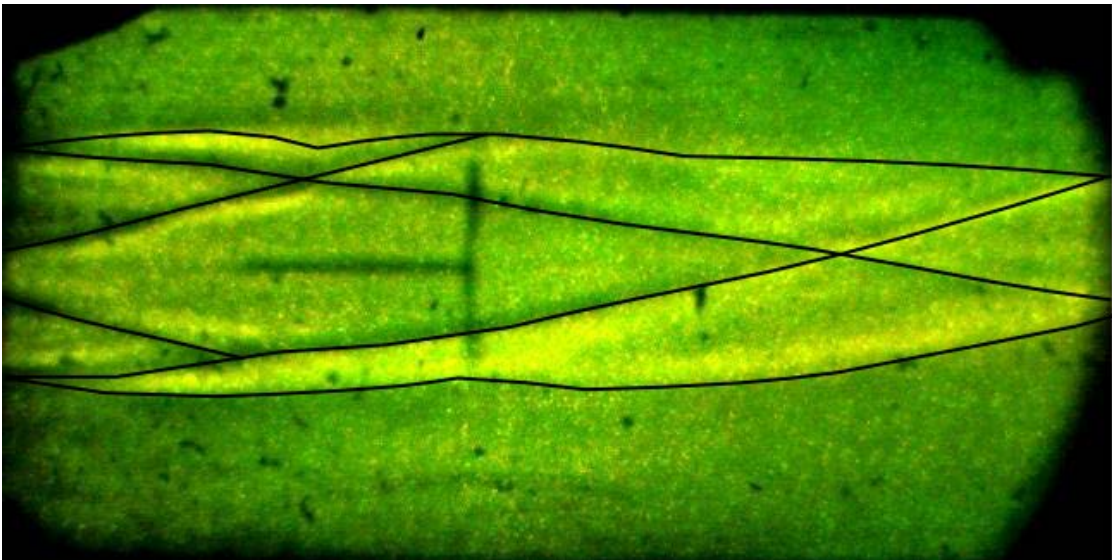
Figure VII-2. Nozzle B2, Time = 1.282 Seconds.

As the figures show, the structure of the primary plume changes considerably over very short intervals – in this case the plume contracts and expands, changing the structure of the expansion cycle, over the course of 10 milliseconds. In Figure VII-1, it's also apparent that the plume becomes less symmetric as it moves downstream of the nozzle exit – within three inches of the nozzle exit the plume begins to contract on the right side but

not on the left, and at four inches downstream the entire plume shifts to the right, causing the internal shock diamond to collapse. By Figure VII-2, 10 milliseconds later, the plume has returned to a more symmetric condition.

While visual data suggested that only Nozzle B2 produced a significantly unsteady or asymmetric primary plume, pressure data from the secondary ducts and mixing duct wall revealed that none of the nozzles produced results that were perfectly symmetric in the secondary or mixing duct. Figure VII-3 shows secondary duct pressure measurements from four different tests, one for each nozzle.
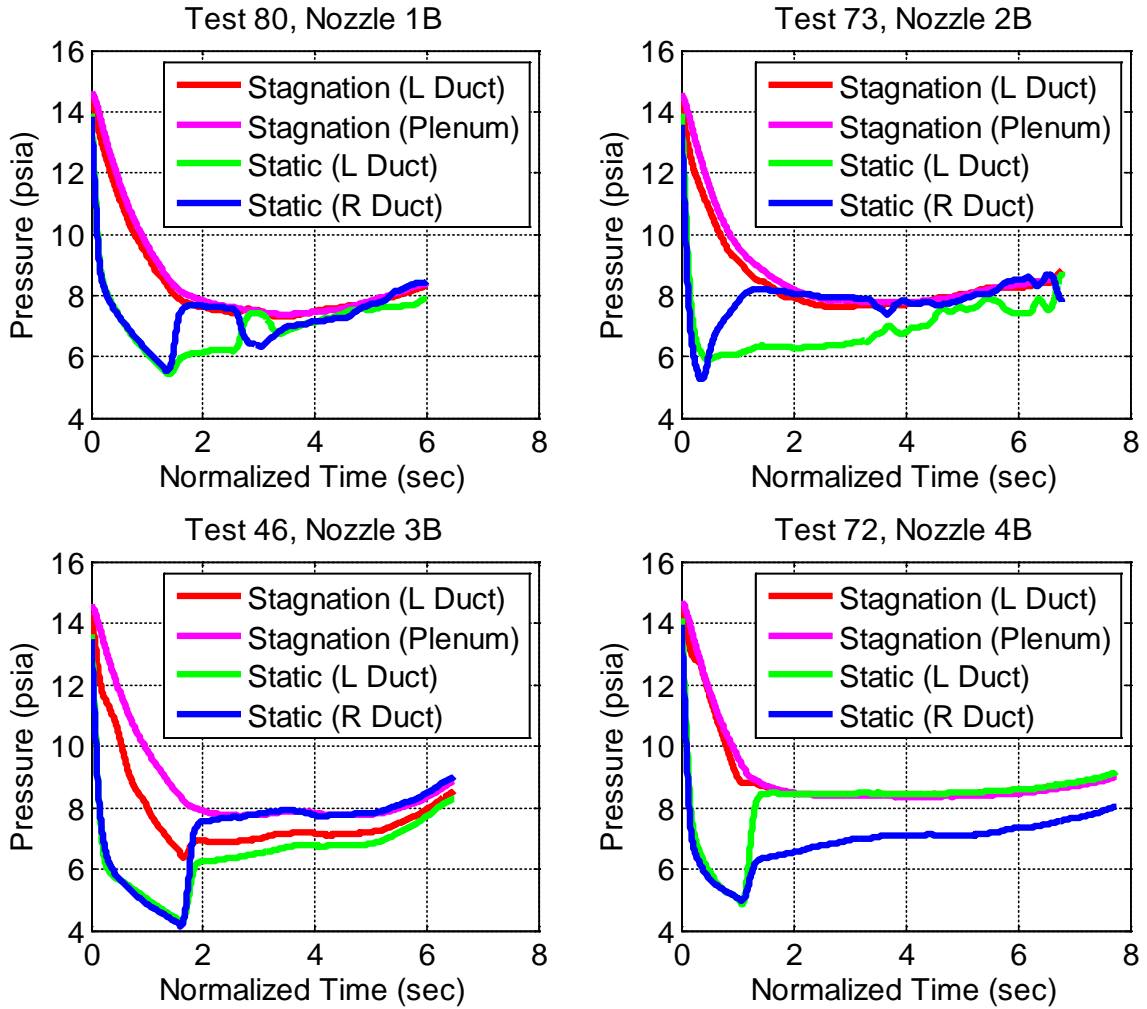
Figure VII-3. Secondary duct pressures showing flow asymmetry.

84

While the measurements show very close correlation between stagnation pressures, indicating that the left duct is a good approximation for the pressure in the plenum, the static pressures in each duct vary considerably across all tests. Generally speaking, the static pressures remain equal on both sides at test startup, as the primary chamber pressure rapidly increases and the secondary drops in response. However, once the stagnation pressure ratio reaches a maximum, there is a sharp rise in the static pressures in the secondary. As the static pressures in the secondary ducts increase, at some point they begin to diverge from one another.

At a fundamental level, the primary flow is causing both the right and left secondary flows to choke downstream in the mixing duct, a result of the aerodynamic throat formed by the primary plume. Once the stagnation pressure ratio reaches its maximum and begins to decrease, the primary plume begins to shrink, increasing the area of the aerodynamic throat and causing the secondary flow to unchoke. As a result, the secondary flow rapidly decelerates to accommodate the expanding aerodynamic throat, which coincides with an increase in static pressure.

At this point in the test, the flow may choke again in either secondary stream; the static pressure spikes and drops seen in Tests 73 and 80 indicate that one side of the flow has choked again, briefly, with a simultaneous increase in pressure on the other side. This is the primary cause of asymmetry in the secondary, and it shows that the unsteadiness and asymmetry are linked. Unsteadiness in the primary plume after it has achieved its maximum pressure ratio causes one secondary stream or the other to re-choke intermittently, which in turn produces the asymmetric fluctuations in the secondary pressures. There does not appear to be a cause-and-effect relationship between the

choking of one stream and coinciding pressure rise in the other stream – they appear to occur at exactly the same time, to within a few milliseconds. This implies that the relationship is not due to wave propagation from one side's re-choke to the other side within the mixing duct, but more likely because of the plume's fluctuations once it becomes overexpanded. Upstream effects may also cause re-choking. Figure VII-4 shows mixing duct wall pressures that indicate flow asymmetry in line with the secondary duct pressures.
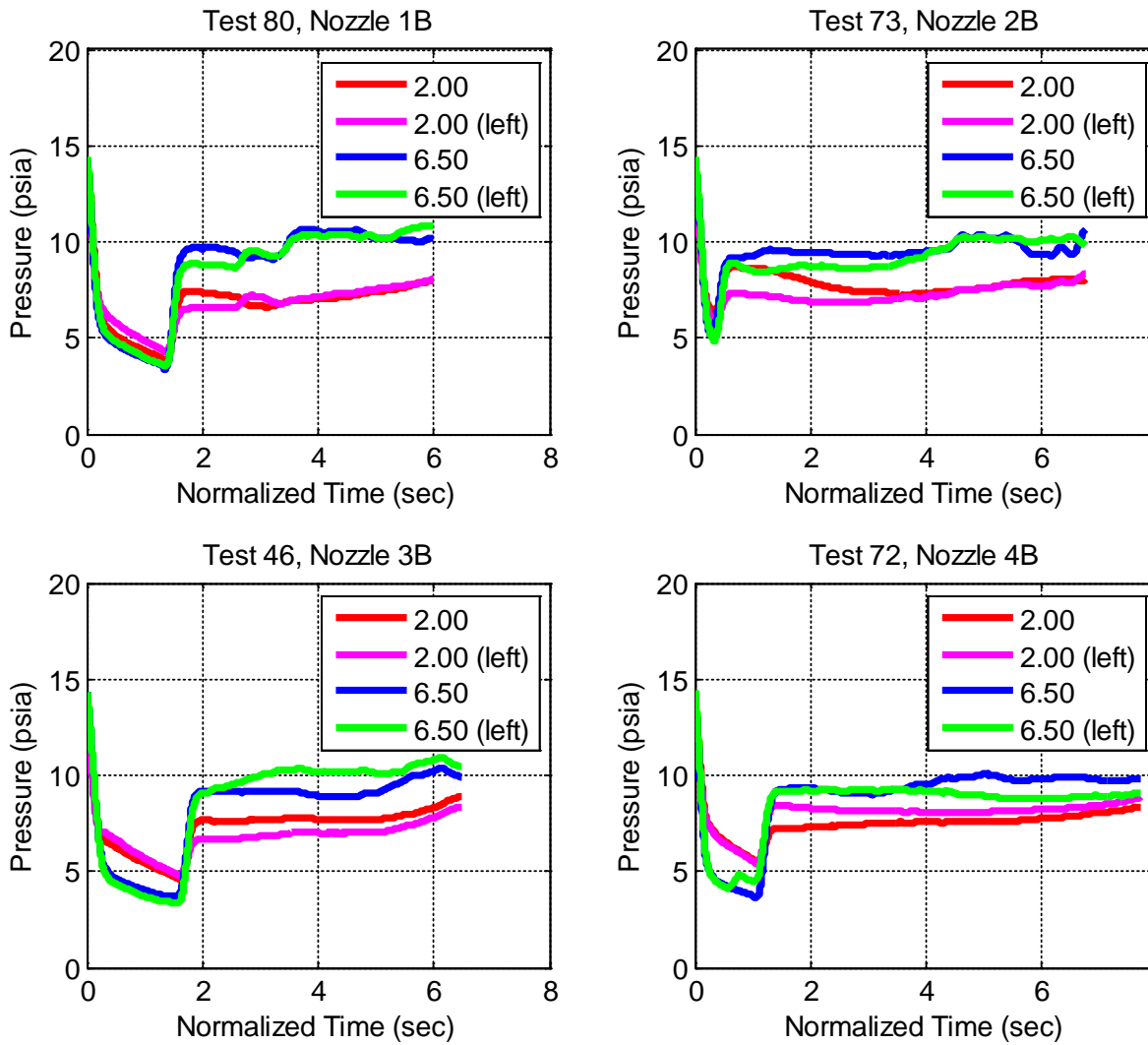
Figure VII-4. Mixing duct wall pressures showing flow asymmetry.

As with the secondary duct pressures, mixing duct wall pressures indicate a large pressure drop coinciding with the Fabri-choke condition, a pressure rise as the flow unchokes, and then static pressure fluctuations as the flow re-chokes on either side. Also worth noting is the left wall pressure at 6.5 inches downstream of the nozzle in Test 72, which has a brief spike before dropping again and then increasing with the rest of the wall pressures. This pressure spike indicates that the aerodynamic throat may have briefly moved upstream of the pressure port, causing a pressure spike due to the increased pressure behind the standing shock at the aerodynamic throat. The lack of a coinciding pressure spike on the right duct wall indicates that the point of maximum primary plume expansion (and thus the aerodynamic throat) is further downstream, beyond the last wall pressure port. If that is the case, then the plume may not always be symmetric, in contrast with the shadowgraph data presented previously.

B.   Primary Nozzle Shock Structure

Shadowgraph images from each test revealed characteristics about the plume produced by each nozzle. While the bell-mouth nozzles were expected to produce slightly different plume shapes from the original conical nozzle inserts, the shock structure within each bell-mouth plume was expected to be relatively similar. However, the images showed that each nozzle produced a unique shock structure within the primary plume, whether in an underexpanded, overexpanded, or optimally expanded condition. Figure VII-5 through Figure VII-9 illustrate the shock structures for an underexpanded case of each nozzle, including the conical nozzle used by Sanchez and Popish. The nozzles are labeled based on their respective lip thickness, numbered in order of increasing thickness. Table VII-1 summarizes the naming convention used to label the nozzles. B indicates a bell-mouth

contour, while C indicates the original conical design used by Sanchez and Popish. Also note that throat area and lip thickness are inversely related; a smaller lip means a larger throat, in order to maintain the same area ratio and thus exit Mach number.

Table VII-1. Nozzle naming convention.

Name	Lip Thickness (in)
B1	0.1250
B2	0.1875
B3	0.2500
B4	0.3125
C3	0.2504
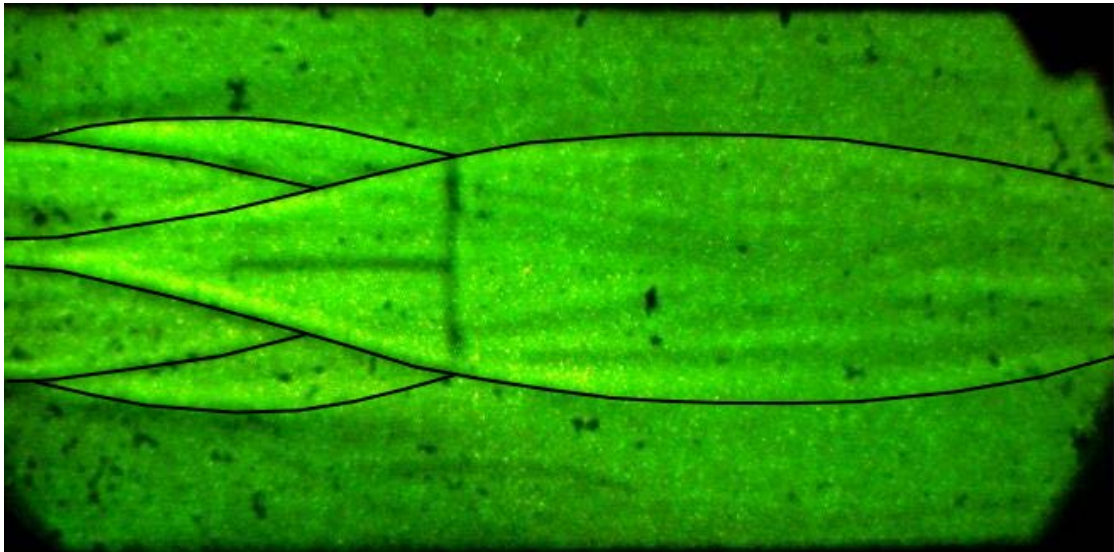
Figure VII-5. Nozzle B1, Test 84, PR = 125: Underexpanded Case.
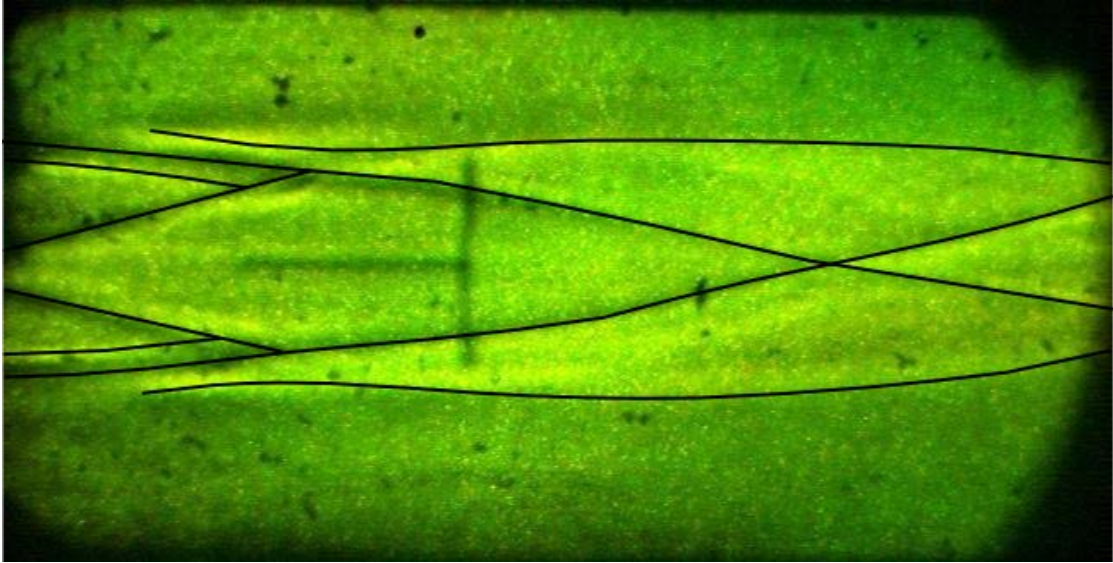
Figure VII-6. Nozzle B2, Test 76, PR = 125: Underexpanded Case.
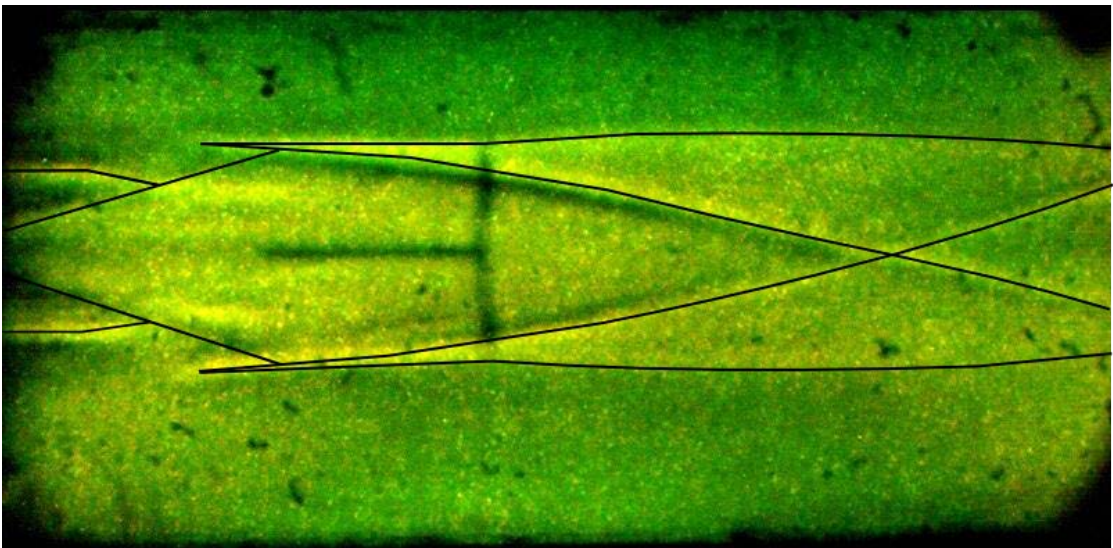
Figure VII-7. Nozzle B3, Test 68, PR = 125: Underexpanded Case.
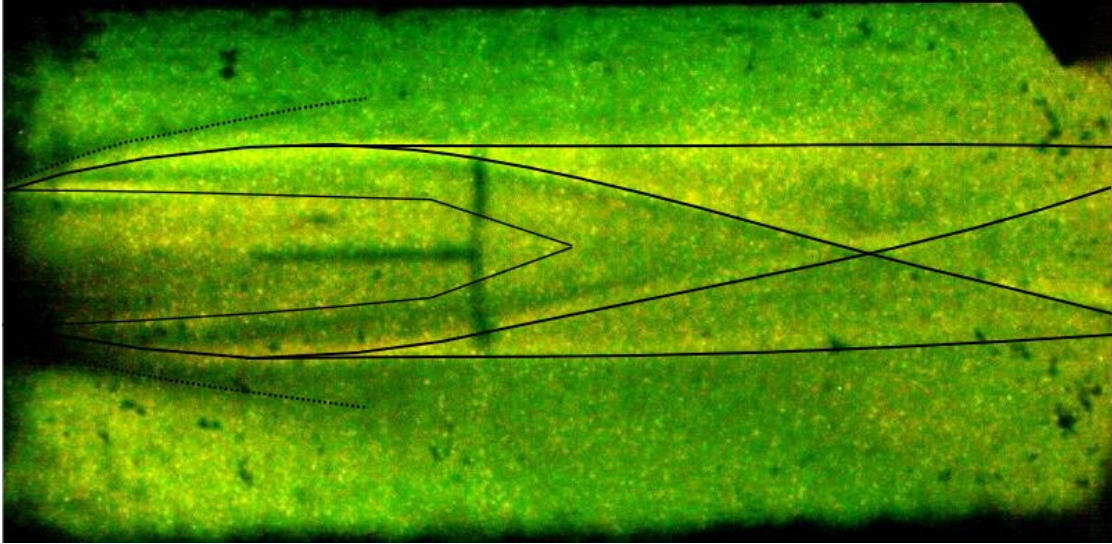
Figure VII-8. Nozzle B4, Test 65, PR = 125: Underexpanded Case.
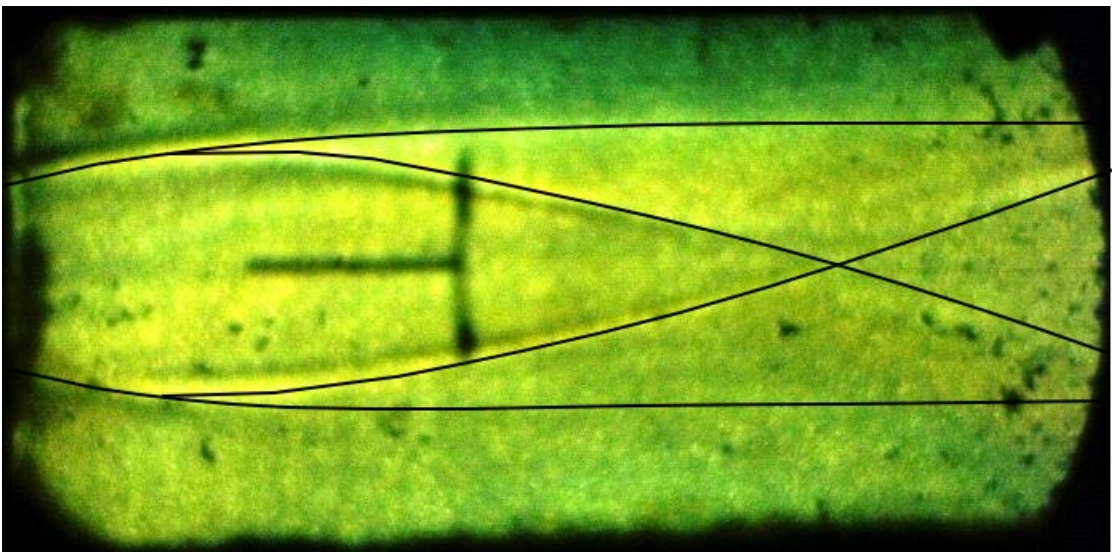
Figure VII-9. Nozzle C3, Test 54, PR = 125: Underexpanded Case.

The characteristic immediately worth noting is the presence of shock waves in the center of the primary core at the nozzle exit plane. Each bell-mouth nozzle exhibits these shocks to some extent, but the conical nozzle does not. Basic gas dynamics dictate that in the underexpanded case, exhaust gases within the nozzle expand via a cycle of Prandtl-Meyer expansion and compression waves until they reach ambient pressure. The underexpanded cycle begins with the formation of Prandtl-Meyer expansion waves at the

nozzle lip which reflect towards the nozzle centerline. Typically, these waves are the first to occur in the plume. However, each bell-mouth nozzle examined in this study seems to produce a second set of shock waves anchored somewhere within the nozzle and interacting with the shocks shed from the nozzle lip, generating a double-diamond pattern in the ensuing plume. In contrast, the original conical design tested by Sanchez and Popish seems to lack this second set of shocks and follows the more common single-diamond plume shock structure.

Secondary shock structures originating within the nozzle have been observed before[36]. In that study, Munday observed that the shocks originate at the throat, emerging from the nozzle and passing through the lip shock or Prandtl-Meyer fan and reflecting off the shear layer to create a second set of shock cells within the plume. This second set of cells becomes superimposed on the cells from the lip, generating a double-diamond appearance. As the two shock trains propagate downstream they eventually coalesce into a single set of shock cells. The ultimate conclusion is that the size of the Mach disk(s) within the nozzle, and thus the angle of the oblique shock leaving the nozzle, is determined primarily by the nozzle's design Mach number. In that case, a higher design Mach number yields a smaller oblique shock angle at the exit.

The results found in that study support the conclusion that the lines visible at the center of the plume at the nozzle exit are shock waves originating inside the nozzle, and forming as a result of non-ideal nozzle performance. As mentioned previously, none of the nozzles used in this study has a perfect bell-mouth contour due to the limitations in machining such a curve on a mill, and so due to those imperfections some amount of non-ideal performance is expected.

Figure VII-10 shows what a non-ideal shock structure inside the nozzle could potentially look like, based on similar results by Hadjadj for shock formation inside a rocket nozzle under transient startup conditions[37].
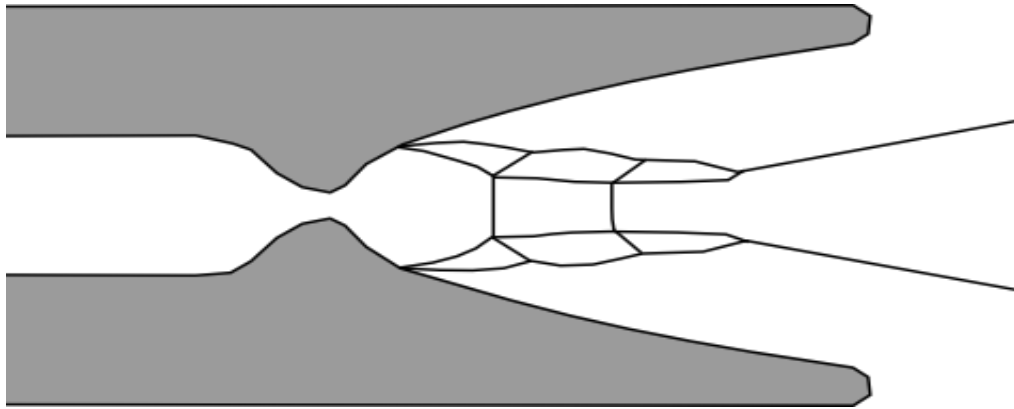
Figure VII-10. Possible shock structure in nozzle's expansion region.

Unlike Munday, the four bell-mouth nozzles in the current investigation were designed with the same area ratio and thus the same exit Mach number, meaning that design Mach number alone cannot be responsible for the differences in oblique shock angle at the nozzle exit plane. Furthermore, there appears to be an inverse relationship between nozzle throat area and the oblique shock angle. Nozzle B4, with the smallest throat area, produces the largest divergence angle; while Nozzle B1, with the largest throat area, produces the smallest divergence angle. One possible explanation is that the size of the throat, not the actual speed of the flow, dictates where the shocks may form and thus if/where they may reflect off of the nozzle walls before exiting the nozzle.

As discussed previously with regards to nozzle design, an ideal bell-mouth nozzle will cause the expansion and compression waves that form in its expanding section to cancel each other out. However, in the non-ideal case this does not occur and strong oblique shocks may form in this region. The present results seem to agree with this conclusion.

Such non-ideal performance may also explain why the shocks are not visible in the conical nozzle shadowgraphs – the constant 15.35° half angle nozzle does not cause the flow to change direction rapidly enough to allow strong shocks to form, and so the nozzle performs as expected for the underexpanded case.

C.   Secondary Flow Choking

In addition to the unique shock structures present in each nozzle's primary plume, shock waves were also observed in the subsonic secondary flow.   Figure VII-11 shows a shadowgraph image taken during the beginning of Test 82 using Nozzle B1.
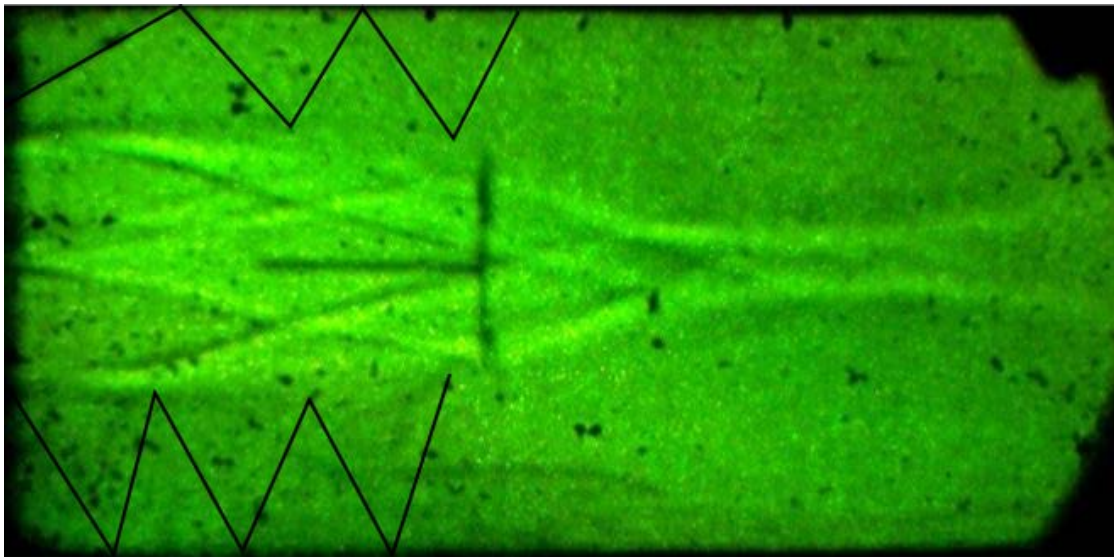
Figure VII-11. Nozzle B1, Test 82, PR = 4. Shocks in secondary flow at test startup.

Immediately obvious is a complex yet regular wave system present in the secondary flow. This appears to be a travelling wave system created by shear layer structures that are convecting supersonically with respect to the low-speed secondary stream; these wave systems have been observed before[15,38,39]. As with Dimotakis, the shadowgraph images are unable to reveal the precise nature of the shear layer structures which created the travelling waves.

It should be noted that these cannot be standing waves because the secondary Mach number is much less than unity at test startup, when pressure ratios are low (in the case of Figure VII-11, the pressure ratio is only 4). They are only visible for roughly 0.1 seconds at the start of the test, when the primary chamber pressure is ramping up and the secondary flow rapidly accelerates from low subsonic speeds.

The wave system seems to be comprised of at least one wave originating at the shear layer. Specifically, the wave seems to originate in the recirculation region immediately after the primary nozzle lip. Subsequent waves reflect alternately off the mixing duct wall and shear layer/plume boundary as they move downstream. According to classical gas dynamic theory, each wave must reflect alternately as a compression or expansion wave and thus balance each other in order to maintain a negligible streamwise pressure gradient. These traveling waves were observed at the start of each test and using each nozzle. However, due to the transient conditions associated with test startup the exact wave system was unique to each test.

While the shocks seen at test startup could only have been travelling waves due to the conditions of the flow, standing waves were also observed within the secondary flow during each test. In fact, there is an observable transition from the traveling wave system to the standing waves that occurs over approximately 0.1 seconds. Once the rocket reaches a pressure ratio near 60, the traveling waves slowly move upstream and coalesce into a standing wave. The wave becomes rooted near the secondary duct outlet, with its exact location dependent on the thickness of the nozzle lip used during that test. Specifically, the standing shock is located between 0 and 1 inch downstream of the secondary duct exit. The thinnest lip nozzle's shock is closest to the secondary duct exit,

while the thickest lip nozzle's shock is furthest downstream. The coalescence of the standing shock occurs as the primary plume reaches an underexpanded condition, and it remains visible throughout the test until the plume becomes overexpanded again. Hence, the wave is visible for approximately 1-2 seconds, starting at pressure ratios around 60 and staying there until the rocket achieves the maximum pressure ratio. Figure VII-12 is an example of the standing shocks visible at the secondary outlet.
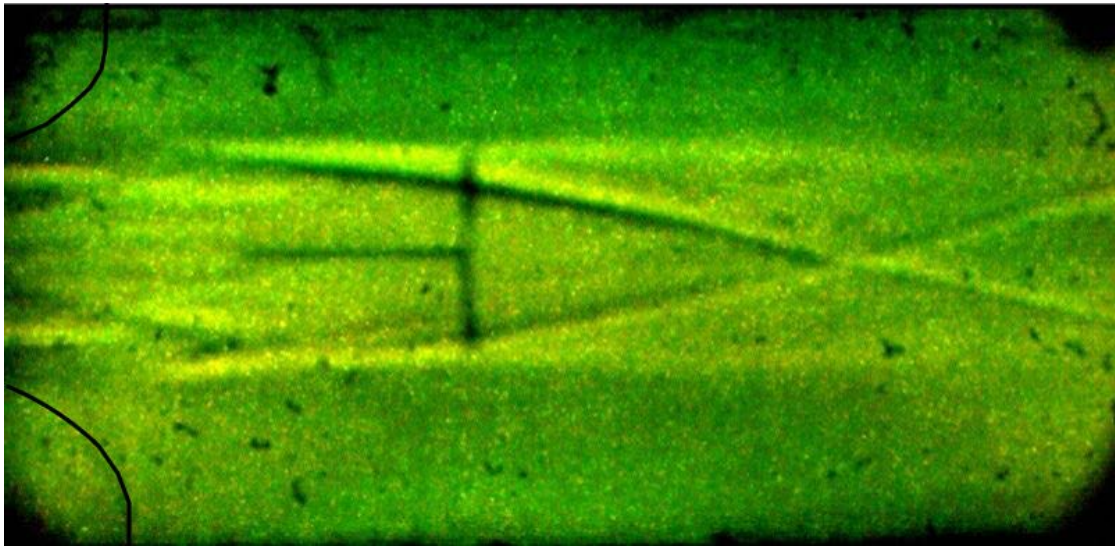
Figure VII-12. Nozzle B3, Test 68, PR = 60. Standing shocks in secondary flow.

A standing wave at the secondary-to-mixing duct entrance is expected in the saturated supersonic case, when the primary plume is optimally expanded and the secondary entrance becomes the point of minimum area for the secondary flow. However, during the majority of the test the primary flow is in a state of underexpansion and the primary plume impinges on the secondary flow, creating a point of minimum area further downstream. This downstream location is where one would expect to see a standing wave, and some tests do show a weak standing wave there, but even in those cases the standing wave at the duct entrance also remains visible. One possible explanation is that the recirculation region immediately behind the nozzle lip produces shear layer vortices

capable of locally accelerating the flow to supersonic speeds. As with the traveling waves, this phenomenon has been observed before[15]. Figure 7-13 shows what these high energy recirculation vortices might look like.
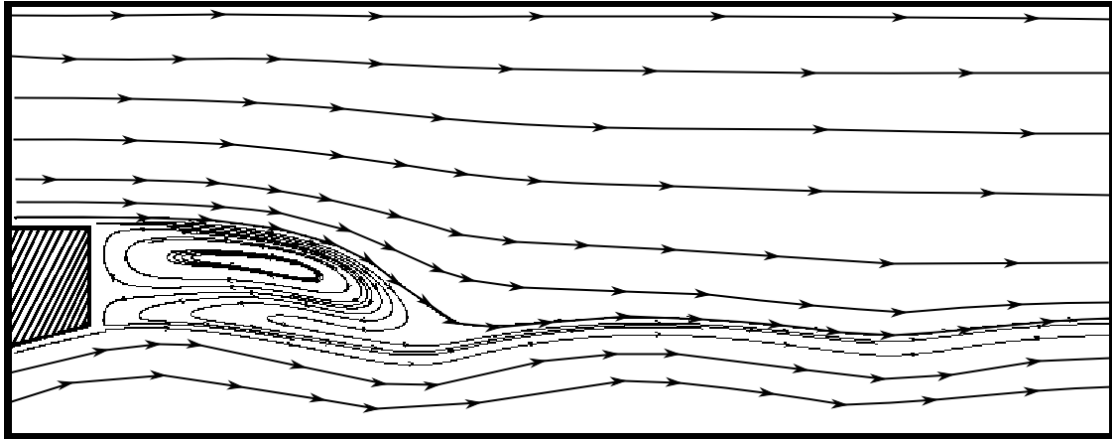
Figure VII-13. Vortices formed in nozzle lip recirculation region.

If the recirculation region is indeed producing turbulent structures that convect supersonically, it would explain why the standing waves are more visible in tests using the thicker nozzle lips – a thicker lip should produce more powerful vortices in the recirculation region. The standing waves also have a distinct curvature between their formation in the recirculation region and the mixing duct wall; this may be the result of their interaction with the boundary layer along the mixing duct wall.

VIII.   Experimental Performance Results

Presented here are the performance-related data collected during the formal testing process. Specifically, the effects of each nozzle on secondary entrainment, wall pressure data, and primary plume pressures are discussed. These results are compared to previous conclusions found using the apparatus's original conical nozzle design.

A.   Mixing Duct Flow Field Diagnostics

As mentioned previously, two configurations were used in testing the Cal Poly AAR. The first, using plexiglass upper and lower surfaces in the mixing duct, was intended primarily for flow visualization. The second, using pressure ports located along the centerline of the lower mixing duct surface, allowed for direct measurement of the primary plume flow field for comparison with mixing duct wall pressures.

Mixing duct wall pressure profiles for each nozzle are shown in Figure VIII-1. Each figure shows a sharp drop in pressure as the secondary flow chokes and then a pressure spike sometime later as the flow unchokes. The figures demonstrate an inverse relationship between nozzle lip thickness and the duration of secondary flow choking. For example, Test 79 shows that with the thinnest nozzle lip, the flow chokes for nearly 1.5 seconds. In contrast, during Test 72 with the thickest nozzle lip, the secondary is choked for approximately 1 second, roughly a 30% reduction in choking time. Nozzle B2 is an exception to this trend, as it chokes only briefly (approximately 0.2 seconds). The short choke time associated with Nozzle B2 may be due to the unsteadiness it produced during each test, a factor which was discussed previously.
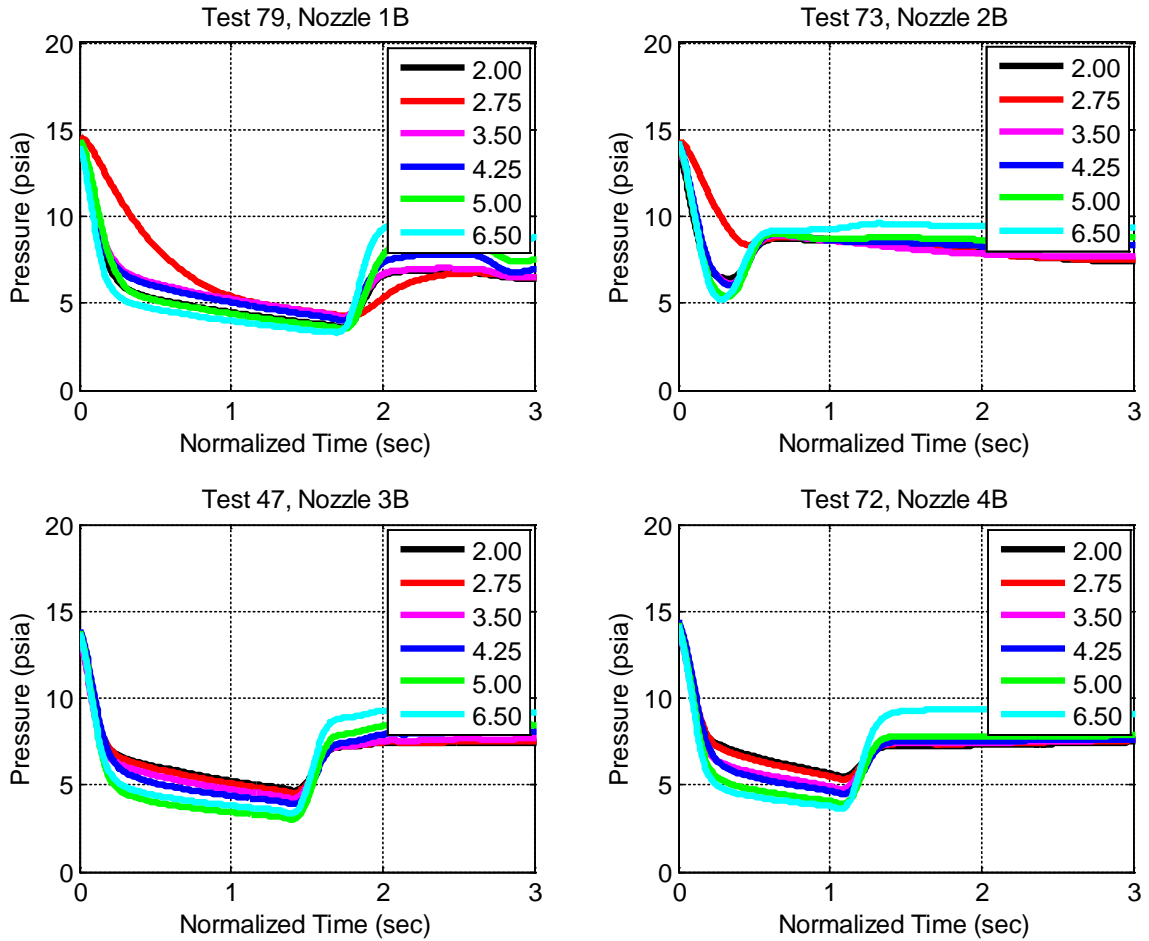
Figure VIII-1. Tests 79, 73, 47, 72: Mixing duct wall pressures.

The cause of the relationship between nozzle lip thickness and secondary flow choking is less obvious. One possible reason is that while a larger nozzle lip may produce a larger shear layer, the primary plume itself impinges more on the secondary with the thinner nozzle lip, because the two flows are simply physically closer together. This theory is supported by results from the CPSE Simulation, which also indicates more primary plume impingement as nozzle lip thickness decreases. It makes sense that the simulation produces such results, as its inviscid assumption does not account for the shear layer between the two flows and instead only predicts how far the primary plume will expand into the secondary. If the duration of secondary flow choking does in fact depend on

nozzle lip thickness, it has profound implications for the performance of the Cal Poly AAR. It indicates that the ejector's ability to choke the secondary flow is primarily an inviscid phenomenon, while its capability for maximizing secondary entrainment is driven by viscous forces.

Figure VIII-2 shows the same trends as Figure VIII-1, only in terms of the distance downstream of the nozzle exit instead of with respect to time. As with Figure VIII-1, the wall pressures are shown to decrease as pressure ratio increases. This makes sense, because as the pressure ratio increases, the primary flow exerts more of a shear force on the secondary, causing it to speed up and thus decrease in pressure. Also worth noting for Nozzles B2 and B4 are the sudden changes in shape of the pressure profiles at pressure ratios of 120 and 140, respectively. In these cases, the Fabri choke point is moving upstream and causing a sharp rise in pressure behind its standing normal shock. For Nozzle B2, the choke point appears to be at approximately 3.5 inches downstream of the nozzle exit for a pressure ratio of 120, while for Nozzle B4 it settles around 4.5 inches downstream for pressure ratios above 140.
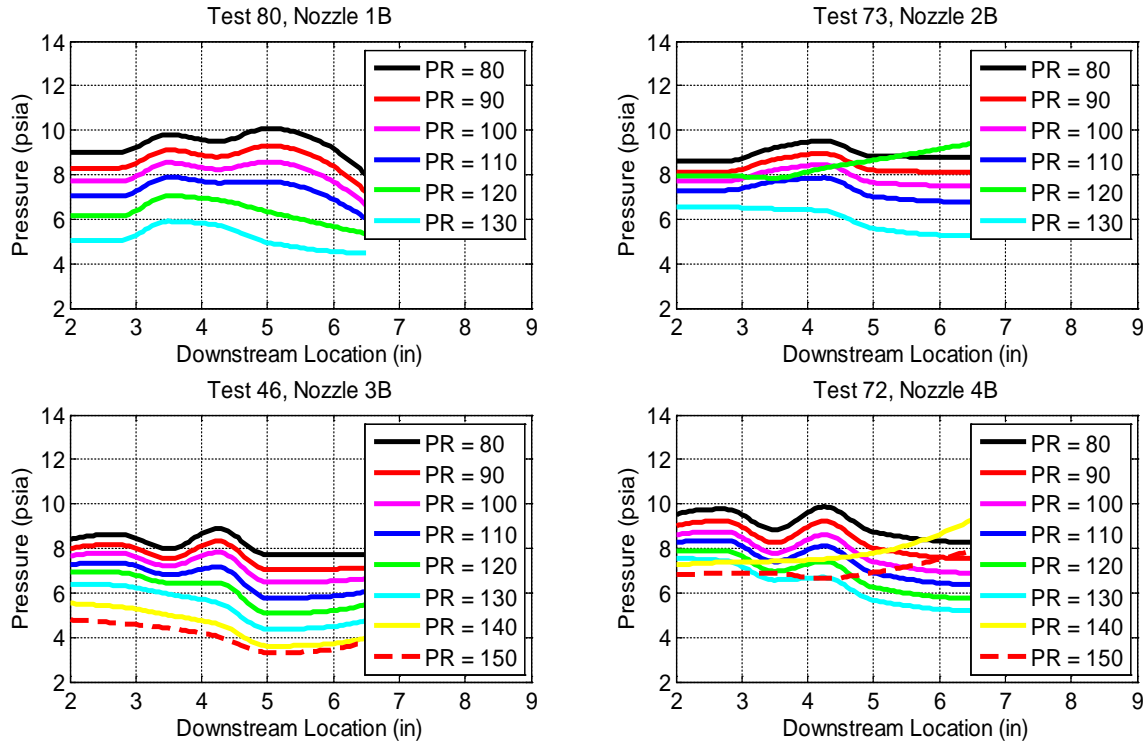
Figure VIII-2. Tests 79, 73, 47, 72: Right mixing duct wall pressures.

Centerline pressures recorded for the same nozzles exhibit the propagation of similar pressure phenomena. Figure VIII-3 shows centerline pressures recorded along the length of the mixing duct downstream of the primary nozzle exit for each of the four nozzles. As shown in the figure, the pressures in the primary plume exhibit the same sharp pressure drop and rise at the beginning of a test that is evident in the mixing duct wall pressure data. Unlike the wall data, however, the first pressure drop does not follow a trend with lip thickness. This makes sense, as centerline data only depends on conditions inside the plume – thus, the first pressure drop simply indicates that the flow is highly underexpanded.

The entire trend in centerline pressures can be explained by the changing shock structure within the primary plume. For example, visible after the first pressure drop are steady pressure oscillations at each point downstream of the nozzle exit. Each oscillation corresponds to a coalesced wave front (aka a strong normal shock) propagating upstream

through the plume. The upstream movement of the shock is a function of the angle of the initial expansion fan emanating from the nozzle lip. At the start of the test the plume is highly underexpanded and thus the initial Prandtl-Meyer expansion angle is very large. As a result, the reflected compression wave from the plume boundary is very shallow and moves far downstream before coalescing into the normal shock. As the primary pressure decreases so does the Prandtl-Meyer angle, and the angle of the reflected compression wave becomes sharper. Due to the sharper reflection, the compression waves coalesce sooner and the shock front moves further upstream as a result.
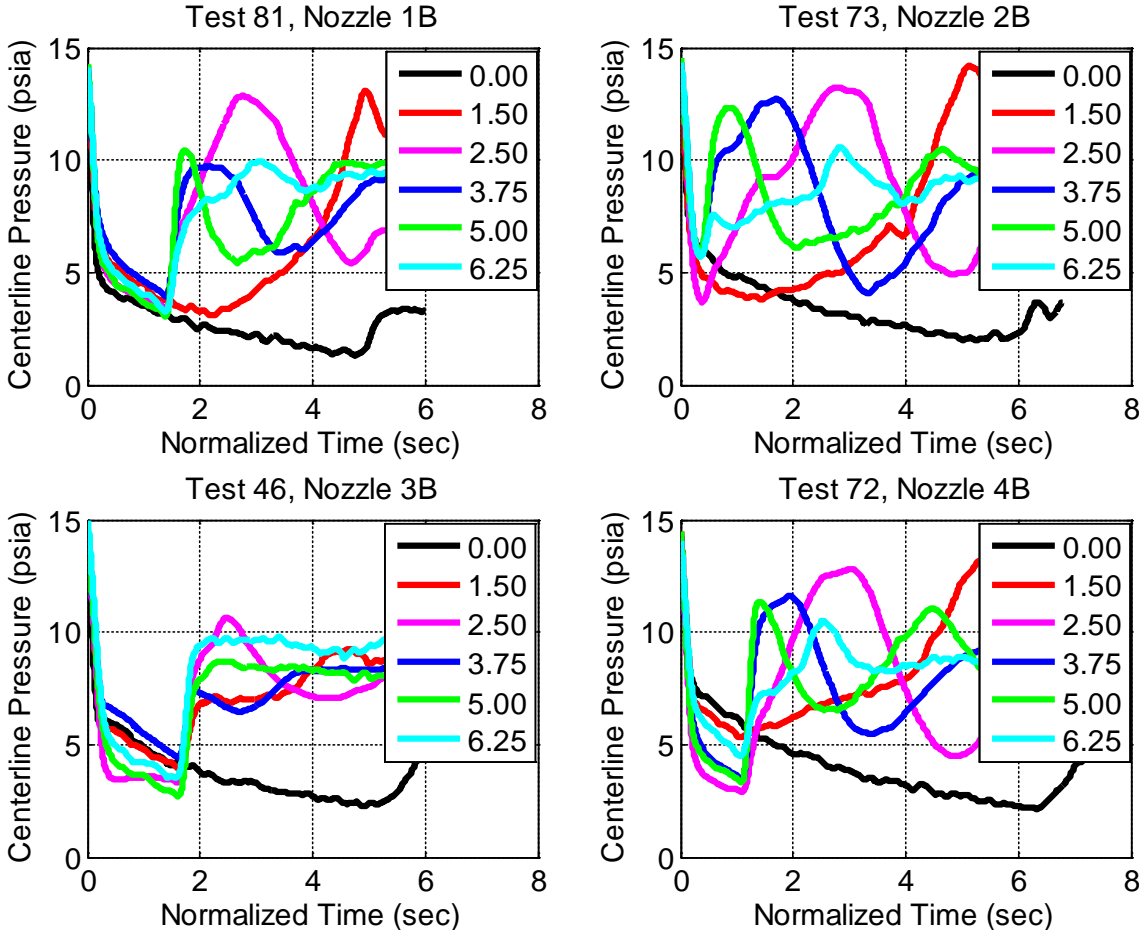
Figure VIII-3. Tests 81, 73, 46, 72: Centerline pressures.

B. Blocked Flow Case

The case of blocked flow is characterized by a primary plume that expands all the way out to come in contact with the mixing duct walls, blocking off secondary flow. Predictions indicate that the primary to secondary stagnation pressure ratio necessary to achieve this condition must be very high. Specifically, the model created by Morham based on Gist's testing results predicted that blocking would occur at pressure ratios near 230. Sanchez built a plenum to connect to the secondary flow in order to achieve those high pressure ratios. However, while Sanchez achieved pressure ratios as high as 221, bringing entrainment ratios down to as low as 5%, he never conclusively showed a blocked condition. Based on Sanchez's results, it was thought that blocking might never be decisively demonstrated. One explanation for such a lack of evidence was the possibility that boundary layer flow along the mixing duct wall might still allow a small amount of secondary flow to enter the duct even if severely impinged upon by the primary plume.

In contrast with Sanchez's results, Test 71 using Nozzle B4 suggested that a blocked case had been achieved. These results were repeated again during Test 72 using the same nozzles. The maximum pressure ratios achieved during Tests 71 and 72 were 147 and 159, respectively. Figure VIII-4 through Figure VIII-6 demonstrate flow conditions of the blocked flow case in Tests 71 and 72. As the figures demonstrate, there is no secondary flow entrainment. As a result, the secondary flow velocity and mass flow rate are driven to zero.
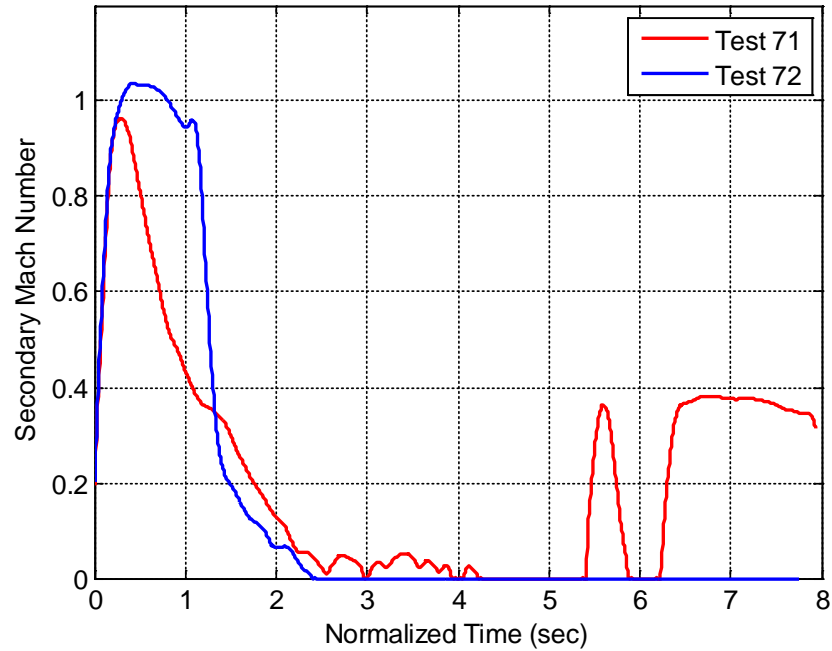
Figure VIII-4. Nozzle 4B, Tests 71 & 72: Secondary Mach number, blocked case.
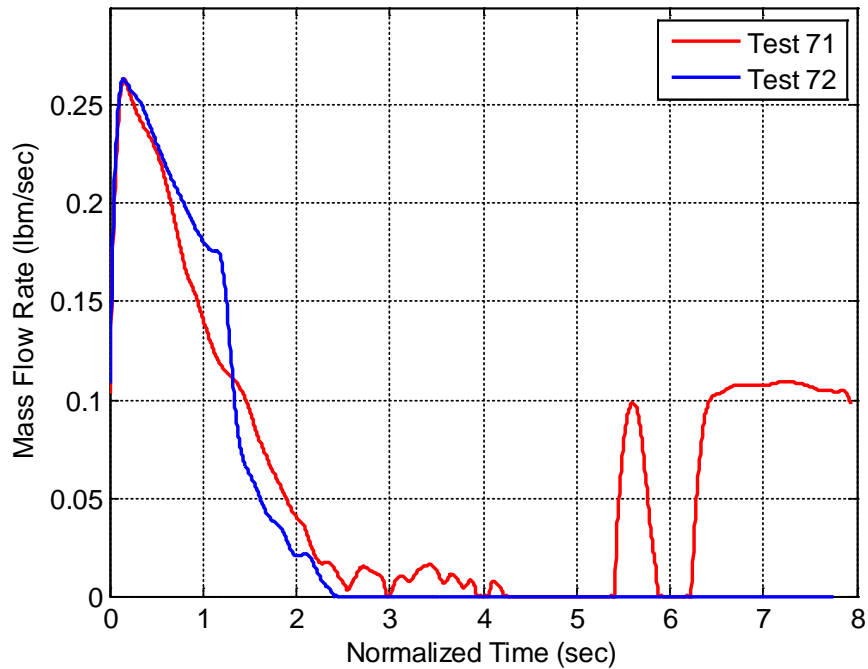
Figure VIII-5. Nozzle 4B, Tests 71 & 72: Secondary mass flow rate, blocked case.

The secondary duct pressures shown in Figure VIII-6 also highlight the blocked flow condition. Similar to the saturated supersonic case, the static pressure in the secondary stream remains nearly constant. However, in the blocked condition the secondary static

103

pressure is also equal to the stagnation pressure from which the air is being entrained. As the figure shows, between 4 and 9 seconds after the test starts, the static pressure in the left secondary duct remains nearly identical to both the stagnation pressures recorded in the plenum and left secondary duct.
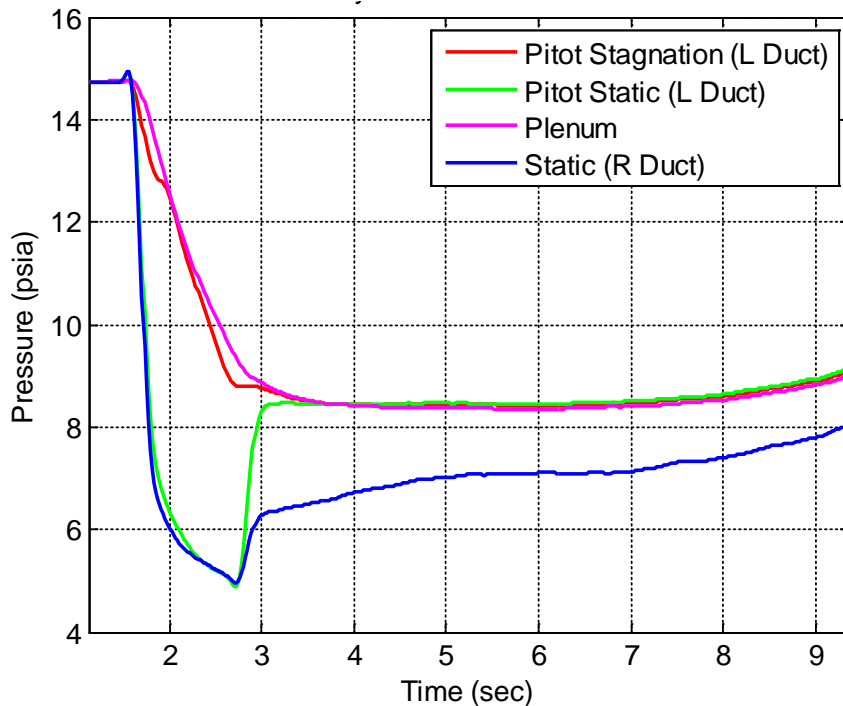
Figure VIII-6. Nozzle 4B, Test 72: Recorded secondary pressures, blocked case.

Figure VIII-7 shows the experimental performance curve from Tests 71 and 72. As highlighted in the figure, the secondary flow entrainment decreases as pressure ratio increases. The figure also shows that the flow achieves secondary blocking, when the entrainment ratio suddenly drops to zero. The surprising result from Figure VIII-7 is the fact that the secondary flow blockage doesn't occur at the maximum pressure ratio. Entrainment steadily decreases as the pressure ratio increases up to 160, then briefly increases before suddenly dropping off to zero at a pressure ratio near 120. Also worth noting is the fact that the secondary flow remains blocked as the pressure ratio continues to decrease, staying blocked at pressure ratios as low as 40 in Test 72.
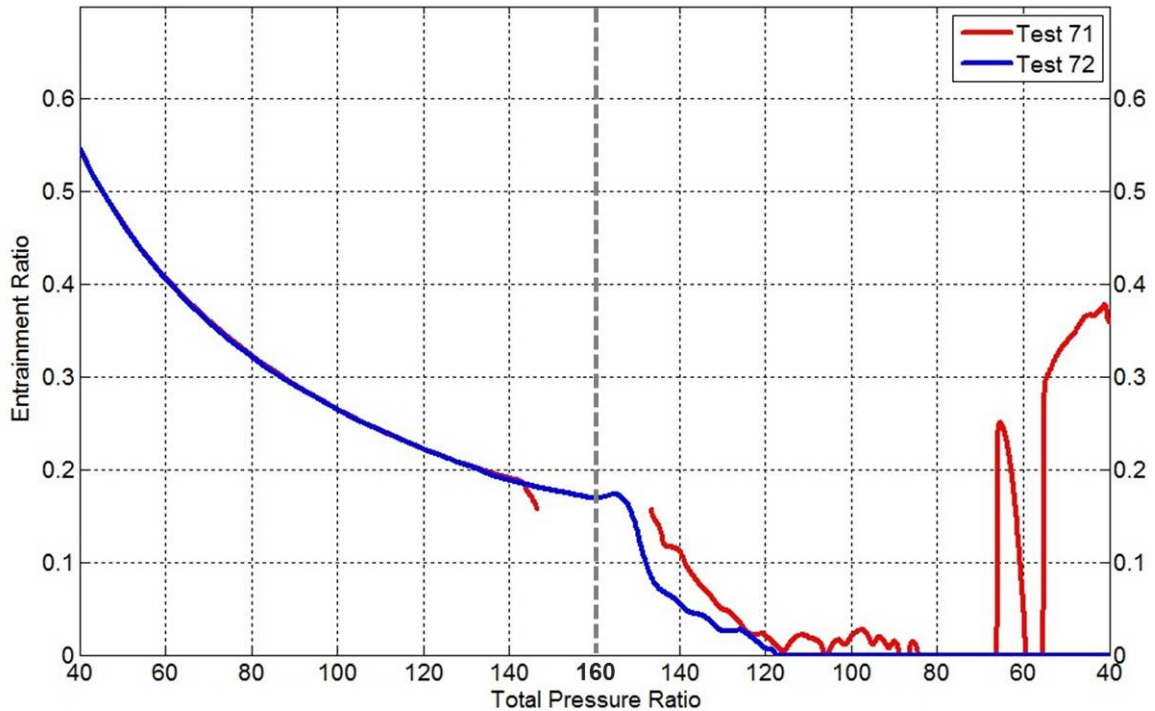
Figure VIII-7. Nozzle 4B, Test 71 & 72: Experimental performance, blocked case.

Figure VIII-7 thus presents a dilemma. Theory dictates that as pressure ratio increases, the primary plume will expand further out until it impinges on the duct wall; thus, if secondary flow blockage does occur it will happen at a very high pressure ratio when the primary plume is highly underexpanded, and continue to remain blocked until the pressure ratio drops below that value. In Tests 71 and 72, however, not only does blockage appear to occur after the pressure ratio has peaked and is decreasing, but it apparently remains blocked even at very low pressure ratios, when the primary plume is overexpanded. One explanation for this flow behavior lies with the larger lip thickness of Nozzle B4, which should create a larger shear layer than is present in any of the other cases. A very asymmetric flow condition, which might be possible as pressure ratio decreases and the primary plume becomes overexpanded, might cause the primary plume and thicker shear layer to shift entirely to the left wall of the mixing duct, thus producing

105

a blocked condition on one side of the duct but not the other. Such extreme flow asymmetry was also observed during tests by Gist[9].

It is also important to note that pressures in the right secondary duct do not indicate that the secondary flow is blocked on that side. There is no recorded stagnation pressure in the right duct, but when the right static pressure is compared to the stagnation pressure in the plenum there is a difference of several psi. In contrast, the static pressure in the left duct matches both the stagnation pressures measured in the duct and in the plenum. Mixing duct wall pressure data on the right duct wall also lacks an indication of primary plume impingement. Unfortunately, because of a lack of visual data to supplement the pressure data, there is no way of verifying exactly what is causing the left secondary flow to become blocked.

C. Entrainment Comparisons

The primary objective of this investigation has been to analyze the effects of primary nozzle lip thickness on the Cal Poly AAR's performance characteristics. This section will discuss the nature of the experimental performance results from each nozzle. There was a very high degree of repeatability between tests using the same nozzles, with an average performance error for each nozzle of 2.7-3.0% across all tests for that nozzle.

Figure VIII-8 shows the experimental performance curves from tests 33, 79, 73, 47, and 72, representing each of the four bell-mouth nozzles as well as the original conical design. The figure presents a clear trend indicating that, for a given pressure ratio, entrainment ratio increases with nozzle lip thickness. The difference between performance curves is significant. For example, at a pressure ratio of 125, the average difference between entrainment ratios is almost 13%.
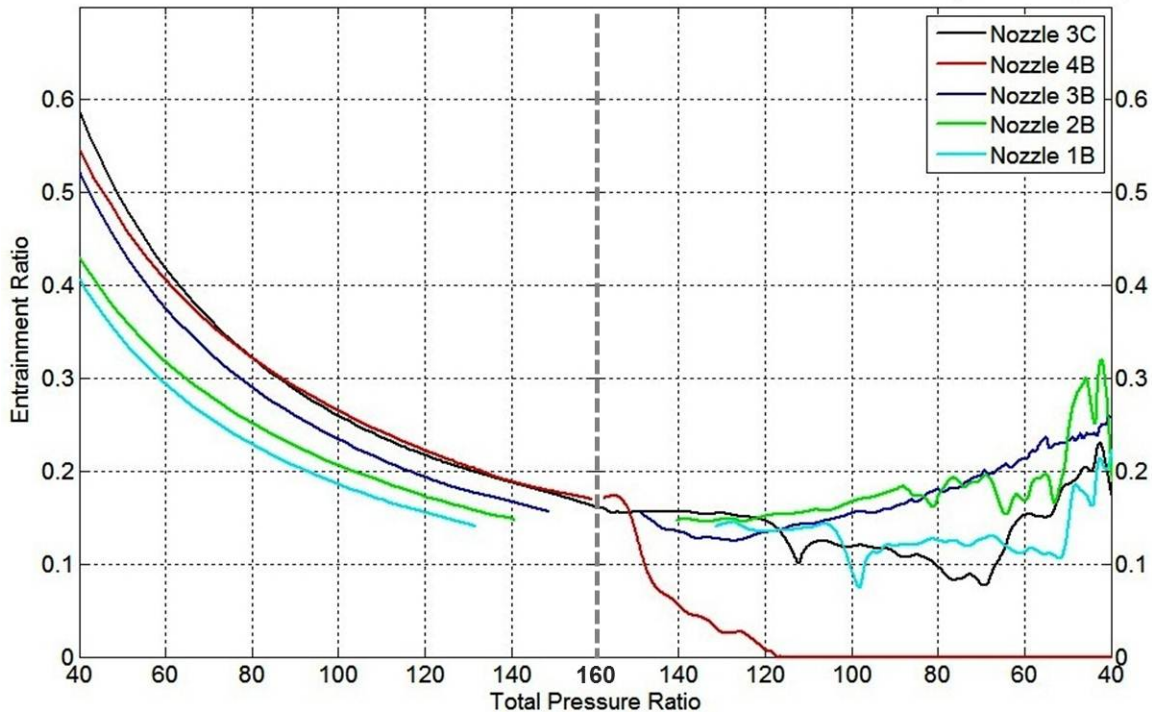
Figure VIII-8. Tests 33, 79, 73, 47, 72: Experimental performance comparison.

The figure also demonstrates that not all nozzles achieved the same maximum pressure ratio. In fact, the maximum pressure ratio achieved also increased with nozzle lip thickness. This trend indicates that the entrainment ratio and pressure ratio are closely linked. The data suggests that for a given pressure ratio, entrainment ratio is higher with a thicker nozzle. Thus, more secondary air is entrained at a faster rate, meaning that the secondary stagnation pressure drops faster, which in turn produces a larger difference in stagnation pressure between the primary and secondary flows.

The trend of increased pressure ratio and entrainment ratio with nozzle lip thickness extends throughout the performance regime of the AAR, from low pressure ratios up to and beyond the point of Fabri choking, where the secondary entrainment is limited by the sonic condition at its aerodynamic throat. These trends break down once the pressure ratio reaches its maximum value; as pressure ratio falls, the entrainment ratio fluctuates

unpredictably and independently of the lip thickness of the nozzle in use. This fluctuation is due to several factors. Primary among these is the re-choking that may occur as the primary nozzle enters the overexpanded condition. The general unsteadiness of the primary plume as it breaks down at low pressures may also play a large role in the unpredictable secondary entrainment – this is especially true when the primary flow unchokes and becomes subsonic at low chamber pressures. At this point, the subsonic primary flow does not produce enough shear force on the secondary to maintain the low pressures present in it, and the flow fluctuates unpredictably as ambient air is drawn back into the mixing duct to equalize the pressure in the plenum.

Figure VIII-9 presents an alternative way of comparing ejector performance for the different nozzles tested. Entrainment ratio is plotted against nozzle lip thickness at several different pressure ratios. In all cases, there is an approximately linear trend of entrainment ratio increasing with nozzle lip thickness. It is also consistent with Figure VIII-8 in showing that the entrainment ratio approaches a minimum at pressure ratios beyond 120. This minimum is between 0.14 and 0.21, corresponding with the thinnest and thickest nozzle lips, respectively.
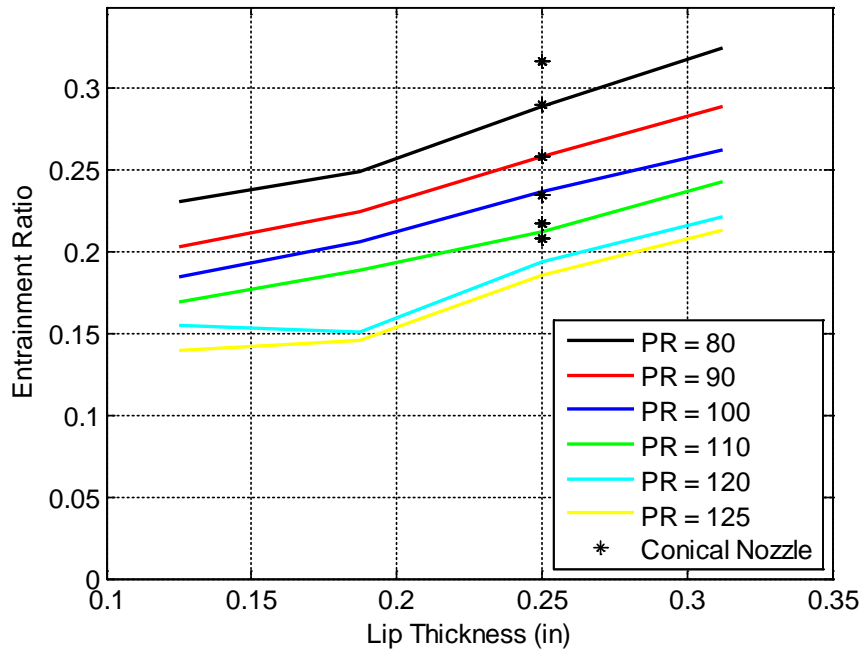
Figure VIII-9. Tests 33,79,73,47,72: Increase in performance with nozzle lip thickness.

Also apparent from Figure VIII-8 and Figure VIII-9 is the fact that the original conical

nozzle design used by Sanchez and Popish, which has a lip thickness of 0.25 inches,

produces entrainment ratios equal to or greater than the thickest-lipped bell-mouth

design, which is 0.3125 inches. The conical design thus seems to be more efficient at

entraining air than the bell-mouth design. One possible reason for this increase in

efficiency is the angle at which the primary flow intersects the secondary flow. A bell-

mouth nozzle is designed to curve the flow along the nozzle wall until it exits

approximately parallel to its centerline. In a conical nozzle, the flow along the wall exits

at a constant angle equal to the nozzle's half-angle. Because the primary flow exits the

conical nozzle at a larger angle with respect to the secondary flow, it produces more force

on the secondary flow, which in turn increases the growth rate of the shear layer that

forms between the primary and secondary. Thus, the data in this case suggests that the

primary nozzle flow angle has a larger impact on shear layer growth and secondary

entrainment than the recirculation region created in the wake of the primary nozzle lip (which is directly proportional to the nozzle's lip thickness). The more far-reaching result of this conclusion is that in an ejector, the loss in efficiency that results from using a conical nozzle over a bell-mouth design of the same length may be more than offset by the fact that the conical design is more efficient at entraining secondary air. Thus, any potential future AAR design might use a conical nozzle for better mixing and thrust augmentation.

Some of the trend of increased entrainment ratio with nozzle lip thickness can also be explained by increases in primary mass flow rate as nozzle throat area is varied. As explained before, in order to vary nozzle lip thickness without changing the exit velocity of the primary flow, the nozzle throat area must also change. When that area is increased, it allows more mass to flow through it. Thus, the nozzle with the thinnest lip also has the largest throat, allowing for the largest primary mass flow rate for a given primary chamber pressure. If secondary mass flow rate remains relatively constant as primary mass flow rate increases with a larger nozzle throat area, then the ejector appears to have less efficient entrainment capabilities. This trend is best highlighted in Figure VIII-10, which shows entrainment ratio for each of the nozzles as a function of primary mass flow rate.
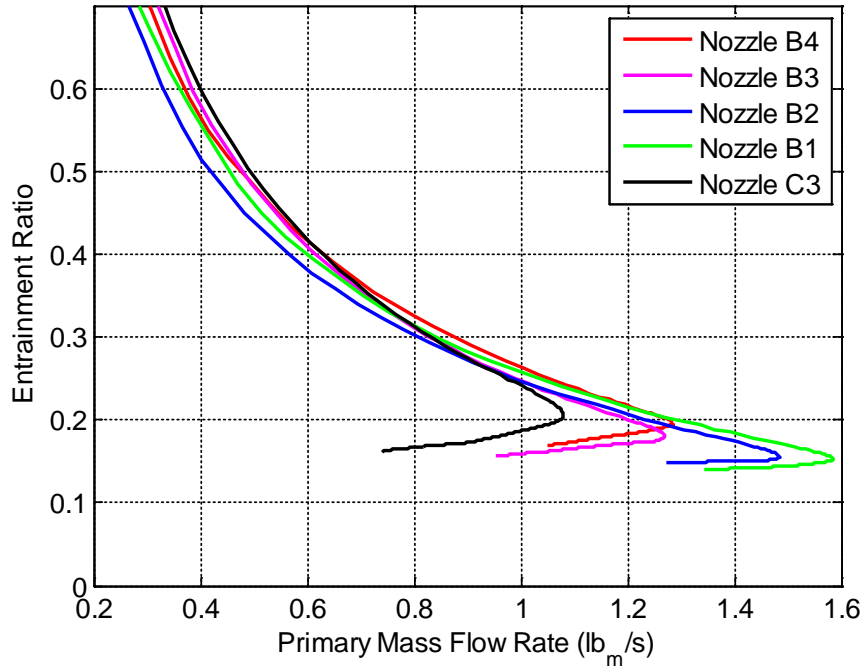
Figure VIII-10. Tests 33,79,73,47,72: Entrainment trends with primary mass flow rate.

As the figure demonstrates, there is a trend of decreasing entrainment as primary mass flow rate increases. However, the increase in primary mass flow rate, which is on the order of 9-10% between increments of lip thickness, is still less than the observed 13-15% increase in entrainment ratio between lip thicknesses at a given pressure ratio. These results thus indicate that the overall increase in efficiency with nozzle lip thickness is closer to 4-5%, when the change in primary mass flow rate is taken into account.

D.   CPSE Simulation Results

The CPSE simulation was used to compare theoretical predictions for secondary entrainment with measured experimental values. While the simulation indicated trends in line with those produced from the experimental data, the values themselves were drastically different. In every case examined the simulated entrainment ratio is higher than the experimentally calculated entrainment ratio, sometimes by as much as 140%.

The trend is also much steeper for the theoretical predictions than for the experimental data. While some of this difference may be attributed to the simulation's simplifying assumptions, especially its inviscid treatment of the two flows, evidence also suggests that in its current state the simulation has been tailored to the original AAR configuration used by Gist. When one of the simulation's input variables such as nozzle throat area, contour, or lip thickness is altered, it drastically changes the simulation's predictive results, and often times the simulation is unable to converge on a solution at all. As a result, the CPSE simulation in its current form cannot be reliably used to extrapolate to alternate test setups.

IX.   Formal Conclusions

As part of the ongoing Cal Poly AAR Research Project, testing was performed using a cold-flow simulated AAR operating as a mixer-ejector. Specifically, the conical primary nozzle used in the original test apparatus was replaced with several bell-mouth designs. Nozzle base lip thickness was varied in order to investigate its effect on the AAR's entrainment capability and the viscous interactions between the primary and secondary streams in the AAR mixing duct. Focused shadowgraphy was used to characterize the resulting flow field, with supplemental data coming in the form of recorded pressures and temperatures. The results were compared to inviscid theoretical predictions. The following conclusions were made based on the experimental findings.

1.   Shadowgraph images of the flow reveal shock waves anchored inside the nozzle and interacting with the shocks shed from the nozzle lip, generating a double-diamond pattern in the primary plume. There is an inverse relationship between nozzle throat area and the oblique shock angle visible at the nozzle exit plane.

2.   Most nozzles exhibit very symmetric flow conditions. Nozzle B2 is the exception, with visual data indicating unsteadiness and asymmetry. Flow unsteadiness is the primary cause of secondary duct asymmetry due to periodic secondary re-choking.

3.   Test repeatability is excellent for all nozzles in both shadowgraph and centerline pressure configurations.

4.   Shadowgraph images show a travelling wave system present in the secondary flow at test startup. The waves appear to originate in the recirculation region

immediately after the primary nozzle lip. The waves may be created by shear layer structures convecting supersonically with respect to the secondary flow.

5. The duration of secondary flow choking is inversely proportional to nozzle lip thickness. This is a result of the primarily plume being physically closer to the secondary flow with a thinner nozzle lip. It also indicates that the ejector's ability to choke the secondary flow is primarily an inviscid phenomenon.

6. Secondary flow blockage has been demonstrated in two consecutive tests using the thickest nozzle lip. Only the left secondary duct is blocked in each case. Blockage was only demonstrated in the centerline pressure configuration, so no visual evidence is available to support the blocked flow theory.

7. At every pressure ratio, entrainment ratio is shown to increase with nozzle lip thickness. The original conical nozzle produces the largest level of entrainment, indicating that the angle of primary flow impingement is the largest contributing factor to secondary entrainment.

8. The increase in efficiency resulting from a bell-mouth nozzle is less than the increase in entrainment efficiency of a conical nozzle, indicating that the conical design is more efficient overall for air augmented rocket applications.

9. The CPSE simulation is unable to accurately predict AAR performance when its inputs are changed from the original Cal Poly AAR configuration. Soft coding some of its input parameters may improve its predictive capability.

X. Future Work

The research performed for this project has its roots in previous efforts by several other individuals. Its primary intention is therefore to supplement that data in order to build a more complete picture of the mixer-ejector flow field for use in future air augmented rocket applications. The hardware constructed for this project also supplements the original test apparatus. Using this combined knowledge and with the materials already available, several topics become feasible for future work.

The most immediately beneficial work would be to enhance the current theoretical model used for predictive analysis through the incorporation of viscous and heat transfer effects. By integrating friction losses, turbulent mixing, and even rarified gas effects, the model could serve as a bridge between current cold flow tests and hot-fire applications. Validating the model would require a return to hot-fire testing, which is strongly recommended if the project is to serve its intended purpose in RBCC concept development.

Future testing would also be simplified immensely with the addition of pressure regulating systems for both the primary and secondary flows. Currently, both streams are transient throughout the course of a test, making repeatability difficult and limiting the tests to very short timeframes. Adding a pressure regulator in the primary and a plenum capable of maintaining a steady, low-pressure condition in the secondary would make correlation with the current theoretical model more valid, while also bringing the conditions in the Cal Poly AAR closer to those in an actual RBCC air-launch scenario.

The current flow visualization system could also be improved upon in future works. The addition of a more powerful light source, larger, more precise mirrors, and better focusing

and stabilizing equipment for video recording could make actual Schlieren visualization possible and thus produce a much more detailed view into the internal structures of the shear layer in the AAR mixing duct. Other flow visualization options, such as flow seeding, Particle Image Velocimetry (PIV), or Laser Doppler Anemometry (LDA) could also provide a better understanding of the turbulent mixing that occurs in the shear layer. Finally, future work should focus on applications. The intended use for ejectors in any RBCC concept is thrust augmentation, so the cumulative goal in testing the Cal Poly AAR must be to investigate its thrust-augmenting capability. Specifically, one final work should combine all of the knowledge acquired as part of the project in order to determine the effects of various input conditions on mixing efficiency and thrust augmentation, while also drawing correlations between cold flow and hot-fire data in order to be able to accurately extrapolate cold flow results to more real-world hot-fire scenarios.

XI.   References

1. Hallion, Dr. Richard P., " The History of Hypersonics: or, "Back to the Future-Again and Again"," *43rd AIAA Aerospace Sciences Meeting and Exhibit*, American Institute of Aeronautics and Astronautics, Reno, NV, 2005.

2. Bussing, T., and Pappas, G., "An Introduction to Pulse Detonation Engines", *32nd AIAA Aerospace Sciences Meeting and Exhibit*, American Institute of Aeronautics and Astronautics, Reno, NV, 1994.

3. "Pulsed Detonation Engines." *UT Arlington's Aerodynamics Research Center*. University of Texas at Arlington, 2011. Web. 04 Apr. 2011. <http://arc.uta.edu/research/pde.htm>.

4. Graham, Richard H. *SR-71 Revealed: the inside Story*. Osceola, WI, USA: Motor International, 1996. Print.

5. Hank, J.M., Murphy, J.S., and Mutzman, R.C., "The X-51A Scramjet Engine Flight Demonstration Program", *15th AIAA International Space Planes and Hypersonic Systems and Technologies Conference*, American Institute of Aeronautics and Astronautics, Dayton, OH, 2008.

6. Bedke, Curt. "High Speed Weapons: What is Different Today", AF T&E Days, Air Force Research Laboratory. February 2nd, 2010.

7. Barber, T.A., Maicke, B.A., and Majdalani, J., "Current State of High Speed Propulsion: Gaps, Obstacles, and Technological Challenges in Hypersonic Applications", *45th AIAA/ASME/SAE/ASEE Joint Propulsion Conference & Exhibit*, American Institute of Aeronautics and Astronautics, Denver, CO, 2009.

8. Trefny, C.J., and Roche, J.M., "Performance Validation Approach for the GTX Air-Breathing Launch Vehicle", *NASA Glenn Research Center*, Cleveland, OH, 2002.

9. Gist, D.R., "Examination of Flow Field Characteristics and Fabri-Choking of a 2-D Augmented Rocket", Master's Thesis, Department of Aerospace Engineering, Cal Poly, San Luis Obispo, CA, 2007.

10. Fabri, J., & Paulon, J., "Theory and Experiments on Supersonic Air-to-Air Ejectors", NACA TM 1410, Sept 1956.

11. Fabri, J., and Siestrunk, R., "Supersonic Air Ejectors", Advances in Applied Mechanics, Vol. 5, Von Karman and Dryden, editors, Academic Press, 1958, pp. 1-35.

12. Addy, L.A., "On the Steady State and Transient Operating Characteristics of Long Cylindrical Shroud Supersonic Ejectors", University of Illinois, Ph. D. dissertation. University Microfilms, Inc. Ann Arbor, MI., 1963.

13. Emanuel, N.G., "Comparison of One-Dimensional Solutions with Fabri Theory for Ejectors", *Acta Mechanica* 44, pp. 187-200, 1982.

14. Papamoschou, D., "Analysis of Partially Mixed Supersonic Ejectors", *Journal of Propulsion and Power*, Vol. 12, No. 4, July 1996.

15. Hall, J.L., Dimotakis, P.E., and Rosemann, H., "Experiments in Non-Reacting Compressible Shear Layers", *29th Aerospace Sciences Meeting*, American Institute of Aeronautics and Astronautics, Reno, NV, 1991.

16. Dimotakis, P.E., "Turbulent Free Shear Layer Mixing and Combustion" in Murthy, S.N.B., Curran, E.T., editors, *High-Speed Flight Propulsion Systems*, Progress in Astronautics and Aeronautics, Vol. 137, 1991, pp. 265-340.

17. Papamoschou, D., and Roshko, A., "The Compressible Turbulent Shear Layer: An Experimental Study", *Journal of Fluid Mechanics*, Vol. 197, 1988, pp. 453-477.

18. Anderson, Bernhard H. "Factors Which Influence the Analysis and Design of Ejector Nozzles", *NASA Lewis Research Center*, Cleveland, OH, 1972.

19. Matsuo, K., Sesaguchi, K., Kiyotoki, Y., and Mochizuki, H., "Investigation of Supersonic Air Ejectors (Part 2, Effects of Throat-Area-Ratio on Ejector Performance)", *Bulletin of JSME*, Vol. 25, No. 210, 1982, pp. 1898-1905.

20. Lee, J.-H., Kumar, V.R.S., Kim, H.D., Bo-Gyu, C., Kim, K.H., and Setoguchi, T., "Studies on Flow Characteristics of Variable Ejector Systems", *42nd AIAA/ASME/SAE/ASEE Joint Propulsion Conference & Exhibit*, American Institute of Aeronautics and Astronautics, Sacramento, CA, 2006.

21. Enomoto, S., Yanagi, R., and Sasaki, M., "Internal Flow Field and Mass Flow Rate of 2-D-CD Ejector Nozzles*", 34th AIAA/ASME/SAE/ASEE Joint Propulsion Conference & Exhibit*, American Institute of Aeronautics and Astronautics, Cleveland, OH, 1998.

22. Ponton, M.K., and Seiner, J.M., "The Effects of Nozzle Exit Lip Thickness on Plume Resonance", *Journal of Sound and Vibration*, Vol. 154, No. 3, 1992, pp. 531-549.

23. Kweon, Y.H., Miyazato, Y., Aoki, T., Kim, H. –D., and Setoguchi, T., "Experimental Investigation of Nozzle Exit Reflector Effect on Supersonic Jet", *Shock Waves*, Vol. 15, No. 3-4, 2006, pp. 229-239.

24. Foster, T.J., "Rectangular Ducted Methane/GOX Thruster", Master's Thesis, Department of Aerospace Engineering, Cal Poly, San Luis Obispo, CA, 2008.

25. Morham, B.G., "Numerical Examination of Flow Field Characteristics and Fabri Choking of 2-D Supersonic Ejectors", Master's Thesis, Department of Aerospace Engineering, Cal Poly, San Luis Obispo, CA, 2010.

26. Sanchez, J., "High Pressure Ratio Flow-field study of a 2-D Air Augmented Rocket", Master's Thesis, Department of Aerospace Engineering, Cal Poly, San Luis Obispo, CA, 2011.

27. Popish, M. "Primary and Secondary Flow Interactions in the Mixing Duct of a 2-D Planer Air Augmented Rocket", Master's Thesis, Department of Aerospace Engineering, Cal Poly, San Luis Obispo, CA, 2011.

28. Omega Engineering, *PX-302 Pressure Transducer Specifications Sheet.* http://www.omega.com/Pressure/pdf/PX302.pdf, 2011.

29. Omega Engineering, *Revised Thermocouple Reference Tables: Type K.* http://www.omega.com/Temperature/Z/pdf/z218-220.pdf, 2011.

30. Settles, G. S. *Schlieren and Shadowgraph Techniques: Visualizing Phenomena in Transparent Media*. Berlin: Springer, 2001. Print.

31. Schnaible, N.R. "Schlieren System for Supersonic Flow Visualization", Senior Project, Department of Aerospace Engineering, Cal Poly, San Luis Obispo, CA, 2002.

32. Olden, G.W., Lineberry, D.M., Linn, C.A.B., Landrum, B.D., and Hawk, C.W., "Low-Cost Flow Visualization for a Supersonic Ejector", *41st AIAA/ASME/SAE/ASEE Joint Propulsion Conference & Exhibit*, American Institute of Aeronautics and Astronautics, Tucson, AZ, 2005.

33. Cipolla, J., (2011). NOZZLE: De Laval Nozzle Analysis (Version 3.2) [Software]. Available from AeroRocket, http://www.aerorocket.com/Nozzle/Validate/Validate.html.

34. M. Jones (2011, March 29). Personal interview.

35. Sutton, George Paul., and Oscar Biblarz. "Nozzle Configurations." *Rocket Propulsion Elements*. 8th ed. New York: John Wiley & Sons, 2001. 75-76. Print.

36. Munday, D., Gutmark, E., Liu, J., and Kailasanath, K., "Flow Structure of Supersonic Jets from Conical C-D Nozzles," *39th AIAA Fluid Dynamics Conference*, American Institute of Aeronautics and Astronautics, San Antonio, TX, 2009.

37. Hadjadj, A., and Perrot, Y., "Numerical Simulation of Transient Supersonic Nozzle Flows", *26th International Symposium on Shock Waves,* Vol. 2, 2009, 979-984.

38. Lowson, M., and Ollerhead, J., "Visualization of Noise from Cold Supersonic Jets", *Journal of the Acoustical Society of America*, Vol. 44, No. 2, 1968.

39. Oertel, H., "Mach Wave Radiation of Hot Supersonic Jets Investigated By Means of the Shock Tube and New Optical Techniques", *Proceedings of the 12th International Symposium on Shock Tubes and Waves*, Jerusalem, 1979.

XII. Appendix

Table XII-1A. Summary of relevant testing parameters and results.

Test #	Nozzle	Area Ratio	Throat Area (in^2)	Exit Area (in^2)	Lip Thickness (in)	Avg M_p	Max $P_{chamber}$ (psi)
29	0	22.3	0.03375	0.753	0.25	N/A	1330
30	0	22.3	0.03375	0.753	0.25	N/A	1758
31	0	22.3	0.03375	0.753	0.25	N/A	1571
32	0	22.3	0.03375	0.753	0.25	4.33	1182
33	0	22.3	0.03375	0.753	0.25	4.41	1414
34	1	10	0.075	0.75	0.25	3.46	887
35	1	10	0.075	0.75	0.25	N/A	469

36	1	10	0.075	0.75	0.25	3.48	827
37	1	10	0.075	0.75	0.25	N/A	563
38	1	10	0.075	0.75	0.25	N/A	788
39	1	10	0.075	0.75	0.25	N/A	407
40	2	10	0.084375	0.84375	0.1875	3.41	571
41	3	10	0.09375	0.9375	0.125	3.54	772
42	0	22.3	0.03375	0.753	0.25	3.93	1053
43	1	10	0.075	0.75	0.25	3.53	1026
44	1	10	0.075	0.75	0.25	3.51	899
45	0	22.3	0.03375	0.753	0.25	4.6	835
46	4	20	0.0375	0.75	0.25	4.36	1498
47	4	20	0.0375	0.75	0.25	4.42	1489
48	4	20	0.0375	0.75	0.25	4.33	1477
49	0	22.3	0.03375	0.753	0.25	N/A	N/A
50	0	22.3	0.03375	0.753	0.25	N/A	N/A
51	0	22.3	0.03375	0.753	0.25	N/A	N/A
52	0	22.3	0.03375	0.753	0.25	4.34	1407
53	0	22.3	0.03375	0.753	0.25	4.31	1205
54	0	22.3	0.03375	0.753	0.25	4.29	1401
55	0	22.3	0.03375	0.753	0.25	4.35	1229
56	0	22.3	0.03375	0.753	0.25	4.23	1407
57	0	22.3	0.03375	0.753	0.25	4.33	1447
58	0	22.3	0.03375	0.753	0.25	4.21	1524
59	0	22.3	0.03375	0.753	0.25	4.32	1494
60	0	22.3	0.03375	0.753	0.25	4.24	1492
61	0	22.3	0.03375	0.753	0.25	4.24	1348
62	7	20	0.0328125	0.65625	0.3125	N/A	N/A
63	7	20	0.0328125	0.65625	0.3125	4.24	1685
64	7	20	0.0328125	0.65625	0.3125	4.31	1437
65	7	20	0.0328125	0.65625	0.3125	4.45	1531
66	7	20	0.0328125	0.65625	0.3125	4.4	1528
67	7	20	0.0328125	0.65625	0.3125	4.37	1555
68	4	20	0.0375	0.75	0.25	4.41	1575
69	4	20	0.0375	0.75	0.25	4.37	1570
70	4	20	0.0375	0.75	0.25	4.42	1571
71	7	20	0.0328125	0.65625	0.3125	4.32	1703
72	7	20	0.0328125	0.65625	0.3125	4.32	1712
73	5	20	0.0421875	0.84375	0.1875	4.39	1550
74	5	20	0.0421875	0.84375	0.1875	4.39	1550
75	5	20	0.0421875	0.84375	0.1875	4.39	1559
76	5	20	0.0421875	0.84375	0.1875	4.3	1523

77	5	20	0.0421875	0.84375	0.1875	4.4	1532
78	5	20	0.0421875	0.84375	0.1875	4.32	1513
79	6	20	0.046875	0.9375	0.125	4.6	1493
80	6	20	0.046875	0.9375	0.125	4.5	1439
81	6	20	0.046875	0.9375	0.125	4.58	1467
82	6	20	0.046875	0.9375	0.125	4.54	1467
83	6	20	0.046875	0.9375	0.125	4.64	1465
84	6	20	0.046875	0.9375	0.125	4.54	1445

Table XII-1B. Summary of relevant testing parameters and results.

Test #	Max PR	Min P_{plenum} (psi)	Max M_s	Max $\dot{m}_p$ (lb_m/s)	Centerline	Shadowgraph
29	151	4.91	0.89	1.01		X
30	222	3.67	0.87	1.34		X
31	214	3.75	0.89	1.21		X
32	255	3.43	0.77	0.91	X	
33	160	5.46	0.91	1.08	X	
34	86	8.48	0.6	1.5	X	
35	51	9.1	0.31	0.81	X	
36	75	9.09	0.7	1.4	X	
37	63	9.17	0.37	0.97	X	
38	88	8.63	0.45	1.34	X	
39	41	10	0.33	0.71	X	
40	47	8.79	0.62	0.92	X	
41	60	8.51	0.57	1.63	X	
42	90	8.36	0.77	0.68	X	
43	88	9.12	0.62	1.47	X	
44	73	9.44	0.72	1.5	X	
45	78	6.93	0.89	0.64	X	
46	160	7.7	1	1.25	X	
47	149	7.53	1.02	1.27	X	
48	148	7.56	1.04	1.23	X	
49	N/A	N/A	N/A	N/A		X
50	N/A	N/A	N/A	N/A		X
51	N/A	N/A	N/A	N/A		X
52	124	5.72	0.92	1.05		X
53	107	5.98	1.02	0.9		X
54	117	5.78	0.92	1.05		X
55	106	5.99	0.98	0.93		X
56	118	5.53	0.88	1.06		X
57	121	5.6	0.87	1.09		X

58	128	5.54	0.86	1.15		X
59	129	5.41	0.92	1.12		X
60	132	5.55	1.08	1.13		X
61	114	5.91	0.91	1.01		X
62	N/A	N/A	N/A	N/A	X	
63	127	9.75	1.05	1.26	X	
64	121	9.73	1.05	1.07	X	
65	121	9.76	1.19	1.14		X
66	125	9.8	1.25	1.14		X
67	133	9.17	1.07	1.16		X
68	146	7.02	0.95	1.33		X
69	155	7.08	0.97	1.34		X
70	151	6.8	0.93	1.34		X
71	147	7.82	0.97	1.27	X	
72	159	8.31	1.04	1.28	X	
73	141	7.73	0.99	1.65	X	
74	139	7.72	0.99	1.49	X	
75	139	7.71	0.99	1.67	X	
76	131	7.94	0.95	1.45		X
77	131	7.87	1	1.47		X
78	128	8.04	0.98	1.46		X
79	132	6.94	0.85	1.58	X	
80	126	7.35	0.82	1.53	X	
81	128	7.24	0.81	1.57	X	
82	127	7.27	0.82	1.56		X
83	128	7.42	0.84	1.56		X
84	131	7.42	0.88	1.54		X